The 1300AD dacite pumice eruption, Rinjani Volcano, East Sunda Arc: Petrology, petrogenesis and plumbing.

By Natasha Meegan

Discipline of Geology & Geophysics

School of Earth and Environmental Geosciences

Adelaide University

North Terrace, Adelaide, 5000

Phone: +61 8 8313 4455

natasha.meegan@student.adelaide.edu.au

A Manuscript as partial fulfilment of the requirements for the degree of Bachelor of Science with Honours,

November 2009

Supervisor: Professor John Foden

CONTENTS

ABSTRACT

Physical controls on fractional crystallisation in subduction settings around the globe are the focus of much discussion within academia. It is frequently observed that the typical magma to be erupted in arc settings is andesite from the differentiation of partially melted peridotite mantle wedge. It is less common in these settings to see more felsic end member magmas such as dacite or rhyolite being erupted in cataclysmic events. Discussion has arisen into what physical process or processes can drive a volcano, or set of volcanoes, within an arc to produce dacite or rhyolite magmas where fractional crystallisation is known to be the process of initial crystallisation. Research into these processes can be applied to Mount Rinjani (Lombok) within the Sunda Arc system, where the normally composite andesite volcano produced a cataclysmic eruption of dacite magma known as the Rinjani Pumice at 1300AD. Data is presented here in order to investigate processes within the sub-volcanic magma plumbing at Rinjani, primarily using volatiles from melt inclusions, coupled with petrology, pressure, temperature and water saturation estimates. It is theorised that ascent driven crystallisation from a parent basalt drove fractional crystallisation to andesite composition beneath Rinjani volcano. Water undersaturated conditions induced ascent of the andesite magma to a shallow reservoir at ~3 kbar at temperatures ~1015 °C, with water saturation ~3.7 weight percent. Melt inclusion data from these same crystals reveals the interstitial liquid in the andesite magma to be of evolved dacite composition (~66 wt % SiO_2) compared to the andesite (~50-54 wt % SiO_2).

Critical crystallinity is the physical process believed to have acted upon fractional crystallisation where the percentage of crystals forming exceeded the ability of the

magma chamber to convect within this reservoir and therefore physical separation of the evolved dacite liquid from the andesite magma occurred. The buoyant dacitic liquid ascends to another shallow reservoir directly beneath Rinjani volcano and reaches its saturation pressure at 1.8 kbar at a temperature of ~900 °C, with water saturation increased to ~5 wt %.

Sub-plinian cataclysmic eruption of the 1300AD Rinjani Pumice occurred due to pressure increase involved in saturation of the dacite, and syn-eruptive degassing aids in excavating the western flank of the Rinjani stratocone leaving a caldera.

Subsequent volcanism occurs where the magma ascent path migrates west producing more cataclysmic eruptions increasing the volume of the edifice. Today, resurgent volcanism can be seen in the central eastern part of Segara Anak lake at Gunung Baru within the Rinjani caldera to produce basalt and andesite lavas.

The application of physical mechanisms acting upon fractional crystallisation proposed here may be applied to other arc settings around the globe, where fractional crystallisation is found to be the primary driving force of felsic end member cataclysmic eruptions at what is typically an andesitic arc.

1. INTRODUCTION

Experimental data from various studies has recently challenged the conventional view of magma differentiation in calc-alkaline suites found in subduction zones (Bunsen 1851; Durocher 1857; Bowen 1928; McBirney 1980; McBirney et al. 1985; Brophy 1991; Blundy and Cashman 2001). The general identification for the process of segregation of volcanic rocks within a magmatic suite (i.e. basalt-andesite-dacite-rhyolite) is that of fractional crystallisation within the sub-volcanic magmatic system. Fractional crystallisation is the theory of a magma differentiating to become enriched in silica and incompatible elements. Lately, much focus has been turned to the physical mechanisms involved in the process of fractional crystallisation (e.g. Brophy 2009), with emphasis imposed on creating a more complex model of magma differentiation to accommodate for eruption products observed that cannot be explained by the basic theory alone.

These processes have been discussed by many. For example, discussion dates back to 1851, where Bunsen suggested magmatic suites may arise from the mixing of basalts and rhyolites producing an intermediate magma to create what seemed to be an evolving suite of silica enrichment. This idea was later challenged by many including Durocher (1857), who suggested that while in the liquid state, a homogenous magma could become vertically zoned due to chemical segregation of the liquid. Gravitational settling where crystals accumulate at the bottom of a magma chamber in accordance with their formation temperature, pressure and compositional requirements, was first discussed by Bowen (1928), where crystals typically forming in magmatic suites were first characterised into a formation sequence known as ‘Bowens Reaction Series’. McBirney (1980) and McBirney et al (1985) suggest that in collaboration, fractional crystallisation

may occur as a result of sidewall crystallisation and ‘liquid fractionation’ where liquid differentiates near a wall, and transported along the side wall up or down depending on its density changes in relation to its differentiation to create a vertically stratified magma column. This zoning has been observed to be inverted in some pyroclastic eruption products (Smith 1979; Hildreth 1981; McBirney et al. 1985). Recently, there has been development on the convolute theories discussed above in relation to the physical mechanism in fractionation. Authors such as Blundy and Cashmans’ (2001) studies of Mount St Helens magmas suggests that decompression-induced H_2O exsolution drives crystallisation within a magmatic suite, thus varying water content within a magma can determine the rate of crystallisation and differentiation. Marsh (2002) suggests a solidification front of magma plumes which differentiate the magma and induce a compositional gap between the middle of the chamber and the solidified materials. These compositional-gap and decompression-driven crystallisation theories are constructed upon by Brophy (2009), who suggests a direct link between the two physical processes by the crystal settling rate determining the eruption point at a given stage of magma differentiation.

The majority of these mechanisms explain the process of fractional crystallisation which commonly results in andesitic arc volcanic eruptions. Whereas dacite lavas can be common in andesitic arc volcanism as discussed in the theories cited above, the common belief is that to push andesitic magmas to a more felsic composition which may induce cataclysm, another source of silica has to be introduced such as crustal melting or AFC processes. However, what if an andesite volcano produces dacite pumice on rare occasion, and isotopic signatures show the felsic magmas have the same source of parental magma as the andesite or basalts produced from that volcano (Foden

1983)? Attention has to be then turned to the physical processes within the magma chamber during fractional crystallisation to drive an andesitic arc to produce dacitic magma.

In this paper, these issues are addressed in application to the 1300AD eruption of the Rinjani Pumice from Rinjani volcano, Lombok, Indonesia, and attempt to fit a fractional crystallisation model to this eruption that may be suited to other similar eruptions around the globe. Limited literature discusses the processes which led to the formation of the Rinjani Pumice, consequently the petrology and petrogenesis will be an aim of the paper. It is also an aim to constrain the sub-magmatic plumbing of the 1300AD eruption in relevance to the physical mechanism of fractional crystallisation that lead to the caldera forming eruption of dacite pumice from Rinjani volcano, in an otherwise basaltic to andesitic composite volcano. The source of the parental magmas is not discussed in this paper and is assumed to be from partial melting of the peridotite mantle wedge above the active Benioff zone within the Sunda Arc subduction system beneath Lombok island (Foden 1983).

Observations of pumice samples from the monogenetic caldera forming eruption at Rinjani 1300AD, compared here to literature based on the 1980 pumice eruption of Mount St Helens (Blundy and Cashman 2001) shows the two sites to have similar petrology and petrogenesis. Dacitic pumice was produced in a sector collapse of Mount St Helens in May 1980, from the northern side of the composite volcano after a bulge was observed there in April 1980 (Pallister et al. 1992). Extensive new methods of study outlined by Blundy and Cashman 2001 and Blundy and Cashman 2008, which focus on constraining pressure, temperature, water saturation and other magmatic variables in application to the 1980-1986 eruption of Mount St Helens. Some of the

methods applied to the 1980 Mount St Helens eruption will therefore be applied in analysis of the Rinjani Pumice to attempt to discover the processes which led to the eruption.

2. SETTING

2.1 Location

Mount Rinjani or 'Gunung Rinjani' to the locals, is located in the central northern area of Lombok island, Indonesia (Figure 1). Lombok makes up part of the Lesser Sunda Islands, being flanked to the west by Bali and to the right by Sumbawa. Rinjani is in the Sunda-Banda Arc above the northward dipping active subduction zone, where the Indo-Australian oceanic lithosphere under thrusts the Eurasian plate. The Sunda Arc extends from Sumatra in the west, all the way to Flores in the east where there is a transition into the Banda Arc which extends further east and then north to the islands in the Banda Sea (Figures 2 & 3) (Foden and Varne 1980). The transition from the Sunda to Banda Arc is due to an extraordinary convergence of three tectonic plates, the Indo-Australian, Eurasian and Pacific plates, making up part of the ring of fire. Rinjani volcano is approximately 300km north of the Java trench (e.g. Hamilton 1974; Hutchison 1976; Foden 1983). Subduction of oceanic crust of the Indo-Australian tectonic plate beneath oceanic crust of the Eurasian plate has resulted in Lombok being bordered to the north and south by oceanic crust (Foden and Varne 1980). The Benioff Zone has been approximated to be 170km beneath Rinjani volcano (Elburg et al. 2007). Crustal thickness decreases from the west to the east within the Sunda Arc in correlation with age and continental crust component (Foden and Varne 1980). In the west, Sumatra and Java consist of continental crust and have rocks of Mesozoic and Palaeozoic age (Katili 1973; Hamilton 1974; Foden and Varne 1980). As the Sunda Arc extends eastward, continental crust decreases within the islands. At Lombok, the crust is relatively thin and volcanic in nature and has only been dated as far back as the Miocene (Foden and Varne 1980).

2.2 Geology

Rinjani Volcano is a composite strato-volcano which most commonly erupts andesitic to basaltic magmas (Foden 1983). Cataclysmic events have blasted a large caldera into the volcanic dome, which now holds the lake 'Segara Anak', which sits approximately 2000 m ASL (Figure 1) and is approximately 7.5 km long and 3.5 km wide. The peak of Rinjani is 3723 m ASL and was once a vent in strato-cone stage. Resurgent volcanism within Segara Anak is building a cinder cone known to the locals as 'Gunung Baru' or 'New Mountain'.

Detailed information regarding eruption sequences from Rinjani and their deposits are scarce. There have been studies in relation to the andesite and basalt magmas and their deposits but little information regarding the pumice in question can be found.

2.2.1 Eruptive history

Eruptions from Rinjani dating back to 12000-6000 years B.P., accumulated to build a stratocone, where the vent is seen to be the peak of Rinjani today on the eastern side of the caldera (Takada et al. 2004). Dating back 6000-8000 years B.P., a cataclysmic eruption collapsed the western flank of the stratocone (Takada et al. 2004). The main magma path continued to ascend east of the previous vent in a second stage of stratocone building. A second cataclysmic event produced an even larger caldera than the first, with a plinian eruption depositing the Rinjani Pumice, and consequent collapse of the caldera induced pyroclastic flows which deposited ash (Takada et al. 2004). The vent of Rinjani is now visible as a resurgent cone in the eastern zone of Segara Anak (Gunung Baru) within the caldera walls. Eruptions from Gunung Baru consist of basaltic to andesitic lava.

2.2.2 Volcanic Deposits

The north-west area and Southern Hilly Terrain of Lombok, are comprised of Tertiary volcanic and sedimentary deposits, while the northern and central areas are Quaternary volcanics (Matrais et al. 1972). Within the Quaternary volcanic deposits, there is a basaltic lava exposed in the north of the island (from stratocone building stage), a volcanic breccia consisting of basalt and andesite exposed on the southern outer slopes of Rinjani, and overlaying these is a pumice (Rinjani Pumice) exposed in most of the area surrounding Rinjani (Matrais et al. 1972). This pumice is thought to be partly responsible for the cataclysmic caldera forming event(s). Erosion has removed or re-mobilised much of the primary pumice, forming secondary deposits that have been found in the south-eastern slopes of Rinjani (Matrais et al. 1972). The Rinjani Pumice has been roughly dated by the Volcanology and Geologic Hazard Mitigation of Indonesia to have formed 1210-1260AD. It is the primary pumice deposits that are the focus of this paper.

3 METHODOLOGY

In order to constrain the conditions with the magma chamber prior to the eruption 1300AD at Rinjani, analysis was carried out of crystals, glass groundmass and melt inclusions within the pumice. Microprobe analysis of mineral species within the melt, coupled with melt inclusion and glass analysis provided constraints on temperature and pressure at time of crystallisation. As water and other volatiles are lost during eruption, especially in the case of explosive eruptions, analysis of melt inclusions trapped within minerals gives an indication of volatile content at time of crystallisation of the host mineral. This is similar to the glass groundmass as it was solidified at time of eruption, although it is more available for volatile gassing. Melt inclusions and glasses were therefore the focus of analysis.

Previous studies of the Lombok area by Professor John Foden of The University of Adelaide, created a sample base of pumice from the island, with a range of thin sections already prepared from many of the samples. Pumice samples were collected opportunistically from the north coast of Lombok to the north and north-western slopes of Mount Rinjani. Although data has been published from studies of lava samples from Mount Rinjani, no literature in relation to the Rinjani Pumice was discovered. Therefore, methodology was based wholly on pumice samples collected from Mount Rinjani.

XRF (whole rock) and some minimal Nd, Sm and Sr isotope data was previously been obtained from these samples by Foden (2001-2002), in addition with whole rock analysis of lava samples erupted prior to the 1300AD pumice. This whole rock analysis was used in conjunction with analysis collected for this paper to create a new data set of

petrography and major and trace elements. For an extended explanation of sample preparation and sample analysis, see Appendix A.

3.1 Petrography

Some thin sections from previous studies by Foden (2001-2002) were already prepared. These thin sections came from samples Lo18, Lo39, Lo52 and Lo54. Photos of the thin sections were taken with a transmitting light microscope using various magnifications. Within selected thin sections, petrographic descriptions were given based on the following descriptions.

- Minerals present
    - Proportions
    - Optical properties
- Crystallinity
- Mega/mesoscopic rock fabrics
- Meso-microscopic textural features including the glassy groundmass
- Quality of Grain shape
- Grain Shape
- Grain Size

Any other observations such as oxidised rims of minerals, zoning of plagioclase, and intergrowth were noted. Photos were taken of grain mounts(prepared using methods outlined below) at Adelaide Microscopy using the Leica MZ16FA Stereomicroscope.

These images were also used to create a petrographic understanding of the pumice. The compilation of observations from all of these images was summed into descriptions for a select few images thought to be representative of the all the pumice samples. A general report was then made to incorporate a general petrographic understanding for the Rinjani Pumice as a whole.

3.2 Preparing the samples

Target minerals for analysis with the Laser ICP-MS and Electron Microprobe at Adelaide Microscopy were found using the light transmitting microscope. Target areas were mapped by circling target areas with pen on the surface of the samples for visual aid during analysis. The thin sections were then sent to Adelaide Microscopy to be carbon coated ready for analysis.

Grain mounts were prepared by crushing rocks from samples Lo23, Lo39 and Lo54 in a tungsten carbide rock crusher at Adelaide University. Grains were then sieved into separated sizes where grains greater than 0.75 mm and less than 1.5 mm were used for further preparation. The grains were then washed and separated into magnetic and non-magnetic minerals. Mounts were then prepared by having two grain separates from each sample, one for magnetic and one for non magnetic minerals (i.e. Lo23MGM (magnetite grain mount) and Lo23PGM (plagioclase grain mount). Epoxy resin was poured into each mount, once set, the mounts were polished to expose the grains for analysis. The mounts were mapped by circling target areas with pen and sent to Adelaide Microscopy for carbon coating.

3.3 Major element analysis

Thin sections Lo18, Lo39, Lo52 and Lo54 and grain mounts Lo23MGM&PGM, Lo39MGM &PGM and Lo54MGM&PGM were analysed using the Cameca SX51 Electron Microprobe at Adelaide Microscopy. The microprobe detects elements by measuring wavelengths emitted from atoms in the target when they have been excited and are releasing the extra energy. The Microprobe was programmed to analyse for major elements Na, Mg, Al, Si, P, S, Cl, K, Ca, Ti, Cr, Mn, Fe, Ni and Zn.

3.4 Geothermometers, Geobarometers and Hygrometers

Barometry and thermometry for the 1300AD Rinjani dacite eruption was conducted based on the minerals present within the pumice. Geobarometry, geothermometry and hygrometry methods within Microsoft excel programs, created by various authors (as outlined below), were used to input major element data to calculate pressure, temperature and water saturation estimates at eruption. These methods used oxide weight percent values from major element analysis. For methods using two mineral species for calculations such as OPX-CPX-P-T, it was ensured that only major element analysis of rims from the two minerals would be used or alternatively major element analysis of cores from the two minerals as they are assumed to have formed in equilibrium. For methods that used a phenocryst and the liquid it was in equilibrium with such as Feldspar-Liquid, major element analysis of the cores was used in calculation with melt inclusion major element analysis for that mineral species (assuming there is no ion exchange between the ions in the melt inclusions and the host minerals). Alternatively if rims of phenocrysts were to be calculated with equilibrium liquid, this was performed in calculation with major element analysis of associated glass. For full details of all geothermometry, geobarometry and hygrometry methods,

see Anderson et al. (2008); Blundy and Cashman (2001); Lange et al. (2009); Lowenstern (2000); Newman and Lowenstern (2002) and Putrika (2008). Methods used were:

3.4.1 CPX-Liquid-P-T

The CPX-Liquid method uses partitioning of Fe and Mg exchange between clinopyroxene and its associated liquid (Putrika 2008) to focus on obtaining a temperature of formation when the clinopyroxene was in equilibrium with the liquid. Methods were carried out in accordance with Putrika (2008). Major element data from clinopyroxene and associated equilibrium liquid was used. Data was entered into a Microsoft Excel macro where pressure and temperature estimates were calculated.

3.4.2 OPX-CPX-P-T

Pressure and temperature values are calculated using this method based on the distribution of Ca, Mg and Fe between orthopyroxene and associated clinopyroxene crystals (Putrika 2008). Methods were carried out in accordance with Putrika (2008). Major element data from orthopyroxene and associated clinopyroxene was used. Data was entered into a Microsoft Excel macro where pressure and temperature estimates were calculated.

3.4.3 Silica activity

Methods were carried out in accordance with Putrika (2008). Major element data from glasses and melt inclusions were entered into a Microsoft Excel macro where pressure and temperature estimates were calculated.

3.4.4 Feldspar-Liquid

Methods were carried out in accordance with Putrika (2008). Major element data from plagioclase and associated liquid was used. Data was entered into a Microsoft Excel macro where pressure, temperature and water saturation estimates were calculated.

3.4.5 Olivine-Liquid

Methods involving thermometry calculations of olivine and its associated liquid are based on the partitioning of Mg between the phenocrysts and the liquid it is in equilibrium with (Putrika 2008). Methods were carried out in accordance with Putrika (2008). Major element data from olivine and associated liquid was used. Melt inclusion data was coupled with olivine cores for temperature calculations however, no glass analysis was found to be in association with olivine rims. Therefore, major element whole rock data was used in place of glass analysis as the pumice was crystal poor, whole rock data was thought to represent a similar composition as the glass matrix. Data was entered into a Microsoft Excel macro where temperature estimates were calculated.

3.4.6 Hornblende-Plagioclase

Hornblende plagioclase methods use the ratio of albite and anorthite values from plagioclase rims in comparison with the composition from associated hornblende rims, which shows a relationship between the partitioning of aluminium between the two crystals when they are in equilibrium. Methods were carried out in accordance with Anderson et al. (2008). Major element data from hornblende rims and associated plagioclase rims was used. Data was entered into a Microsoft Excel macro where temperature estimates were calculated.

3.4.7 Water Saturation

Methods were carried out in accordance with Lange et al. (2009). Ratios of albite and anorthite were calculated from plagioclase major element data and used in association with average major element values from the glass matrix, and also re-calculated with average major element values from melt inclusions. These parameters were also calculated in association with pressure and temperature values, calculated using the methods outlined above to obtain water saturation percentages at stated conditions.

3.4.8 Saturation Pressure

Methods were carried out in accordance with Newman and Lowenstern (2002). Temperature and water saturation percentage calculated using methods outlined above were input into the VolatileCalc program, along with a standard CO_2 concentration of 200ppm (as this was not calculated it was kept constant).

3.4.9 Normalisation

Major element analysis of glass and melt inclusions was input to the NormCalc program where Lowenstern (2000) compiled methods from Kelsey (1965) and Le'Maitre (1976). Quartz normative values were calculated for a set of mineral species typical of volcanic rocks. Values for Quartz, Orthoclase, Albite and Anorthite normative were taken from this normalisation where Quartz, Orthoclase and Albite were together normalised to 100%. These normalised values could then be used to create a haplogranitic projection from methods outlined in Blundy and Cashman (2001). The haplogranite projection could then be used for pressure estimates of eruption and to constrain the driving force of crystallisation within the magma as discussed in Blundy and Cashman (2008).

3.5 Modelling crystallisation sequence

Once pressure, temperature and water saturation data was calculated using the methods above, this was then compared to an experimental simulation using the program 'Pele' (Boudreau 1999). Pele can calculate a series of composition and crystal phases during a fractionation process from entering the data of the starting and finishing pressure and temperature values, and a starting composition of a parental magma. This was carried out from the input of the composition of lava sample Lo46 from whole rock data (Foden 2001-2002), which was then modified as the simulations were ran to try and reach then end product composition calculated from the pumice samples. Four simulations were executed isobarically for four different pressures. These were 2000 bar, 1500 bar, 1000 bar and 500 bar. Temperature input started at 1500 ºC and ended at 900 ºC, as temperatures below 900 ºC could only yield a gas phase in accordance with the pressure and compositional parameters. For comparison, two more simulations were run with the same starting composition from lava sample Lo46. A simulation was executed at 2000 bars and when finished, the resulting composition was normalised, a new liquidus temperature calculated and executed again at 1500 bars. Once again a simulation was executed at 2000 bars with starting composition modified from sample Lo46, and the resulting composition was executed again at 1000 bars. For this execution the liquidus temperature was found to be less than 900 ºC, less than the parameters limited other executions to terminate at, therefore for this experiment, the terminating temperature of crystallisation was changed to be 800 ºC.

3.6 Trace element analysis

Thin sections Lo18, Lo39, Lo52 and Lo54 and grain mounts Lo23MGM&PGM, Lo39MGM &PGM and Lo54MGM&PGM were analysed using Laser Ablation ICP-

MS at Adelaide Microscopy. Laser ablation uses a plasma gas (Argon) to dissociate molecules and ionise atoms. The mass numbers of these ions are then detected and sorted into abundance. Trace and some major elements included in the analysis were Mg, Si, K, Ca, Sc, Ti, V, Cr, Mn, Fe, Co, Ni, Cu, Ga, Rb, Sr, Y, Zr, Nb, Ba, La, Ce, Pr, Nd, Sm, Eu, Gd, Tb, Dy, Ho, Er, Tm, Yb, Lu, Hf, Ta, Pb, Th and U, the specific isotope detected for each element can be seen in Appendix B. Silica oxide weight percent data from major element samples was used as a standard for trace element analysis in corresponding samples.

Melt inclusion and glass analysis results of trace elements were arranged and chondrite normalised according to Sun and McDonough (1989). Spidergrams were then created from this data.

4. RESULTS

4.1 Petrography

Correlation of all petrographic observations of Rinjani Pumice samples is summarised in Table 1. Previous studies of Andesite thin sections from Rinjani lavas show the crystal phases to include plagioclase, clinopyroxene, orthopyroxene, magnetite, hornblende and some olivine.

In pumice thin sections and grain mounts, plagioclase was the most abundant mineral followed by hornblende, magnetite, orthopyroxene and clinopyroxene respectively. The glassy vesicle dense groundmass was observed to account for approximately 70% of the pumice. The overall broad mineralogy is dominantly isolated clusters of crystal aggregates matching the crystals observed within the pumice thin sections, with an extremely vesicle rich homogeneous matrix. In comparison, thin sections of andesite contain a much higher percentage of crystals, approximately 50-60%. The interstitial matrix of andesite samples is comprised dominantly of glass with minor vesicles (~10%). No quartz from petrographic observations or electron microprobe analysis was discovered within the pumice. Detailed descriptions of minerals and associated melt observed within pumice thin sections and grain mounts are as follows:

4.1.1 Plagioclase

Plagioclase was observed to have twinning in most phenocrysts. Zoning was also observed in around 70% of phenocrysts (Figures 4, 5, 6, 7, and 8). Zoning was commonly observed to have few oscillations and in some cases only one distinct broad band of zoning (bottom left phenocryst in Figure 5 and right phenocryst in Figure 7). Approximately 35% plagioclase phenocrysts were seen to have dense oscillatory zoning

(Figures 4 and 6). Unzoned or partly zoned small fragmented plagioclase phenocrysts were seen to as inclusions in hornblende (Figure 9). Melt inclusions were dominant within plagioclase cores and are rare in rims (Figures 4, 5 & 6). Plagioclase was dominantly found in close proximity with hornblende phenocrysts.

Transects of major element analysis across zoned plagioclase crystals are represented in Figures 15 to 17. The cores of all transects can be seen to be calcium rich and sodium poor while the rims are calcium depleted and sodium enriched, showing plagioclase to be in equilibrium with the melt in fractional crystallisation conditions.

4.1.2 Hornblende

Hornblende phenocrysts were observed to rarely exhibit oxidised rims but in some cases were visible in cross polarised light by the shift in birefringence (Figure 10). Phenocrysts were dominantly euhedral and if fragmented, were still aggregated. Hornblende can be seen replacing a pyroxene crystal (possibly clinopyroxene) in Figure 4. Needle like apatite inclusions were seen to be common within hornblende crystals (Figures 7, 10, & 11), and less commonly, plagioclase inclusions (~1000 µm) were also present within the mineral (Figure 9).

4.1.3 Magnetite

Magnetite was observed to commonly be in contact or close proximity with all mineral species, and form distinct equant shaped crystals (Figures 4, 6, 7, 8, 9, 11, 12 & 13).

4.1.4 Pyroxenes

Orthopyroxene was observed to be slightly more abundant than clinopyroxene and often both mineral species were observed to be in proximity of each other but not in direct contact. Both pyroxenes had a closer proximal association with magnetite than other mineral species, often growing around it (Figure 13).

4.1.5 Glass matrix

Groundmass of samples from the Rinjani Pumice were only visible in thin sections. The glassy matrix was void of any minerals but dense in vesicles (Figure 14). The abundance of vesicles created problems for glass analysis using the Electron Microprobe and Laser ICP-MS.

4.1.6 Melt inclusions

Melt inclusions were visible in cores of plagioclase and throughout all other mineral species. Inclusions were small, typically less than 100microns wide. Some inclusions formed as elongate needles which were too thin for analysis due to error margins (Figure 10).

4.2 Major elements

XRF (whole rock) and Electron Microprobe analysis of minerals, melt inclusions and glass from the Rinjani Pumice can be seen in Table 2. Microprobe analysis confirmed the minerals present from petrographic observations, with addition of minor biotite and olivine. Major element analysis reveals values from whole rock pumice ~62 wt% SiO_2 compared with individual crystal analysis where plagioclase yields values ~53 wt% SiO_2, hornblende ~43 wt% SiO_2, orthopyroxene ~53 wt% SiO_2, clinopyroxene ~51 wt% SiO_2, magnetite ~.15 wt% SiO_2. Melt inclusions and glass have similar values of silica enrichment of 66.5 wt% SiO_2 and 65 wt% SiO_2 respectively. These values are evolved from whole rock data on andesite samples which has silica enrichment of ~50-54 wt% SiO_2.

4.2.1 Major element variation

Bivariate harker diagrams in Figure 18, show relationships between selected major elements with increasing SiO_2 wt % (increasing fractionation) for whole rock analysis

of Rinjani lavas and pumice, coupled with electron microprobe analysis of melt inclusions and glasses. TiO_2 initially increases in the lavas before decreasing proportionally with increasing silica towards pumice, melt inclusion and glass components. Al_2O_3, FeO, MgO and CaO show a roughly proportional decrease with increasing silica. Al_2O_3 can be seen to be depleted slightly when silica enrichment reaches the pumice (dacite) composition. Glass and melt inclusion analysis from the four plotted cations is seen to decrease more than the proportional trend with silica enrichment, possibly due to differences in calibration of XRF and microprobe analysis. Similarly, Na_2O wt % values for glass and melt inclusions shows an average of a 75% drop with silica enrichment compared to pumice values. Microprobe analysis of sodium can sometimes give spurious results due to water within the glass or melt inclusions. To correct for this, silica is plotted against Na_2O wt% where a range of pumice whole rock values of sodium have been substituted and plotted against silica enrichment (Figure 19). These substituted Na_2O values were then used for all glass and melt inclusion calculations. K_2O wt% values can be seen to increase with silica enrichment in a roughly proportional trend, although once silica enrichment reaches 60 wt% SiO_2 in the pumice samples, there is an increase in potassium values with constant silica. The positive trend then continues between the two oxides.

4.3 Depth of origin, Pressure, Temperature and water saturation of eruption

Geobarometry, geothermometry and hygrometry results are summarised in Table 3. The highest temperatures obtained were from clinopyroxene and associated liquid thermometry after Putrika (2008) where cores and rims of clinopyroxene returned similar values of 1016.15ºC and 1011.15ºC respectively. Thermometers using silica alone returned the second highest average value for temperature where glass was found

to be 993.22 ℃ and melt inclusions to be 986.08 ºC, showing the former glass temperature at the time of eruption were hotter than latter more primitive melt inclusion temperatures. Olivine and coexisting liquid returned the third highest temperature of 989.70 ºC, followed by plagioclase and liquid from methods discussed by Putrika (2005) of 986.08 ºC. These temperatures were followed by coexisting clinopyroxene and orthopyroxene analysis of cores with a value of 915.92 ºC, hornblende-plagioclase analysis values of 914.74 ºC, clinopyroxene and orthopyroxene analysis of coexisting rims with a value of 901.7 ºC and finally an inconsistently low temperature of 675.24 ºC was found with plagioclase-liquid methods discussed by Putrika in 2008. Pressure results were found not to follow the same suit where the highest pressures were found using clinopyroxene and orthopyroxene barometry to be 3.03 kbar. This was followed by plagioclase-liquid methods (Putrika 2005) to be 3.11 kbar, clinopyroxene and orthopyroxene barometry to be 2.99 kbar, glass barometry (2.54 kbar) and finally melt inclusion barometry which returned a pressure of formation value in average of 1.80Kbars. This value is analogous with the pressure of saturation found using VolatileCalc of 1.81 kbar. Water saturation percentages were found to be highest in plagioclase-liquid hygrometry from Putrika (2008) of average 10 % H_2O. Water content was found to be 5.6 wt% for clinopyroxene-orthopyroxene methods and 5.3 wt% using hornblende-plagioclase methods. The plagioclase-liquid thermometer from Putrika (2005) gave a water content of 4.2 wt%, much lower than the thermometer method from Putrika in 2008. Silica alone and olivine-liquid methods all returned water contents of 4 wt% where lower values of 3.7 wt% were obtained from clinopyroxene-liquid methods.

Feldspar and associated liquid methods from Putrika (2008) gave results not only of pressure and temperature, but also gave estimates of weight percent water saturation.

These values are not thought to correspond to water values obtained using the methods from Lange et al. (2009) but are represented in Figure 20 to show association of silica enrichment within the melt compared to water saturation for that analysis. It can be seen that silica values remain constant with changing weight percent values of water (syn-eruptive degassing line), however depending on how the data is interpreted, there is also suggestion that silica may decrease slightly with decreasing water content (decompression H_2O saturated line) or possibly increase when water saturation remains constant (isobaric H_2O saturated line).

Figure 21 was plotted in accordance with Blundy and Cashman (2001). The ternary diagram shows the melt inclusions from Rinjani Pumice to have highest affinity for the albite (sodium) end member of plagioclase. Pressures consistent with the albite component from this diagram were calculated using methods from Blundy and Cashman (2008) in Figure 22. The relationship between the albite component and pressure is seen to be positively proportional where if albite component within a haplogranitic system is increased, the pressure of the system is also increased. Albite pressure values obtained were between 0 and 2 kbar.

4.4 Modelling crystallisation sequence

Results for fractional crystallisation simulations at 2000 bar, 1500 bar, 1000 bar and 500 bar using Pele can be seen in Figure 23 represented by a silica versus titanium bivariate diagram. The simulations are compared to whole rock data of lava and pumice from whole rock analysis, melt inclusions and glasses from Electron Microprobe analysis. It can be seen that the simulations that were conducted with high pressure (i.e. 2000bar) fits closer to the calculated whole rock data than simulations executed at low pressure (i.e. 500bar). The next fractional crystallisation simulation (Figure 24) shows trends

concordant with calculated data, where the first simulation at 2000bar and the resulting composition at 1500bar shows a consistent fractional crystallisation trend. When the resulting composition from simulations ran at 2000 is executed at 1000bar (Figure 25), silica becomes enriched independent of titanium depletion between values of 55 and 64 wt % SiO_2. These values correspond to the transition of andesite to dacite classification of volcanic rocks.

Simulations using Pele at all pressures obtained the similar mineral phases observed in petrographic and major element analysis with olivine, clinopyroxene, plagioclase and magnetite. Error reports from the program indicated that there were errors in trying to find a stable phase for clinopyroxene and therefore this was not observed to be crystallised. The program also did not crystallise any amphibole phases which is inconsistent with the hornblende abundance seen in petrographic observations and calculated using electron microprobe analysis. Phases simulated that were not observed using calculated methods were gas and ilmenite. All simulations achieved the same mineral phase results with the exception of executions at 2000bar where gas was not present. Output from Pele executions are displayed in Appendix C.

4.5 Trace elements

Figure 26, 27, 29 and 29 show trace element patterns normalised to primitive mantle (Sun and McDonough 1989), where the most incompatible element is the left far most element and the most compatible the right far most element.

Pumice whole rock trace element patterns from samples Lo18, Lo23, Lo39, Lo52 and Lo54 (Figure 26) show the same trend in element mobility. Rb, Nb, Pb, and Y are all

depleted With the exception of Rb, this shows depletion in High Field Strength Elements (HFSE). Ba, U, La, Ca, Sr and Zr are all enriched, especially Uranium.

Trace element representation in Figure 27 shows trends in element mobility of sample Lo23. Ba, La, Sr and Eu are enriched while Rb, Nb, Pr, Nd, Zr, Hf and Ti are depleted. Negative anomalies are seen in Nb, Zr, Hf and Ti.

Sample Lo39 (Figure 28) shows depletion in Rb, Nb, Pb and Ti and enrichment in Ba, La and Eu. No negative anomalies are plotted in this diagram.

Figure 29 shows sample Lo54 to be depleted in HFSE with low values of Rb, Th, Nb, Pb, Zr and Ti and to be slightly enriched Low Ion Lithophile Elements (LILE) such as Ba, U, La, Sr and Eu. Negative anomalies are observed for Rb, Nb, Pb, Zr, Hf, Ti and Y.

4.6 Caldera volume

The crude caldera volume estimate from basic cylinder volume mathematics was calculated to be 39.56 Km^3 (Table 4). DRE volumes of the Rinjani Pumice calculated by Takada et al. (2004) to be 0.3 Km^3, significantly less than the estimated volume of the caldera calculated here.

5. DISCUSSION

5.1 Petrography

In plagioclase, zoning that was shown to have few oscillations may suggest limited changes in melt composition that was in contact with the phenocrysts as they formed. This may correspond to late stage crystallisation. Some plagioclase phenocrysts are seen to have well-developed oscillatory zoning (Figure 6) suggesting the crystal has coexisted with a varying composition of melt, which is consistent with fractional crystallisation. Abundant oscillatory zoning could also be a result of formation syn-water saturation as the magma was forced to degas, which drives formation of plagioclase phenocrysts.

Few hornblende phenocrysts are seen to have oxidised rims. At water saturation conditions, water is exsolved from the melt rapidly in a cataclysmic event. As a result of this, hydrous minerals such as hornblende that are in contact with the melt usually acquire oxidised rims. The higher the percentage of water within the magma, the more cataclysmic the eruption, and it would be expected that the rims of hydrous minerals would become more oxidised. As few hornblende mineral rims are oxidised from the Rinjani Pumice, it could be suggested that the water content of the magma at saturation point was low. The euhedral habit of hornblende suggests that most hornblende phenocrysts are stable in the magma at time of eruption, which can challenge the preceding suggestion that water saturation percent was low at time of eruption, as the function of stability of the mineral phase at time of eruption exempt it from forming oxidised rims.

This observation is supported by discussion from Elburg (2010) that shows hornblende to be stable at pressures <3.7 kbar, temperatures <1050 °C with a range of water saturation starting from highest 5.5% as plotted in Figure 30. Apatite inclusions along with plagioclase inclusions were often observed within hornblende crystals. This suggests apatite, forming small needle like crystals was a stable crystallising phase immediately prior to and during hornblende crystallisation. As there are no plagioclase inclusions observed within magnetite, orthopyroxene and clinopyroxene (not to suggest it is not there), may show that it was less stable as a crystallising phase in the melt during magnetite and pyroxene crystallisation than it was during hornblende crystallisation.

Magnetite was observed commonly in direct contact with pyroxenes. Petrography of grain mounts showed orthopyroxene and clinopyroxene to armour magnetite crystals. This follows Bowen's reaction series and it may be suggested that the magnetite crystals created a nucleation point for crystallisation of pyroxenes when the composition of the magma changed to favour pyroxene formation.

The presence of both orthopyroxene and clinopyroxene suggests that the Rinjani Pumice is sourced from a primitive dacite. Following Bowen's reaction series, clinopyroxene may be replaced by orthopyroxene as calcium becomes less available in the melt for crystallising mineral species to use. The initial crystallisation of calcium rich plagioclase (anorthite) is consistent with the calcium rich pyroxene species where clinopyroxene may have been favoured due calcium in its mineral formula. As the magma evolved to become more sodium rich and increasingly calcium poor, conditions favouring precipitation of anorthite phenocrysts may have ceased and orthopyroxene may have been able to form (calcium poor pyroxene). Petrographic observations show

orthopyroxene to be slightly more common than clinopyroxene suggesting that the magma was in the stage where it had more affinity to crystallise orthopyroxene, but fractionation had not proceeded as far as replacing all clinopyroxene.

Melt inclusions were often small, <200µm, and it is an assumption that host minerals may have formed quickly and had limited time to trap surrounding melt.

The absence of minerals within the glass matrix gives rise to speculation about the formation of magma that produced the Rinjani Pumice. Although dense in vesicles, the glass is homogenous suggesting a crystal poor, homogenous dacite melt was erupted. Andesites erupted from Rinjani are generally abundant in mineral grains and therefore, gives rise to thought of the origin of the few crystals that do reside in the dacitic pumice. These crystals may be remnants from andesitic magma, that the dacitic melt migrated away from, where complimentary oscillatory zones may have been added to plagioclase phenocrysts during degassing and eruption, and in addition, new unzoned plagioclase phenocrysts may have formed. The presence of isolated clusters of phenocrysts within a homogeneous glass groundmass is referred to by Blundy and Cashman (2008) to be consistent with shallow plugs in the sub-volcanic plumbing system.

Zoning of plagioclase represented in Figures 15 to 17 is consistent with fractional crystallisation in calc-alkaline suites. Initial growth in the plagioclase cores is calcium rich and sodium poor consistent with primitive melts. The outer zones of plagioclase are enriched in sodium where the albite end member of plagioclase becomes dominant over anorthite as the phenocryst is in equilibrium with a more fractionated melt.

5.2 Major element analysis

5.2.1 Major element variation

The initial increase in titanium with silica enrichment (Figure 31) in the harker diagrams is probably due to titanium enrichment prior to formation of magnetite. As magnetite started to crystallise, titanium becomes decreasingly abundant in the magma as it fractionates. Decreasing trends in FeO and MgO with also decreasing Al_2O_3 and CaO with silica enrichment (Figure 18) are consistent with the general notion that this trend is typical of calc-alkaline suites. The proportional increase in sodium with silica enrichment is typical of fractional crystallisation as is the increase in K_2O. However, fractional crystallisation would suggest that there would be a distinct linear relationship between potassium and silica enrichment, this is not the case. Once silica values approach 60 wt% SiO_2 in the pumice samples, silica enrichment ceases and potassium enrichment becomes larger, then the trend returns back to the norm. This suggests that potassium enrichment exceeded fractionation of the andesite parent magma. Figure 32 shows two distinct separate trends for potassium enrichment during fractionation. As silica fractional crystallisation is assumed to be consistent down temperature, this shift in potassium enrichment can be thought to happen isothermally. The relationship between potassium and silica here may give indications of sub volcanic plumbing prior to the 1300AD pumice eruption at Rinjani. The initial linear relationship between silica and potassium in the basalt and andesite composition lavas is typical of fractional crystallisation where the lowest values of silica would have no crystals and the highest values within the lavas (around 58 SiO_2 wt%) would be dense in crystallisation (magma A, Figure 32). The enrichment of potassium corresponding to a pause in fractionation is initiated in the dacite compositional field (pumice), suggesting that the liquid in

equilibrium with the abundantly crystallised andesite was of dacite composition and separated itself from the melt (magma B, Figure 32). This process would not involve fractional crystallisation and hence the lack of silica enrichment visualised in Figure 32 during potassium enrichment. The reason for increasing potassium with no corresponding silica enrichment being an independent trend of all other positive linear bivariate trends, may be due to potassium becoming mobile within the melt and not partitioning to any of the crystals already formed within the andesite.

5.3 Trace element analysis

The depletion of HFSE (Nb, Pb and Y) in trace element trends from whole rock data (Figure 26), may suggest a trend towards the primitive mantle and therefore early stages of fractional crystallisation. Due to this assumption, it is thought high concentrations of some LILE's such as Sr and Zr are due to the overall lack of partitioning to plagioclase and zircon crystallisation respectively, rather than crustal contamination. This would happen as a plagioclase is not formed abundantly in magma, so element which typically partition to its crystallisation become enriched. Similarly, enrichment of LILE elements can suggest a mobile fluid is present within the magma.

Enrichment in Sr and Eu (LILE's) in sample Lo23 (Figure 27) is typical of a lack of partitioning to plagioclase crystallisation. Positive Eu anomalies can be attributed from crystallisation of pyroxenes and hornblende which is consistent with petrographic observations. Concentration of LILE's can also be from a mobile fluid phase within the melt or crustal contamination. The latter is consistent with a negative Nb anomaly which can suggest that there has been some contribution of a crustal component to the melt. The negative trend in Ti is consistent with partitioning to magnetite formation during fractional crystallisation. Depletion of Zr can be explained by partitioning to

zircon crystallisation although the presence of this mineral was not analysed for and thus cannot be confirmed.

Sample Lo39 trace element trends (Figure 28), like whole rock trends, do not suggest crustal contamination as strongly as sample Lo23. Depletion is more dominant in HSFE's suggesting like the whole rock trend, that the magma is trending towards its primitive mantle end member. Although Nb values are low, they are not negative and cannot be interpreted to be a function of crystal contamination. Depletion of Ti is constant with magnetite formation during fractional crystallisation. Eu enrichment can be interpreted as the lack of partitioning to plagioclase, but as petrographic observations show plagioclase to be a common mineral, it is likely the enrichment of this LILE element is due to a fluid phase becoming mobile within the melt or the fact that pyroxenes and hornblende are stable within the magma.

Depletion of HFSE in sample Lo54 (Figure 29) is once again consistent with a magma that has not extensively fractionated from its source. Concentration of LILE such as Sr and Eu suggests plagioclase is once again not a dominant crystallisation phase although observed in petrographic observations, and that pyroxenes and hornblende are the stable mineral phases. This may suggest that most plagioclase crystallisation can be attributed to early fractional crystallisation with complementary zones acquired through changing melt conditions, and that it may have been a stable mineral phase only in the primitive melt, and possibly immediately prior to eruption when driven to crystallised by volatile degassing. So far sample Lo54 has been consistent in suggesting fractional crystallisation to be the dominant physical mechanism of silica enrichment which agrees with interpretations from sample Lo39 and whole rock patterns. But, like sample Lo23, Lo54 shows distinct negative anomalies for Nb suggesting there is some degree of

crustal contamination to the magma. Negative Zr and Hf anomalies can also be due to partitioning to materials introduced by crustal contamination as if Zr was being partitioned to zircons, then you would not expect to also see a negative anomaly in Hf.

5.3.1 Trace element variation-isotopes

Previous strontium isotope analysis by Foden (2001-2002) is displayed in Figure 33. It can be seen that with silica enrichment from whole rock data of lava (blue) and pumice (red), the ratio of stable to radiogenic strontium is constant. This trend is typical of fractional crystallisation. The diagonal arrow shows the trend you may see when there is crustal contamination involved during fractional crystallisation (AFC), but no data plots along this trend. The fact that strontium isotope ratios are constant with silica enrichment, coupled with consistently increasing silica values, rules out any notion that bi-modal magmatism with or without crustal contamination is a controlling factor on the physical process of the evolution of magma prior to the eruption 1300AD at Rinjani.

5.4 Depth of origin, Pressure, Temperature and water saturation of eruption

Temperatures between 1017 ºC and 675 ºC obtained from all geothermometry methods are consistent with decreasing temperature involved in fractional crystallisation. It was expected that heat of fusion in crystal formation may show an increase in temperature estimates closer to eruption as discussed in Blundy and Cashman (2001) where decompression driven (forced) crystallisation returned some temperature increases with increasing water saturation from samples at Mount St Helens. This was not observed suggesting force for crystallisation was not decompression/ascent driven. Geobarometry methods from early stable mineral phases (assuming fractional crystallisation) such as clinopyroxene and orthopyroxene returned pressures of approximately 3 kbar which reduce to 1.8 kbar for melt inclusions. This creates conflict as most melt inclusions were

from pyroxene mineral phases and therefore should return similar pressure values. This may be due to the silica methods incorporating melt inclusions from a small amount of plagioclase phenocrysts also. Interestingly, glass analysis alone showed an increase in pressure with an average value of 2.5 kbar. Increased pressure created by volatile exsolution prior to eruption could account for this, as volatiles escape the melt in the form of bubbles (vesicles) at water saturated conditions. The petrographic observations of vesicle dense groundmass are consistent with this interpretation.

Contrary to the last statement, constant silica values compared with changing water saturation from methods outlined in Putrika (2005), follow the syn-eruptive degassing trend from discussions in Blundy and Cashman (2008). Alternatively, individual interpretation of Figure 20 could suggest that data plots along the decompression H_2O saturated, Isobaric H_2O saturated or isobaric undersaturated trends. The roughly vertical trend (syn-eruptive degassing) is chosen to fit the data best although other trends are not ruled out. This trend then suggests that water saturation was independent of pressure and temperature within the magma beneath Rinjani 800 years ago, until the time of eruption where degassing occurred simultaneously, rather than being a causing factor of eruption. The stability of hornblende within the magma from petrographic observations is consistent with this theory as the magma may have been stable right up until eruption conditions, although this theory still does not explain the cause of eruption.

5.5 Modelling crystallisation sequence

The fact that mineral phases, element concentrations, water saturation, pressure and temperatures obtained in experimental simulations using Pele are almost completely consistent with petrographic observations and major element analysis implies that the program is a good analytical tool to investigate sub magmatic processes synthetically.

This implication can only be confidently applied with subduction settings that involve fractional crystallisation as the dominant physical process of magma differentiation, as this was the only physical process using the simulations to return analogous results with calculated data.

As the Pele simulation at 2000 bar fit the trend in changes of titanium as a function of silica enrichment (Figure 23), it may be interpreted that the mineral phases and compositions reached of the Rinjani Pumice and its melt inclusions and glass groundmass did so at pressures around 2 kbar and between temperatures of 1500 ºC and 900 ºC. It is unlikely that the pressure within the magma chamber remained at 2 kbar during the whole fractionation process and therefore, the simulations ran where the resulting composition of executions were at 2000 bar, were re-ran at 1500 and 1000 bar to give a better indication of pressure conditions within the magma chamber prior to eruption. The experiment executed at 2000 bar with the resulting composition being executed to crystallise at 1000 bar (Figure 25) shows a much more consistent trend than the 2000 bar and 1500 bar trends in Figure 24. Again, an even tighter trend in silica enrichment with titanium movement between the whole rock and major element data and experimental simulations is seen for the Pele execution of the same starting composition at 2000bar and the resulting composition at 1000bar. This execution has been adopted as fitting the calculated data most consistently. The fact that silica enrichment between values of 55 and 64 wt % SiO_2 is independent of changes in titanium composition, shows that fractionation became independent of crystallisation. In order for this interpretation to be possible, the magma must have become physically separated between andesite and dacite composition to allow for a shift in overall silica enrichment independent of associated elemental changes. This interpretation is

consistent with somewhat opposite behaviour seen in the SiO_2 versus K_2O harker diagram (Figure 32), where also at the transition between andesite and dacite composition (according to silica values), there is an independent enrichment of potassium in the magma. If a dacitic liquid had been physically separated from crystal rich andesite magma, potassium would be incompatible during fractional crystallisation at this stage and show to be enriched in the dacite liquid compared to that of the andesite magma.

5.6 Evolution leading to the 1300AD Rinjani Pumice

The data presented here is unsystematic without a model in which it is applied. Figure 34 proposes a model interpretation for the source, petrogenesis, and plumbing at Gunung Rinjani, Lombok 1300AD.

The DEM from Figure 1 shows previous volcanism on Lombok island to have fluctuated laterally roughly trending west-south-west to east-north-east prior to the 1300AD eruption. It is suggested here that volcanism originally occurred directly to the west of Rinjani and the magma path then moved east to form the Rinjani composite volcano.

The magma model in Figure 34 shows a primitive melt ascending from basalt composition via decompression/ascent driven crystallisation from a proposed lower reservoir. Fractional crystallisation drives crystallisation of high temperature minerals such as plagioclase, clinopyroxene, orthopyroxene, magnetite and hornblende. Whole rock data shows the andesite to have silica weight percent values between 50 and 55%. The fractionating magma is seen in Figure 34 to pool in a magma chamber at around ~3 kbar, consistent with calculated and experimental data. Temperature proposed for this

chamber is ~1015 °C with water saturation calculated using CPX-Liquid methods of ~3.7 %. Olivine, typically being the first mineral phase to crystallise, returned thermometry values of ~989 °C. This temperature would be associated with a basalt parent of the andesite magma, where heat of fusion involved in forcing crystallisation with decompression has increased the temperature of the magma by the time it has fractionated to andesite composition. Low normalised HSFE values obtained from crystals formed in the andesite are consistent with a magma that is pertaining to its primitive parent end member. The presence of hornblende in abundance and the fact that it is viewed to form euhedral crystals is consistent with the calculated temperature, pressure and water content of this shallow andesitic magma chamber. Figure 30 shows that typically hornblende is stable at temperatures <1050 °C, pressures <2 kbar when water saturation is approximately 3.7 kbar. This suggests that the andesite magma chamber hosts the initiation of hornblende crystallisation.

Decompression driven crystallisation continues to force crystallisation of pyroxenes, hornblende, magnetite and to a lesser extend plagioclase due to the pressure and temperature conditions. Plagioclase becomes a less stable phase with decreasing pressure and temperature in water undersaturated conditions. This is supported by positive Eu and Sr values from trace element variation spidergrams, where usually, these elements would be partitioned to plagioclase growth but are in fact becoming concentrated in the fractionating magma.

Electron Microprobe analysis of melt inclusions entrained in the dominant crystal phases of the andesite magma reveal an evolved silica content of ~66 wt % SiO_2, more evolved than the whole rock data of the andesite with values between 50 and 55% SiO_2.

This exposes a magma crystallising minerals associated with andesite, with an evolved interstitial melt of dacite composition (shallow reservoir, Figure 34).

Calculated data reveals pressure values from most methods to be ~3 kbar. This isobaric condition suggests that the andesite magma has become concentrated in crystals and therefore becoming denser, may have reached its maximum crystallinity holding it back from further ascent.

It is a typical thought that in arc settings, magmas cool progressively as they near the surface. As proposed by Blundy and Cashman (2001), forced decompressional crystallisation is associated with heat produced by formation of crystals known as 'heat of fusion'. Therefore, where you would typically expect to see a decrease in temperature as the melt fractionates, the andesite temperature is observed not to vary significantly due to the forced crystallisation keeping the magma body hot. As it has been assumed the dacite magma did not fractionate significantly from when it existed as interstitial liquid within the andesite magma, heat of fusion maintaining heat within the magma may be a possible explanation for the lack of quartz not being a crystallising phase within the pumice, as quartz will not typically form until temperature becomes <850 ºC.

Brophy (1991) discusses the physical control of critical crystallinity versus chamber convection in fractionating magmas. The discussion proposes that within a fractionating magma, if the extent of crystallisation exceeds the ability of the chamber to convect, the interconnected network of crystals 'fuses', and the interstitial melt is immediately more evolved than the crystals, more buoyant, and it ascends and separates from its parent. The displacement to higher concentration of K_2O weight percent seen at the transition in silica enrichment from andesite to dacite is supported by this theory

where potassium, acting as in incompatible element (having no crystal phase to partition to), becomes enriched during fractionation, and if the liquid it resides in becomes separated from the diluting crystals (andesite), an instant increase in the percent of potassium will be seen, but will still fit the positively proportional relationship it holds with silica enrichment (Figure 36). The physical process of magma segregation proposed by Brophy (1991) also fits with experimental models of crystallisation sequence. The synthetic modelling of the magma chamber at 2000 bar (3000 bar according to calculated data) is related to the shallow reservoir containing andesite magma in Figure 34. Crystallisation sequence from this pressure (and temperature ~1000 °C) follows the silica and titanium variation plotted from whole rock and major element data (Figure 31). The end composition of this synthetically fractionated magma re-executed at 1000 bars continues to follow the calculated variation trend in silica v titanium enrichment. Relating this to Brophy's (1991) argument, the instant enrichment in silica with constant titanium (crystallisation of magnetite being dormant) also suggests that a physical mechanism is acting upon the andesite magma to separate the evolved interstitial liquid, which immediately signatures an increase in silica values between andesite and dacite composition.

The small shallow chamber associated with the stratocone of Gunung Rinjani prior to 1300AD, is projected in Figure 34 to be the residence of the migrated dacitic liquid. The calculated depth of origin of the pumice yields a pressure of 1.8 kbar, the first shift in pressure observed from the pressures experienced in the shallow chamber holding andesite magma. Temperature calculations reveal the dacite at this stage to be ~900 °C and have an increased water content of ~5 %. It is proposed that the lack of crystals observed in the dacite petrography shows that ascent driven crystallisation did not act

upon the dacitic liquid, it only drove the magma to the initial point of andesite and dacite separation. Contrary to the statement, minor crystallisation of hornblende is thought to continue in this shallow chamber as in Figure 30 it can be seen that hornblende remains a stable phase within the melt, supported by the visual evidence of wholly crystallised hornblende phenocrysts.

Trace element variation that reveals negative Nb values is considered to possibly be due to minor contamination of the materials within the andesite cone into the dacite magma chamber.

Figure 23 from ascent driven crystallisation models published by Blundy and Cashman (2001) shows water weight percent values from calculated data of melts and associated plagioclase decrease with constant silica content. This visualisation would imply that at 1300AD, degassing of volatiles from the dacite magma happened simultaneously with the eruption (small shallow chamber conditions in Figure 34). Some data is seen to be arbitrarily plotting along other trends imposed by Blundy and Cashman (2001). This could be theorised as the fact that the data plotting along the decompression driven crystallisation trend may be relating to the driving force acting on fractional crystallisation that produced the andesite magma beneath Rinjani.

The model in Figure 34 shows the dacite stalling within the stratocone and not ascending to the vent. Although low in crystals, the elevated silica content would force the magma to become rigid and act like a plug. Petrographic observations of the pumice reveal it to overall consist of isolated clusters of entrained phenocrysts within a homogenous glass and vesicle rich matrix. These exact observations are surmised by Blundy and Cashman (2008) to be typical of volcanic plugs. The rigidity of the dacite

magma here, coupled with the magma trending toward saturation at such low pressure has given rise to the explosion of the western flank of Rinjani 1300AD (right diagram in Figure 34). Glass from fusion at time of eruption records SiO_2 wt % values of ~65, which is similar to that found within melt inclusions entrained in crystals formed in what has been referred to as the 'andesite' magma chamber. This finding reinforces that the dacite composition at time of eruption was still the same as that of the interstitial liquid of the andesite magma.

The caldera volume calculated in this paper being much larger than the DRE pumice volume discovered by Takada et al. (2004), can possibly be explained by the conjunction of the fact that the eruption occurred between what was once two stratocones (visually deceiving) and that subsequent minor cataclysm may have attributed to the large edifice volume.

The right hand diagram in Figure 34 shows that the subsequent cataclysmic eruptions to the 1300AD Rinjani Pumice have increased the volume of the caldera. The model also shows the magma ascent path migrating laterally westwards once again where active resurgent volcanism is today at Gunung Baru. This is consistent with observations previously discussed from the DEM.

Do we rule out crustal contamination?

Strontium isotope ratios suggest the fractionation process that produced the Rinjani Pumice is via fractional crystallisation alone, but there are minor signs that can be attributed to AFC processes, such as negative Nb values. As discussed, the crust beneath Rinjani is young (Miocene) and has not had time to decay radioactive strontium. This may disguise crustal contamination. The typical trend in the Sunda Arc for crustal contamination decreases from west to east in direct correlation with

continental crust component. Therefore, what seems to be fractional crystallisation may be spurious due to young and oceanic lithosphere being the contaminants in the east of the arc. In saying this, the correlation of petrography, petrogenesis and plumbing discussed here still moulds together to form a distinct fractional crystallisation model, under the influence of another magma separating physical process such as ‘critical crystallinity’, but crustal contamination cannot be ruled out.

6. CONCLUSIONS

Conditions within the sub-volcanic plumbing that drove the 1300AD eruption of the Rinjani Pumice on Lombok island are constrained to point towards fractional crystallisation processes with limited or no crustal contamination. Crustal contamination where continental crusts is present in the west of the Sunda Arc (i.e. Toba) is seen to enrich the magma significantly in silica and show varying sources of strontium isotope ratios. It is thought that the lack of continental crust may disguise this at Lombok but this theory can be overcome by assuming crustal contamination in the western Sunda Arc is due to thick crust where the crust is thin and young at Lombok.

Ascent driven crystallisation from a parent basalt drove fractional crystallisation to andesite composition beneath Rinjani volcano, where the affinity for crystallising phase was clinopyroxene, orthopyroxene, magnetite, hornblende and plagioclase respectively. Minor crystallisation of olivine, biotite and apatite is also recorded at andesite composition. Decompressional water undersaturated conditions induced ascent of the andesite magma to a shallow reservoir at ~3 kbar at temperatures ~1015 °C. Water saturation from analysis of crystals formed within the dacite yield values ~3.7 wt%. Melt inclusion data from these same crystals reveal the interstitial liquid in the andesite magma to be of evolved dacite composition (~66 wt% SiO_2) compared to the andesite (~50-54 wt% SiO_2).

Critical crystallinity exceeded the ability of the magma chamber to convect within this reservoir and therefore physical separation of the evolved dacite liquid from the andesite magma occurs. The buoyant dacitic liquid ascends to another shallow reservoir directly

beneath Rinjani volcano and reaches its saturation pressure at 1.8 kbar at a temperature of ~900 °C, with water saturation increased to ~5 wt %.

Sub-plinian cataclysmic eruption of the 1300AD Rinjani Pumice occurred due to pressure increase involved in saturation of the dacite, and syn-eruptive degassing aids in excavating the western flank of the Rinjani stratocone leaving a caldera.

Subsequent volcanism occurs where the magma ascent path migrates west producing more cataclysmic eruptions increasing the volume of the edifice. Today, resurgent volcanism can be seen in the central eastern part of Segara Anak lake at Gunung Baru within the Rinjani caldera to produce basalt and andesite lavas.

The application of physical mechanisms acting upon fractional crystallisation proposed here may be applied to other arc settings around the globe where fractional crystallisation is found to be the primary driving force of felsic end member cataclysmic eruptions at what is typically an andesitic arc.

ACKNOWLEDGEMENTS

I would like to thank the input, advice and discussions from my supervisor Professor John Foden. Also thanks goes to Professor David Giles, Andreas Schmidt Mumm, Graham Heinson, Dr. David Kelsey and Dr. Steve Hill. I cannot thank Frank Robinson enough for his help in the past year as a fellow student and a friend. Thanks also goes to Verity Normington and Hannah Pfitzner for their helpful input. I would also like to thank my partner Justin for all his support and patience in the last year, and my sister Tina for editing. The crew at Adelaide Microscopy are invaluable as they have gone out of their way to help in sample and data analysis, special thanks to Angus Netting and Ben Wade. Sample preparation was made much easier with the aid of polishing from Pontifex. Thank-you to Mark Tingay for his helpful writing hints and to John Seach from volcanolive.com for his valuable reference searching. Overall thanks is in order for the whole honours crew for being a great bunch of people and supporting one another.

REFERENCES

Anderson, J. L., A. P. W. Barth, J. L and F. Mazdab (2008). Thermometers and Thermobarometers in Granitic Systems. Reviews in Mineralogy and Geochemistry. K. Putrika and F. Tepley. **69:** 121-142.

Bernard, A., B. Barbier, R. Campion and C. Caudron. (2009). "The 2009 eruption of Rinjani volcano (Lombok, Indonesia)." Commision of Volcanic lakes (CVL) Retrieved 19th October, 2009.

Blundy, J. and K. Cashman (2001). "Ascent-driven crystallisation of dacite magmas at Mount St Helens, 1980-1986." Contrib Mineral Petrol **140**: 631-650.

Blundy, J. and K. Cashman (2008). Petrologic Reconstruction of Magma System Variables and Processes, A Systematic Approach. Minerals, Inclusions and Volcanic Processes J. J. Rosso, Reviews in Mineralogy and geochemistry. **69**.

Boudreau, A. E. (1999). PELE—a version of the MELTS software program for the PC platform. B. a Division of Earth and Ocean Sciences, Duke University, Durham, NC 27708, USA.

Bowen, N. L. (1928). The evolution of the igneous rocks. Princeton University Press. Princeton**:** 332.

Brophy, J. G. (1991). "Composition gaps, critical crystallinity, and fractional crystallisation in orogenic (calc-alkaline) magmatic systems." Contributions to Mineralogy and Petrology **109**: 173-182.

Brophy, J. G. (2009). "Decompression and H2O exsolution driven crystallisation and fractionation: development of a new model for low-pressure fractional crystallisation in calc-alkaline magmatic systems." Contrib Mineral Petrol **157**: 797-811.

Bunsen, R. W. (1851). "Uber die Processe der vulkanischen Gesteinsbildungen Islands." Ann Phys Chem **83**: 197-272.

Durocher, J. (1857). "Essai de p~trologie compar~e ou recherches sur la composition chimique et min~ralogique des roches ign~es, sur les ph~nom~nes de leur ~mission et leur classification." Ann. des Mines, Paris, Ser **11**: 217-269 and 676-681.

Elburg, M. A. (2010). "Sources and processes in arc magmatism: The crutial role of water." Geologica Belgica **13**(3): 119-134.

Elburg, M. A., V. S. Kamenetsky, J. D. Foden and A. Sobolev (2007). "The origin of medium-K ankaramitic arc magmas from Lombok (Sunda arc, Indonesia): Mineral and melt inclusion evidence." Chemical Geology **240**: 260-279.

Foden, J. (2001-2002). XRF whole rock and isotope data - Lombok suite, University of Adelaide.

Foden, J. D. (1983). "The Petrology of The Calcalkaline Lavas of Rindjani Volcano, East Sunda Arc: a Model for Island Arc Petrogenesis." Journal of Petrology **24**: 98-130.

Foden, J. D. and R. Varne (1980). "The Geology and Tectonic Setting of Quaternary - Recenet Volcanic Centres of Lombok and Sumbawa, Sunda Arc." Chemical Geology **30**: 201-226.

GoogleEarth (2009). Google Earth. E. Technologies, Data SIO, NOAA, U.S. Navy, NGA, GEBCO.

Hamilton, W. (1974). Earthquake map of the Indonesian region. M. I. Ser., U.S. Geol. Surv.**:** Map 1-875-C.

Hildreth, W. (1981). "Gradients in silicic magma chambers: Implications for lithospheric
magmatism." Journal of Geophysical Research **86**: 10153-10192.

Hutchison, C. S. (1976). "Indonesian active volcanic arc: K, Sr and RG variation with depth to the Benioff Zone. ." Geology **4**: 407-408.

Katili, J. A. (1973). On fitting certain geological and geophysical features of the Indonesian
island arc to the new global tectonics. The Western Pacific: Island Arcs, Marginal Seas, Geochemistry. P. J. Coleman. Perth, W.A., University of Western Australia Press**:** 287-305.

Kelsey, C. H. (1965). "Calculation of the C.I.P.W. norm." Mineralogical Magazine **34**: 276-282.

Lange, R. A., H. M. Frey and J. Hector (2009). "A thermodynamic model for the plagioclase-liquid hygrometer/thermometer." American Mineralogist **94**: 494-506.

Le'Maitre (1976). "The Chemical Variability of some Common Igneous Rocks." Journal of Petrology **17**: 589-598.

Lowenstern, J. B. (2000). NormCalc. NormCalc_JBL, Compilations from Kelsey (1965) and Le'Maitre (1976)**:** USGS.

Marsh, B. D. (2002). "On Bimodal differentiation by solidification front instability in basaltic magmas; Part 1, Basic mechanics." Geochemica et Cosmochimica Acta **66**: 2211-2229.

Matrais, I. B., D. Pfeiffer and L. W. Stach (1972). Hydrogeology of the Island of Lombok. Bandung, Geological Survey of Indonesia.

McBirney, A. R. (1980). "Mixing and unmixing of magmas." Journal of Volcanology and Geothermal Research **7**: 357-371.

McBirney, A. R., B. H. Baker and R. H. Nilson (1985). "Liquid Fractionation. Part I. Basic Principles and experimental simulations." Journal of Volcanology and Geothermal Research **24**: 1-24.

Newman, S. and J. B. Lowenstern (2002). "VolatileCalc: a silicate melt-H20-CO2 solution model written in Visual Basic for excel." Computer & Geosciences **28**: 597-604.

Pallister, J. S., R. P. Hoblitt, D. R. Crandell and D. R. Mullineaux (1992). "Mount St Helends a decade after the 1980 eruptions: magmatic models, chemical cycles, and a revised hazards assessment." Bulletin of Volcanology **54**: 126-146.

Putrika, K. (2008). Thermometers and Barometers for Volcanic Systems. Reviews in Mineralogy and Geochemistry. K. Putrika and F. Tepley. **69:** 61-120.

Sandiford, M. (2009). "The Indonesian - New Guinea Landform Atlas " What on Earth? Retrieved November 18, 2009.

Smith, R. L. (1979). "Ash-flow magmatism. ." Geol. Soc. Am. Spec. Pap. **180**(5-27).

Sun, S.-s. and W. F. McDonough (1989). Chemical and isotopic systematics of oceanic basalts: implications for mantle composition and processes. Magmatism in the Ocean Basins. A. D. Saunders and M. J. Norry, Geological Society Special Publication **42:** 313-345.

Takada, A., A. Nasution and R. Mulyana (2004). Eruptive history during the last 10ky for the caldera-forming eruption of Rinjani volcano, Indonesia.

FIGURE CAPTIONS

Figure 1. DEM model of Lombok island Indonesia showing previous volcanism to roughly strike ESE-WNW (Sandiford 2009). Large crator in the centre is the Rinjani caldera holding Segara Anak lake. Resurgent volcanism at Gunung Baru can be seen in the centre of the lake and the extinct stratocone vent of Rinjani flanking the eastern edge of the caldera.

Figure 2. Lombok island in relation to Indonesia, the Sunda-Banda Arc and its active volcanoes. The Java trench can be seen from the subduction of the Australian tectonic plate beneath the Eurasian plate. From Foden and Varne (1980).

Figure 3. The location of Lombok within the Sunda-Banda Arc, Indonesia. Modified from SEM from Sandiford (2009) overlain by map from Foden and Varne (1980).

Figure 4. Thin section images at 4x magnification with fields of view approximately 1.8cm across from sample Lo52. The image on the left is in plane polarised light while the image on the right is in cross polarised light. Minerals observed are plagioclase, hornblende, clinopyroxene and magnetite in order of abundance. The vesicle rich groundmass glass is approximately 40% of the field of view.

Figure 5. Thin section images at 10x magnification with fields of view approximately .75cm across from sample Lo52. The image on the left is in plane polarised light while the image on the right is in cross polarised light. Minerals observed are plagioclase and magnetite in order of abundance. The vesicle rich glassy groundmass is approximately 60% of the field of view

Figure 6. Thin section images at 10x magnification with fields of view approximately .75cm across from sample Lo52. The image on the left is in plane polarised light while the image on the right is in cross polarised light. Minerals observed are hornblende, magnetite and plagioclase. The vesicle rich glassy groundmass is approximately 75% of the field of view.

Figure 7. Thin section images at 4x magnification with fields of view approximately 1.8cm across from sample Lo52. The image on the left is in plane polarised light while the image on the right is in cross polarised light. Minerals observed are plagioclase and hornblende in order of abundance. The vesicle rich glassy groundmass is approximately 75% of the field of view. The black lines are pen marks from the sample maps.

Figure 8. Thin section images at 4x magnification with fields of view approximately 1.8cm across from sample Lo52. The image on the left is in plane polarised light while the image on the right is in cross polarised light. Minerals observed are plagioclase and hornblende in order of abundance. The vesicle rich glassy groundmass is approximately 75% of the field of view.

Figure 9. Thin section images at 4x magnification with fields of view approximately 1.8cm across from sample Lo52. The image on the left is in plane polarised light while the image on the right is in cross polarised light. Minerals observed are hornblende, plagioclase and magnetite in order of abundance. The vesicle rich glassy groundmass is approximately 85% of the field of view.

Figure 10. Thin section images at 4x magnification with fields of view approximately 1.8cm across from sample Lo52. The image on the left is in plane polarised light while the image on the right is in cross polarised light. Minerals observed are hornblende, plagioclase and magnetite in order of abundance. The vesicle rich glassy groundmass is approximately 80% of the field of view. The black lines are pen marks from the sample maps.

Figure 11. Thin section images at 4x magnification with fields of view approximately 1.8cm across from sample Lo52. The image on the left is in plane polarised light while the image on the right is in cross polarised light. Minerals observed are hornblende, magnetite and plagioclase in order of abundance. The vesicle rich glassy groundmass is approximately 75% of the field of view.

Figure 12. Thin section images at 1.5x magnification with fields of view approximately 4.5cm across from sample Lo18. The image on the right is in Plane polarised light and the image on the left is in crossed polarised light. Minerals observed are plagioclase, hornblende, magnetite and orthopyroxene in order of abundance. The vesicle rich glass groundmass accounts for approximately 80% of the field of view.

Figure 13. Grain mount images using the Leica MZ16FA from sample Lo23. The image on the left is a clinopyroxene crystal with magnetite inclusions and the image on the right is an orthopyroxene crystal that has grown around magnetite. The field of view for each image is approximately 500 microns.

Figure 14. Thin section images at 1.5x magnification with fields of view approximately 4.8cm across from sample Lo52. The image on the left is in plane polarised light while the image on the right is in cross polarised light. Minerals observed are plagioclase and orthopyroxene in order of abundance. The vesicle rich glassy groundmass is approximately 90% of the field of view.

Figure 15. Major element transect across zoned plagioclase from sample Lo52.

Figure 16. Major element transect across zoned plagioclase from sample Lo54.

Figure 17. Major element transect across zoned plagioclase from sample Lo23.

Figure 18. Major element variations for silica versus titanium, aluminium, iron, magnesium, calcium, sodium and potassium of whole rock lavas and pumice along with microprobe analysis of melt inclusions and glass.

Figure 19. Silica versus Sodium bivariate diagram. Sodium values for melt inclusions and glasses are taken from whole rock data due to microprobe analysis issues.

Figure 20. Silica versus weight percent water from output associated with plagioclase-liquid thermometry and hygrometry methods (Putrika 2005), using interpretations of crystallisation mechanism from Blundy and Cashman (2008).

Figure 21. Haplogranitic ternary diagram from Blundy and Cashman (2001). The data plotted is normalised according to albite, anorthite, quartz and orthoclase parameters.

Figure 22. Pressure calculations in relation to albite component from Blundy and Cashman (2001) haplogranite diagram. The albite 'component' from figure 21 is used in accordance with formulas outlined in Blundy and Cashman (2008) to calculate a pressure value for the stable albite phase.

Figure 23. Whole rock lava and pumice, major element melt inclusions and glass analysis plotted with output from experimental crystallisation sequence simulations using Pele© at 2000bars, 1500bars, 1000bars and 500bars.

Figure 24. Whole rock lava and pumice, major element melt inclusions and glass analysis plotted with output from experimental crystallisation sequence simulations using Pele© at 2000bars, and resulting composition, and temperature re-executed at 1500bars.

Figure 25. Whole rock lava and pumice, major element melt inclusions and glass analysis plotted with output from experimental crystallisation sequence simulations using Pele© at 2000bars, and resulting composition, and temperature re-executed at 1000bars.

Figure 26. Chondrite normative trace element variation from whole rock data.

Figure 27. Chondrite normative trace element variation from melt inclusions from sample Lo23.

Figure 28. Chondrite normative trace element variation from melt inclusions from sample Lo39.

Figure 29. Chondrite normative trace element variation from melt inclusions from sample Lo54.

Figure 30. Hornblende and associated mineral stability in a fractionating magma and variable pressure, temperature and water saturation. The red dots show the trend in evolution of the Rinjani Pumice which follows a similar pattern to the stable hornblende transect. From Elburg (2010).

Figure 31. Silica versus titanium bivariate diagram showing lava and pumice data from whole rock analysis and glass and melt inclusion data from electron microprobe analysis.

Figure 32. Silica versus potassium bivariate diagram showing **two** distinct magma bodies.

Figure 33. Previous strontium isotope analysis performed by Foden (2001-2002)

Figure 34. Model proposed for the genesis of the cataclysmic caldera forming eruption of Rinjani Pumice 1300AD. The diagram on the left describes processes that lead to the eruption while the diagram on the right shows the post eruption setting.

Figure 35. Silica versus titanium major element variation for melt inclusions and their corresponding host minerals.

Figure 36. Critical crystallinity v magma convection rates adapted from Brophy (1991). The Rinjani Pumice (dacite - magma II) can be seen separating from the andesite magma (magma I).

FIGURES

Figure 1.

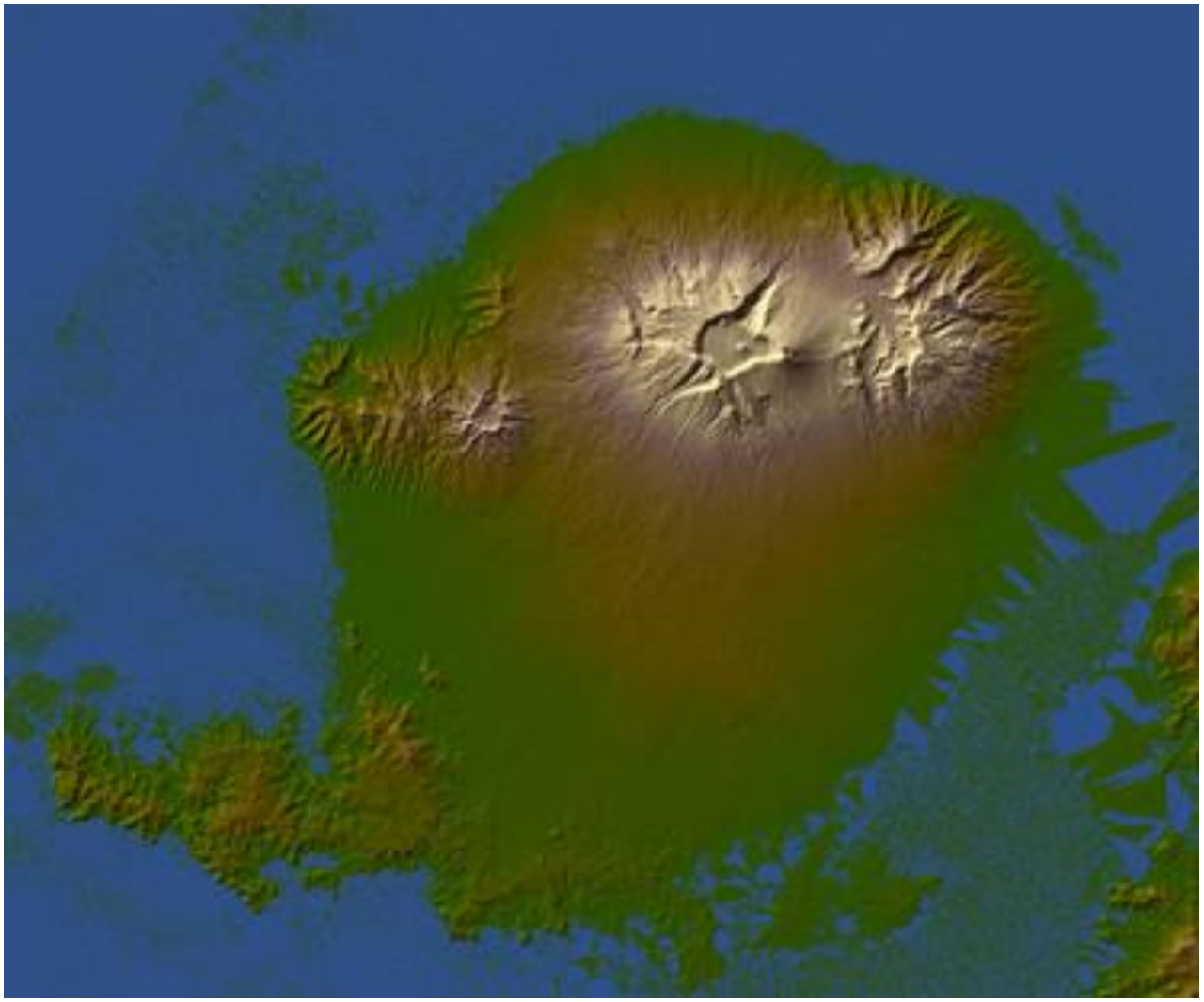

(Sandiford 2009)

Figure 2.

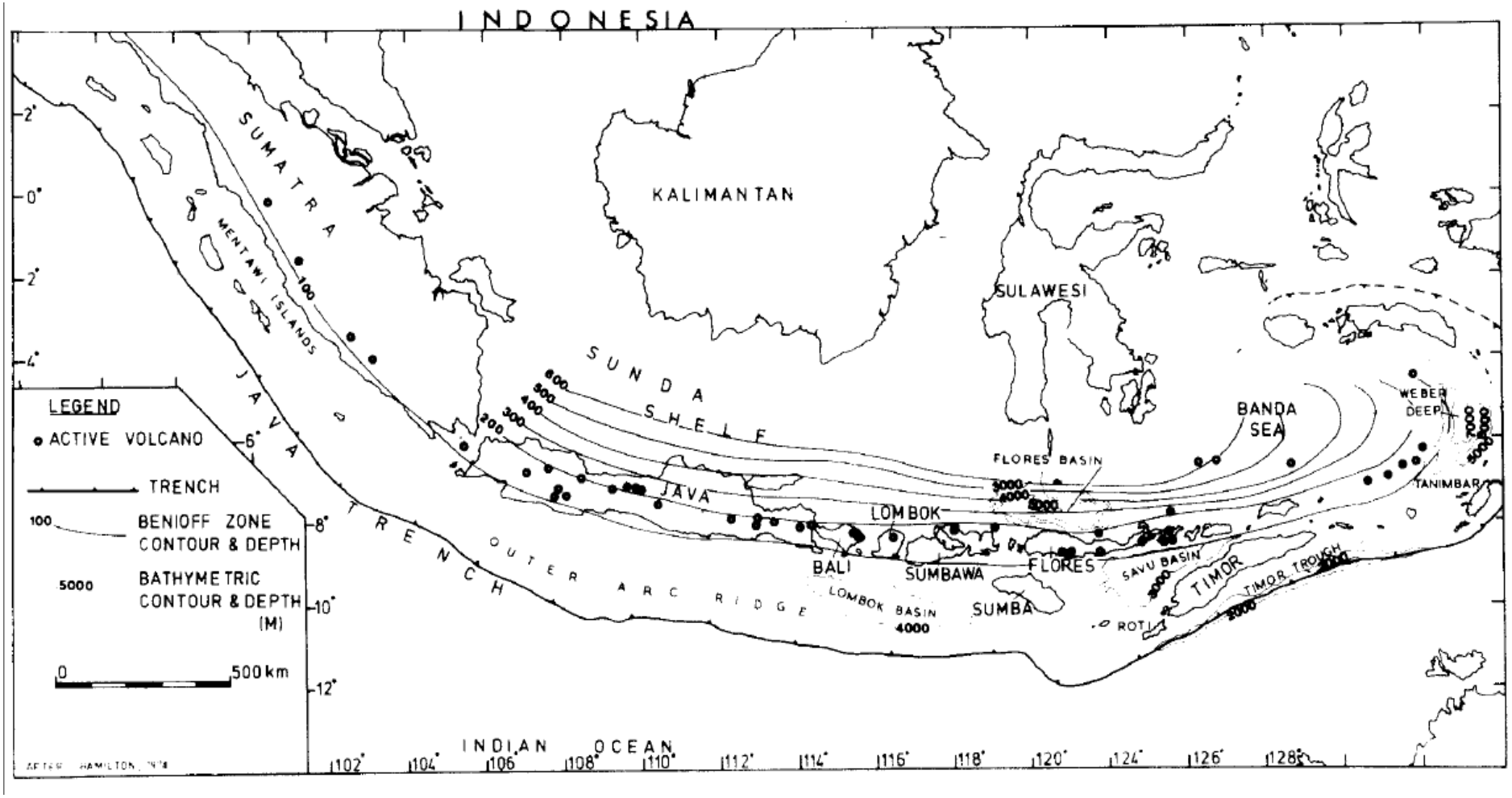

Foden and Varne (1980)

Figure 3.

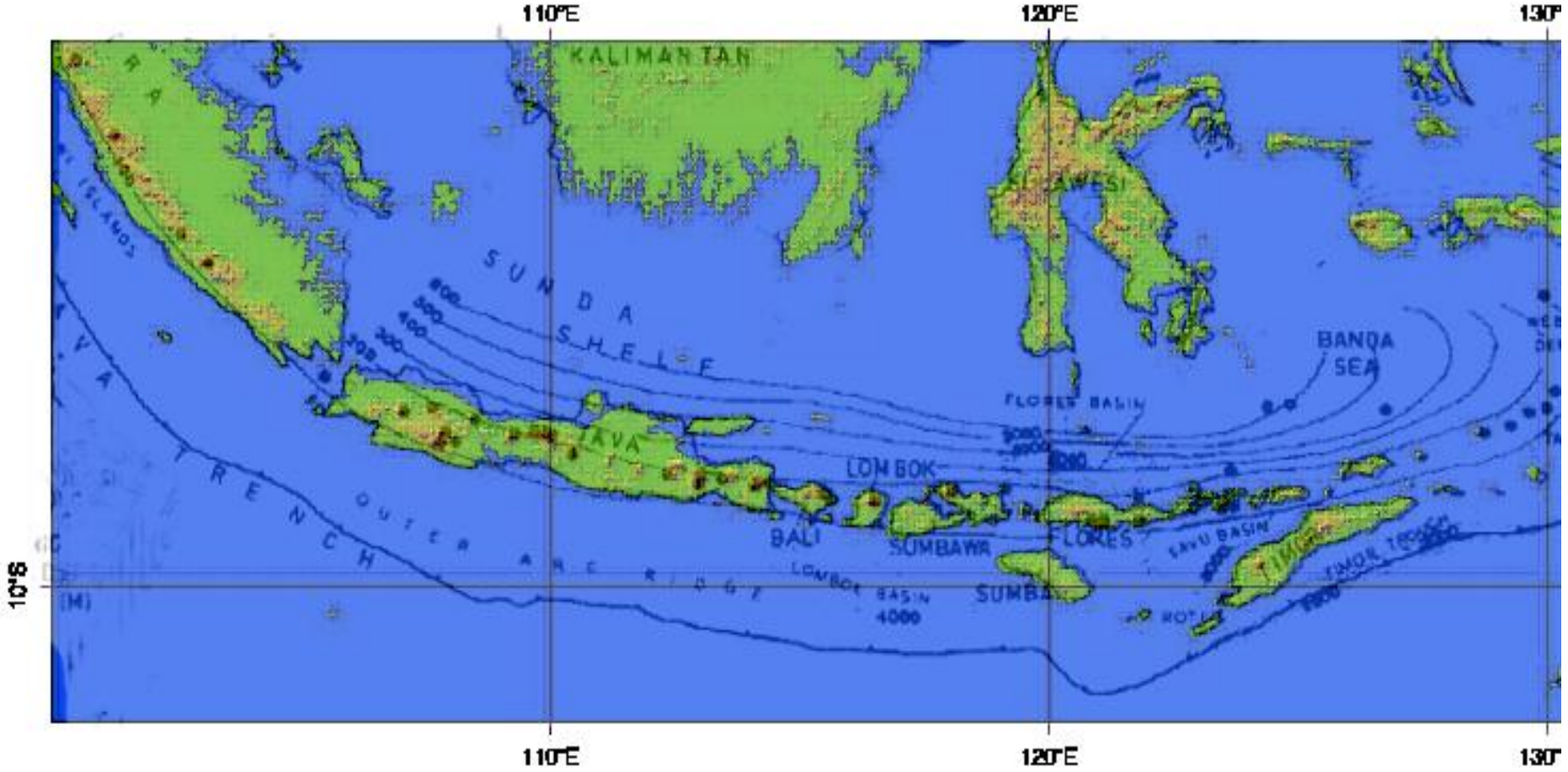

DEM from Sandiford (2009) overlain with map from Foden and Varne (1980)

Figure 4.

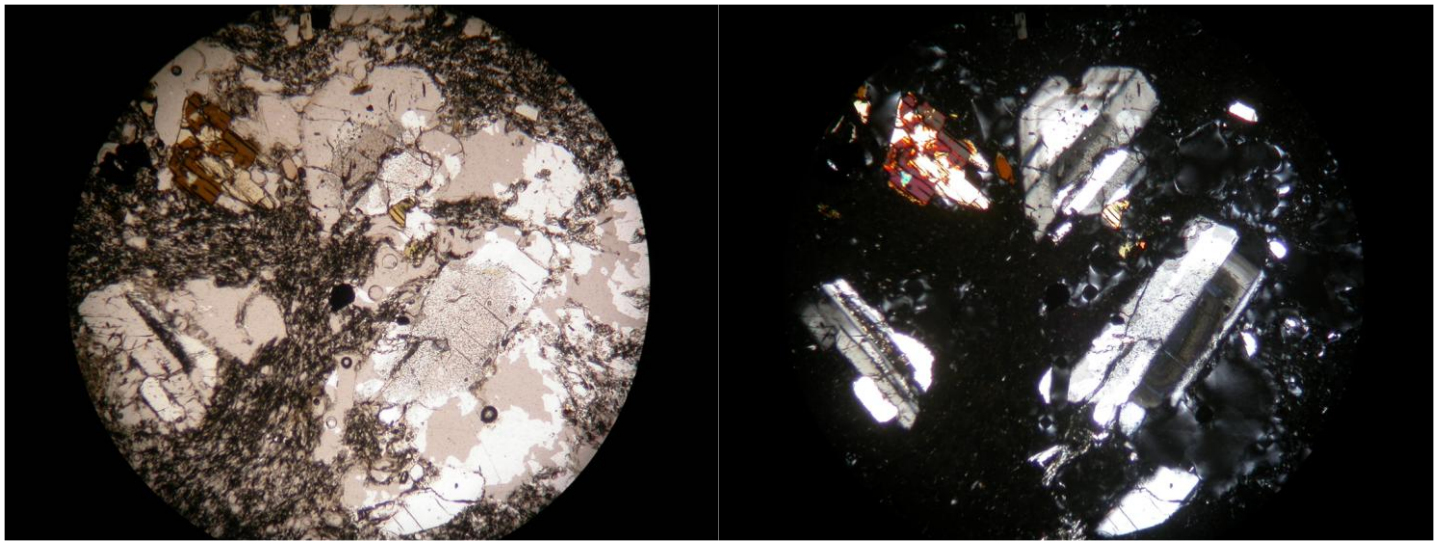

Figure 5.

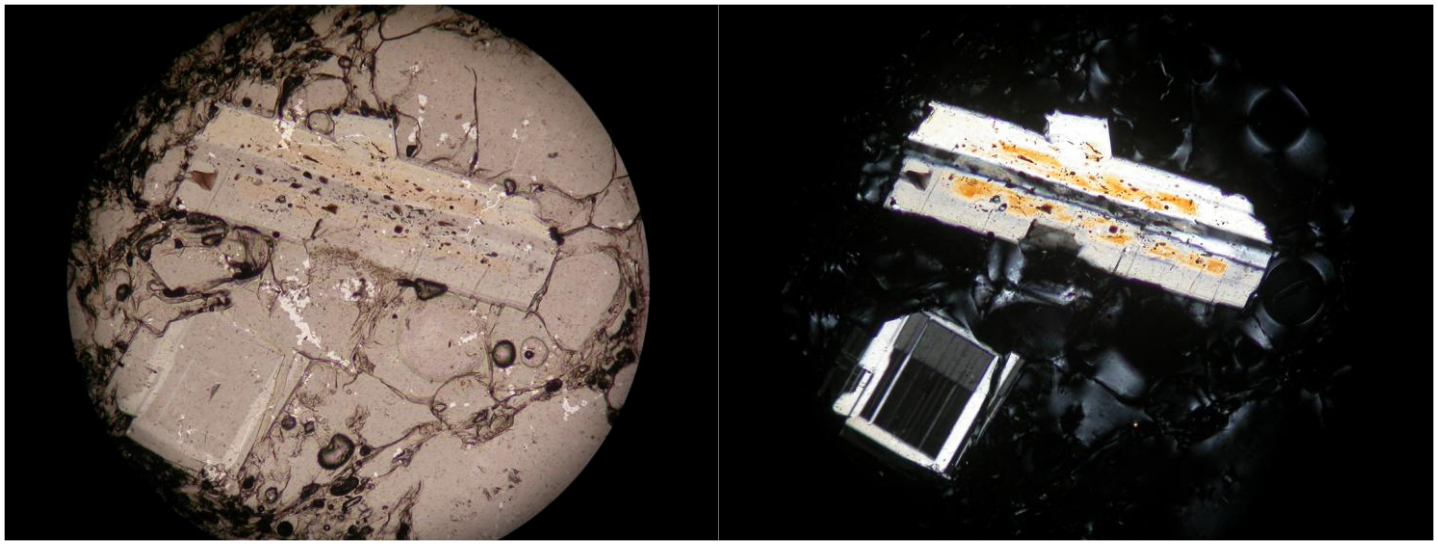

Figure 6.

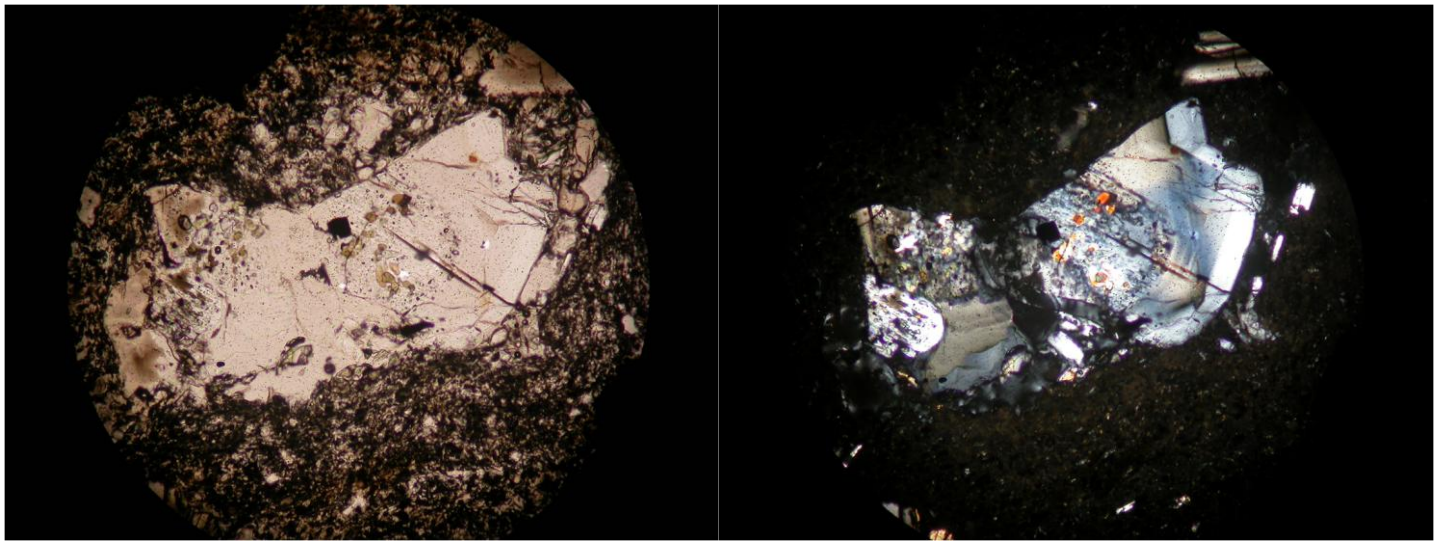

Figure 7.

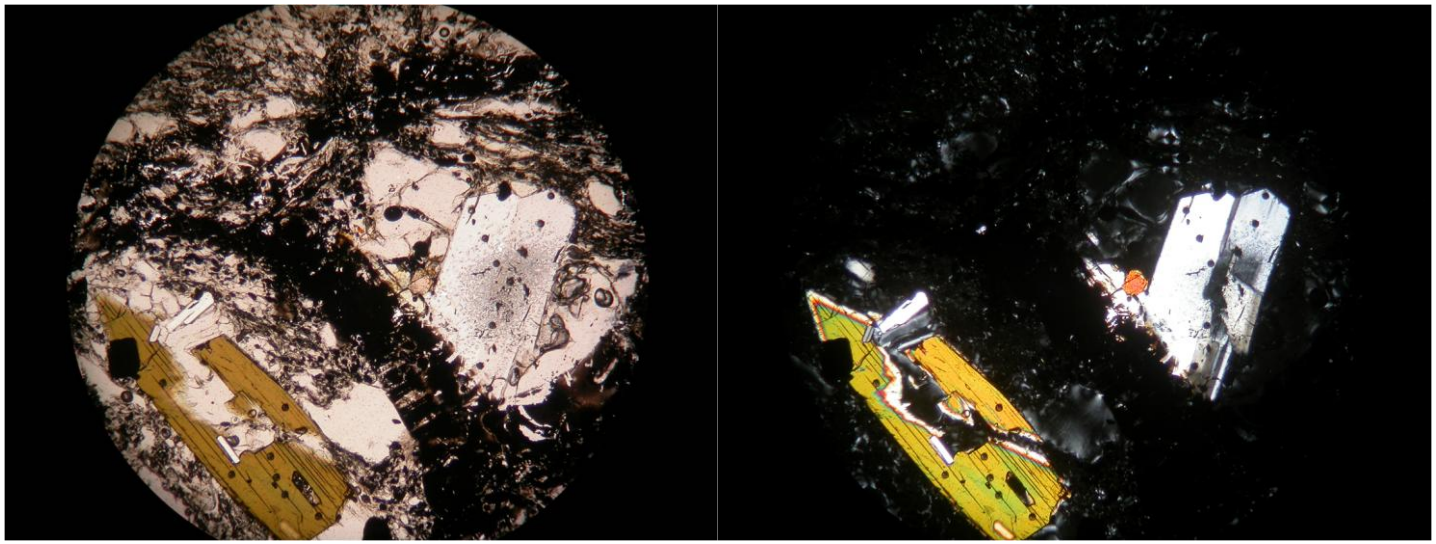

Figure 8.

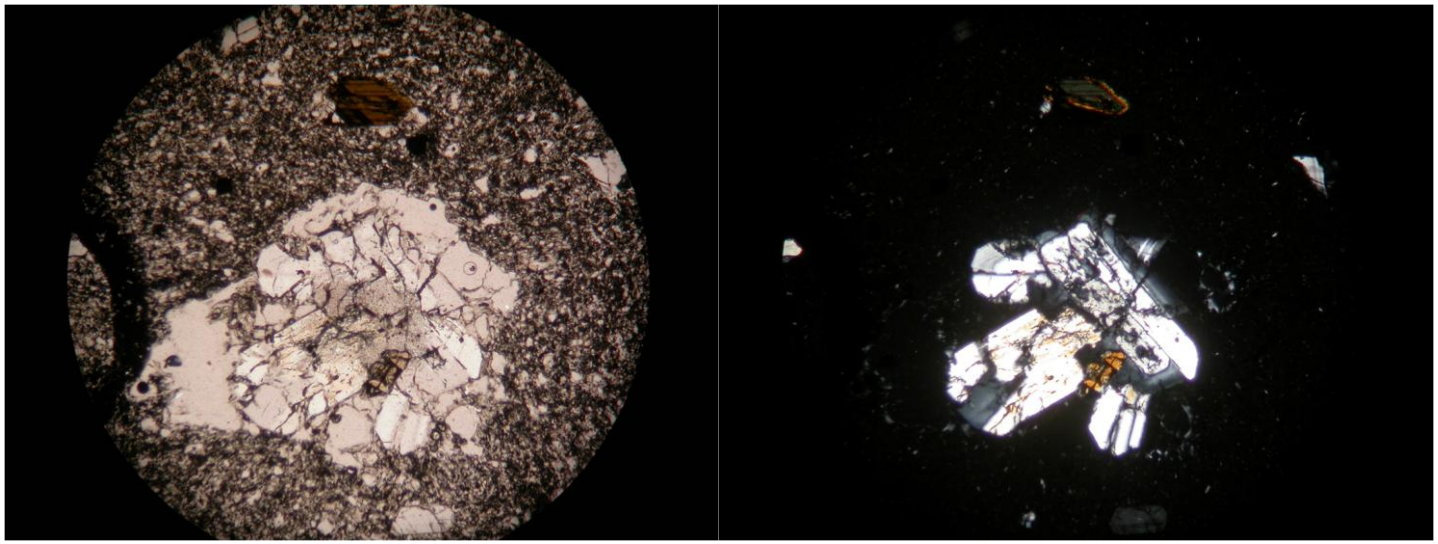

Figure 9.

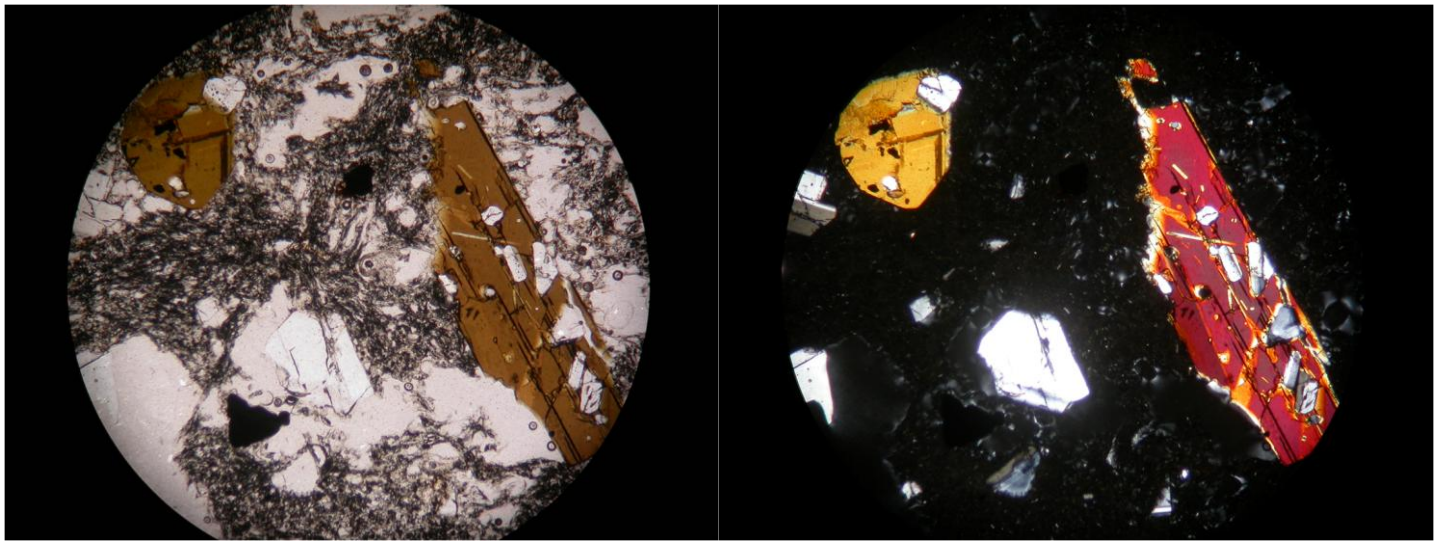

Figure 10.

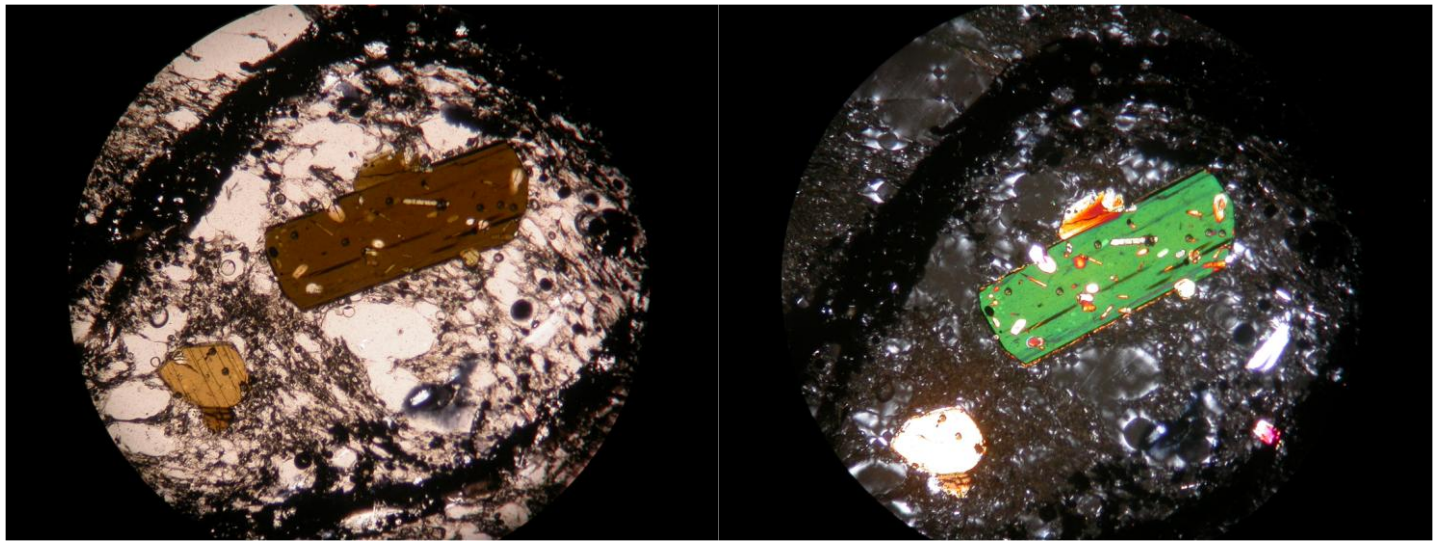

Figure 11.

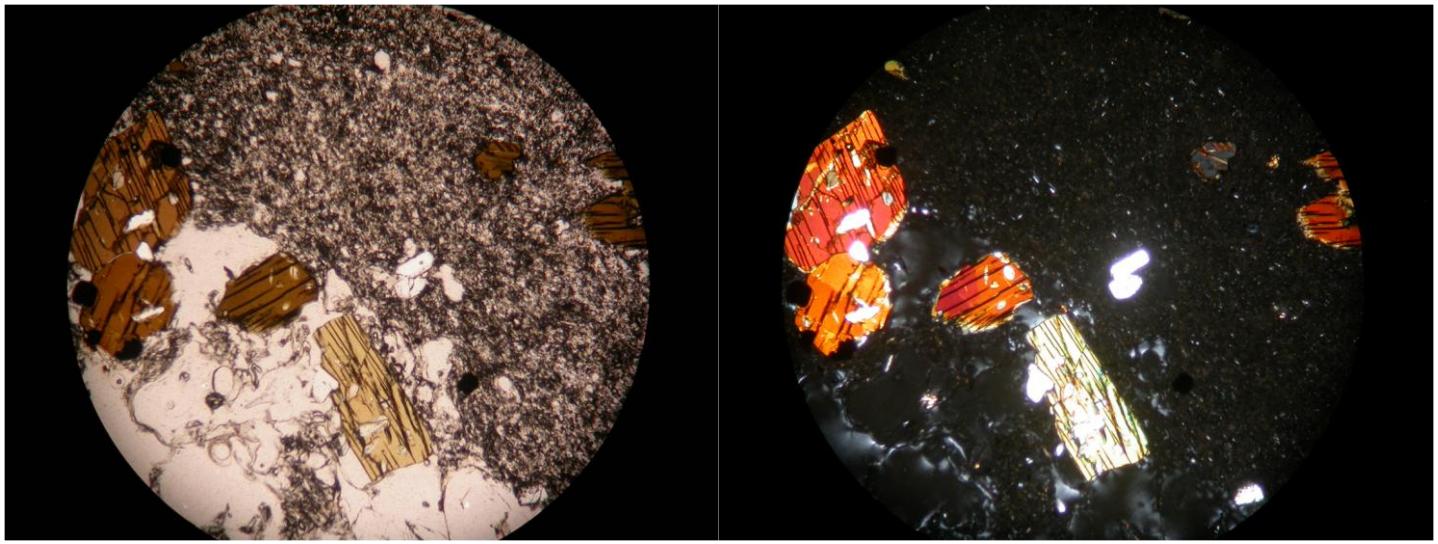

Figure 12.

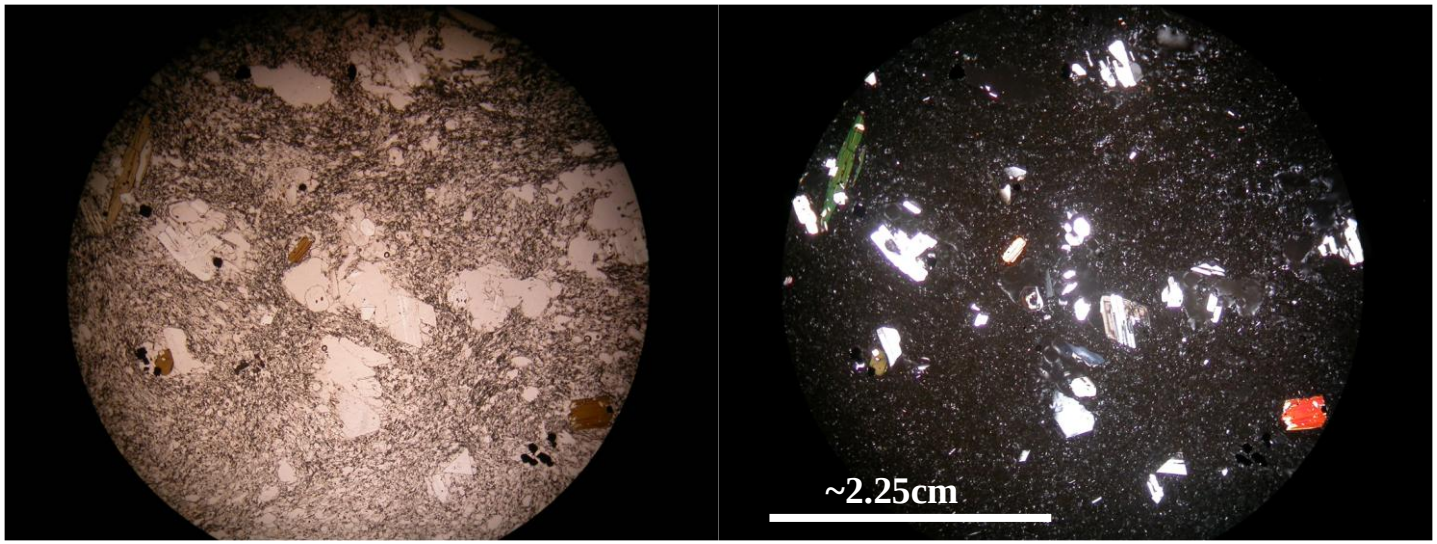

Figure 13.

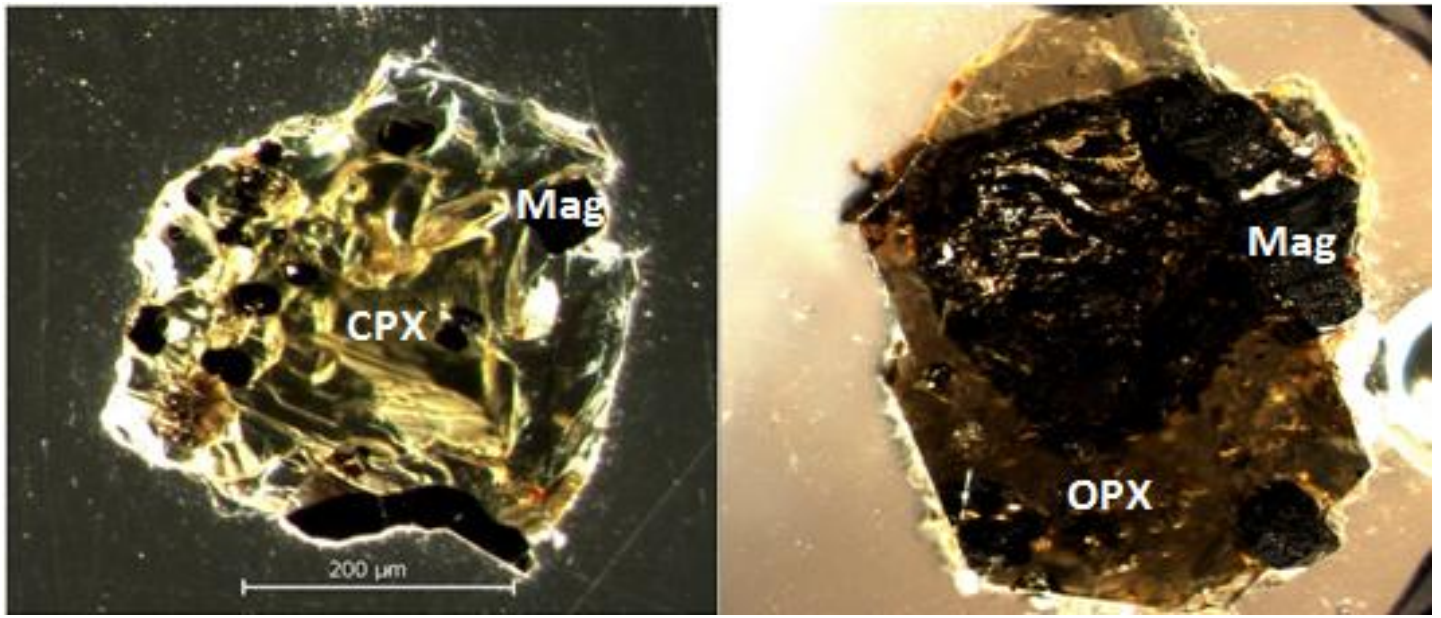

Figure 14.

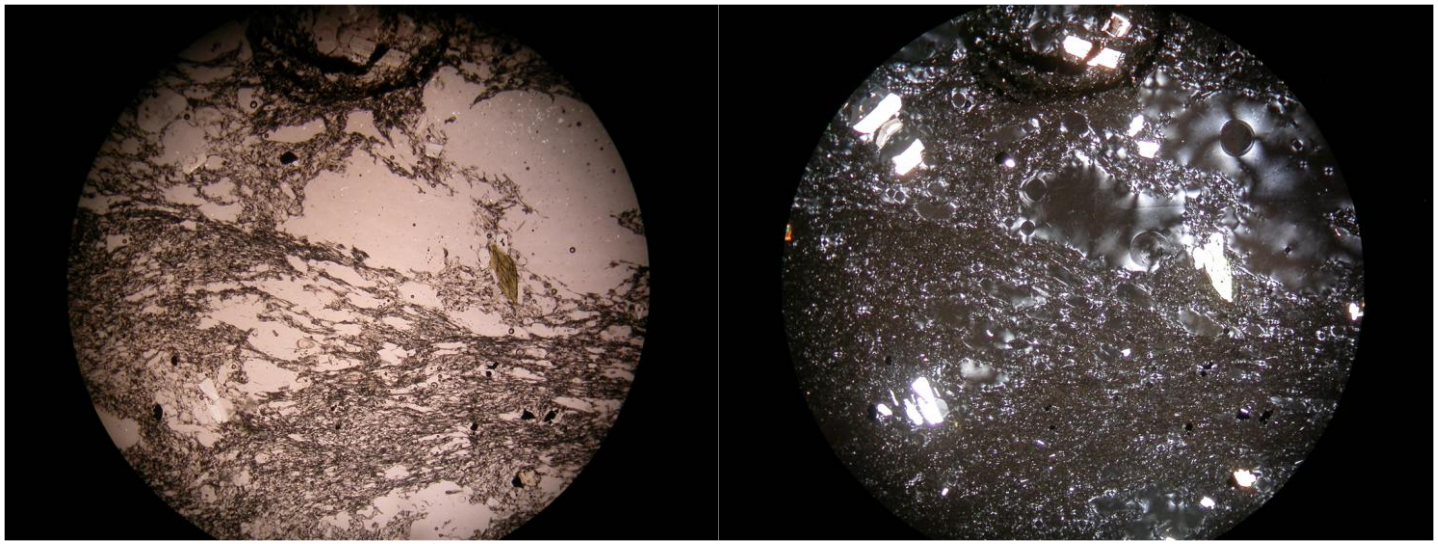

Figure 15.

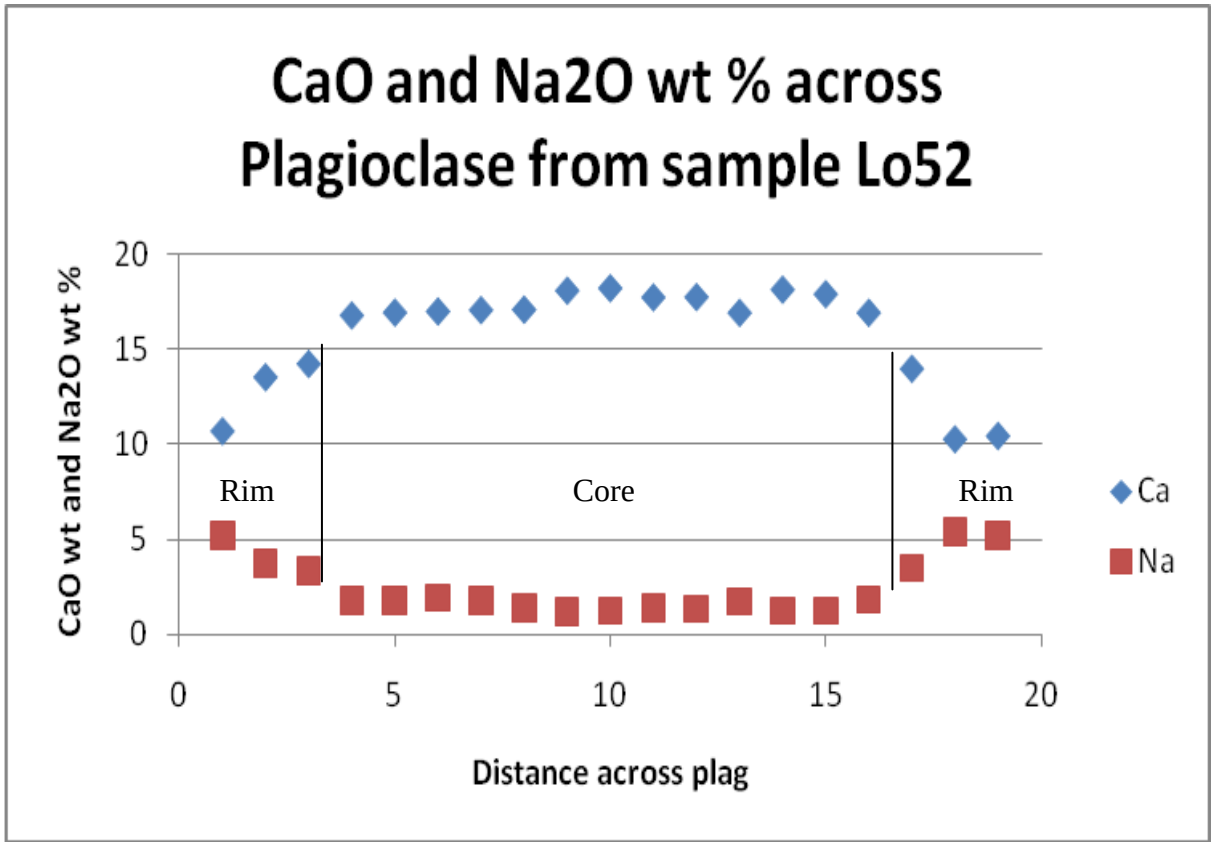
CaO and Na2O wt % across Plagioclase from sample Lo52
CaO wt and Na2O wt %
20
15
10
5
0
0
5
10
15
20
Distance across plag
Rim
Core
Rim
Ca
Na

Figure 16.

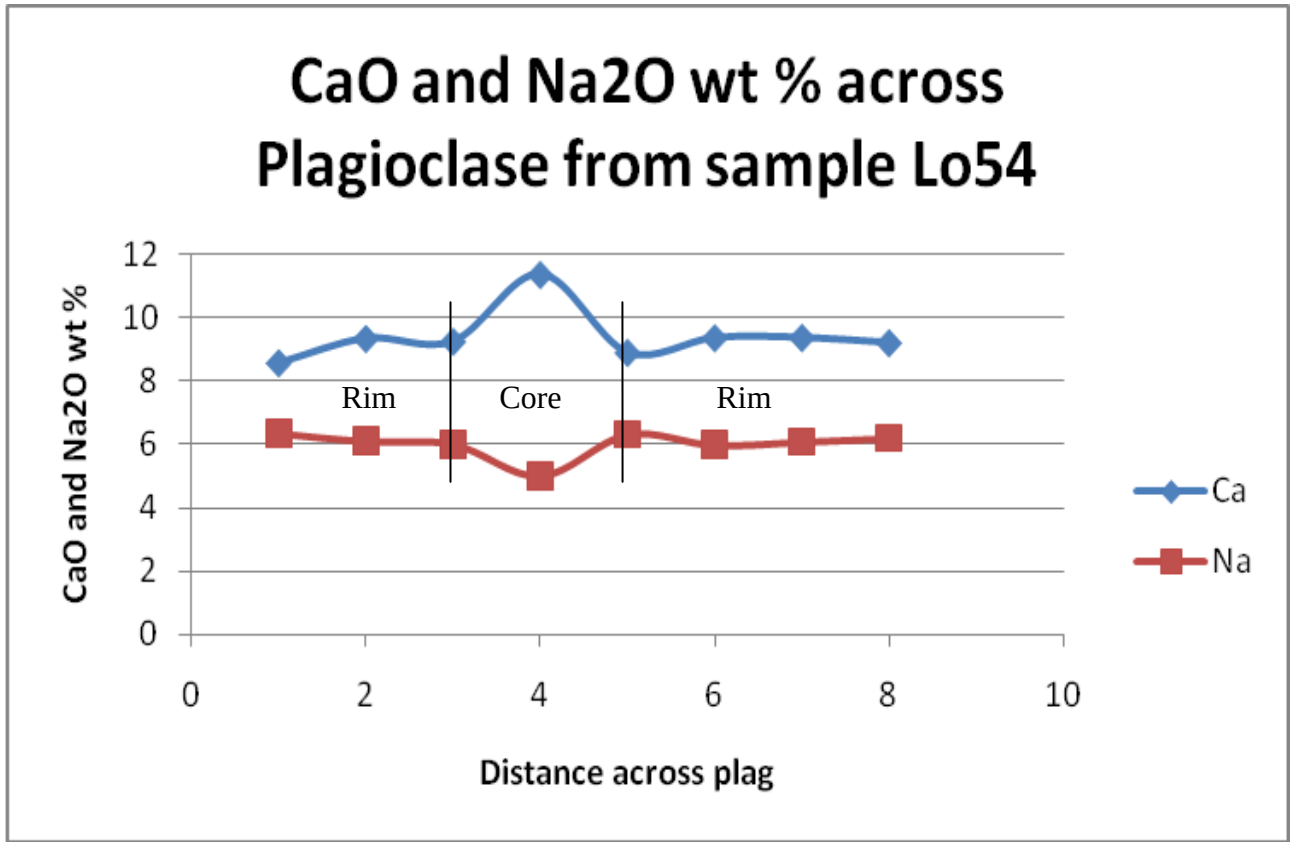
CaO and Na2O wt % across Plagioclase from sample Lo54
CaO and Na2O wt %
12
10
8
6
4
2
0
0
2
4
6
8
10
Distance across plag
Rim
Core
Rim
Ca
Na

Figure 17.

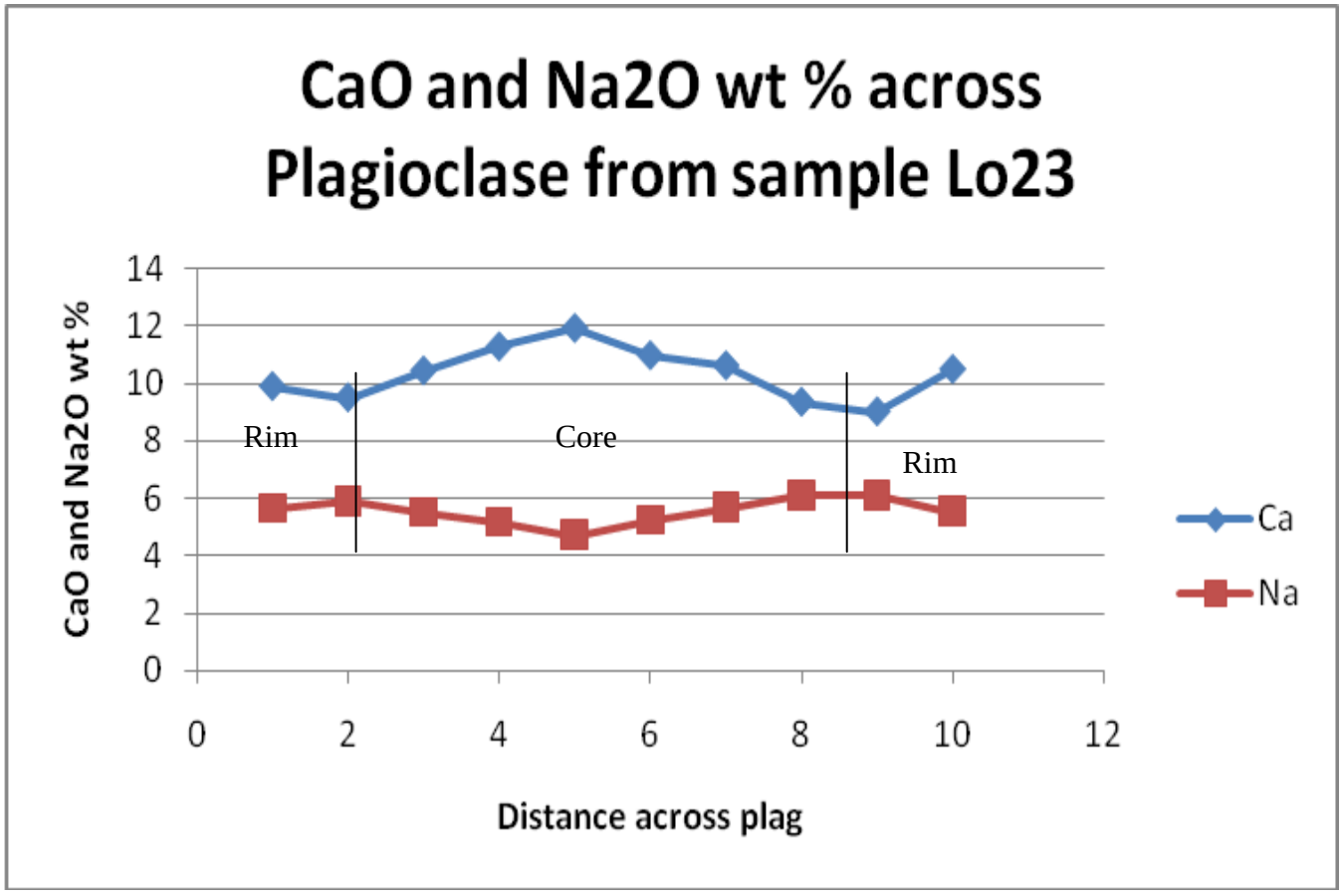
CaO and Na2O wt % across Plagioclase from sample Lo23
CaO and Na2O wt %
14
12
10
8
6
4
2
0
0
2
4
6
8
10
12
Distance across plag
Rim
Core
Rim
Ca
Na

Figure 18.

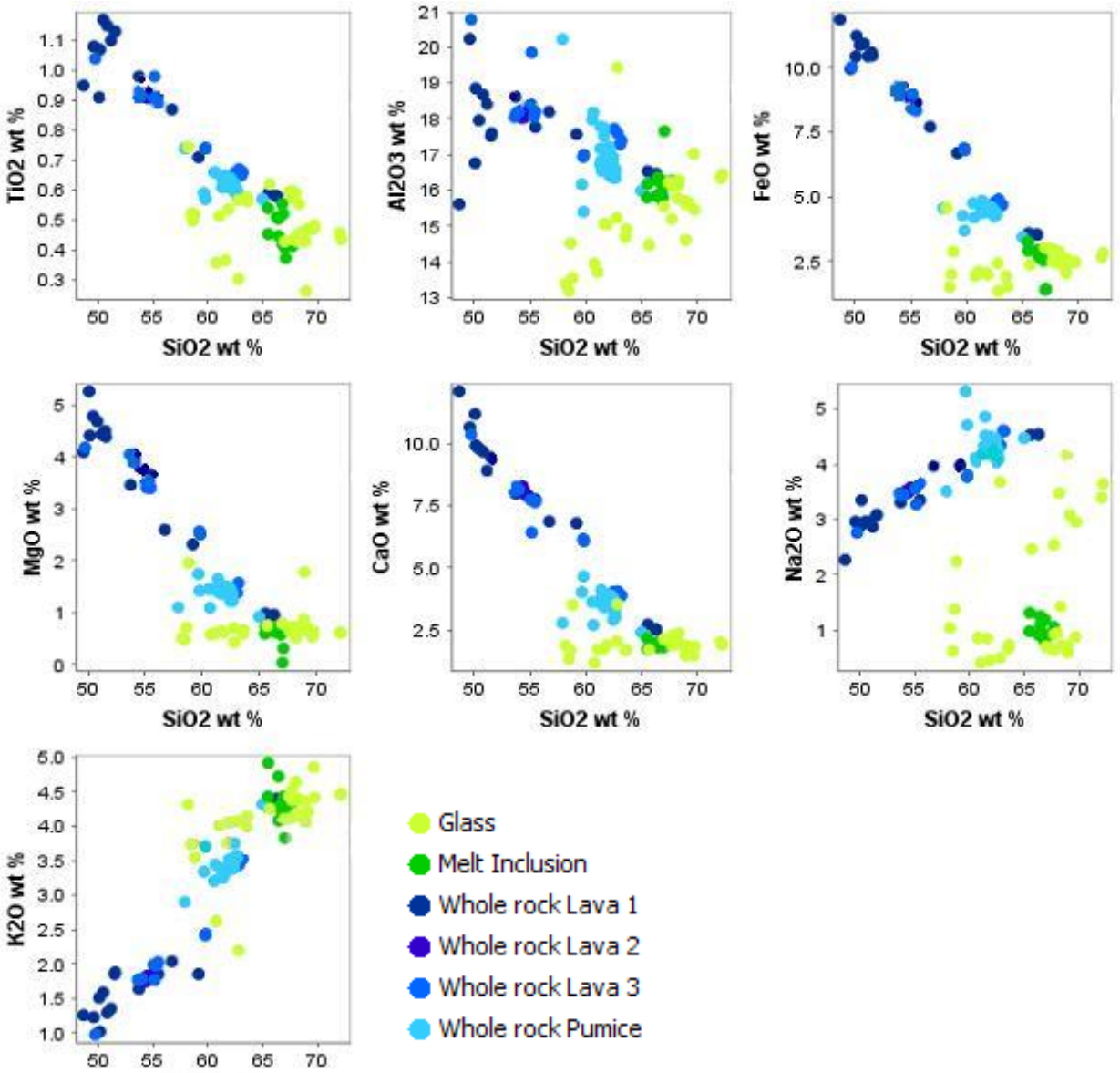
TiO2 wt %
SiO2 wt %
Al2O3 wt %
SiO2 wt %
FeO wt %
SiO2 wt %
MgO wt %
SiO2 wt %
CaO wt %
SiO2 wt %
Na2O wt %
SiO2 wt %
K2O wt %
Glass
Melt Inclusion
Whole rock Lava 1
Whole rock Lava 2
Whole rock Lava 3
Whole rock Pumice

Figure 19.

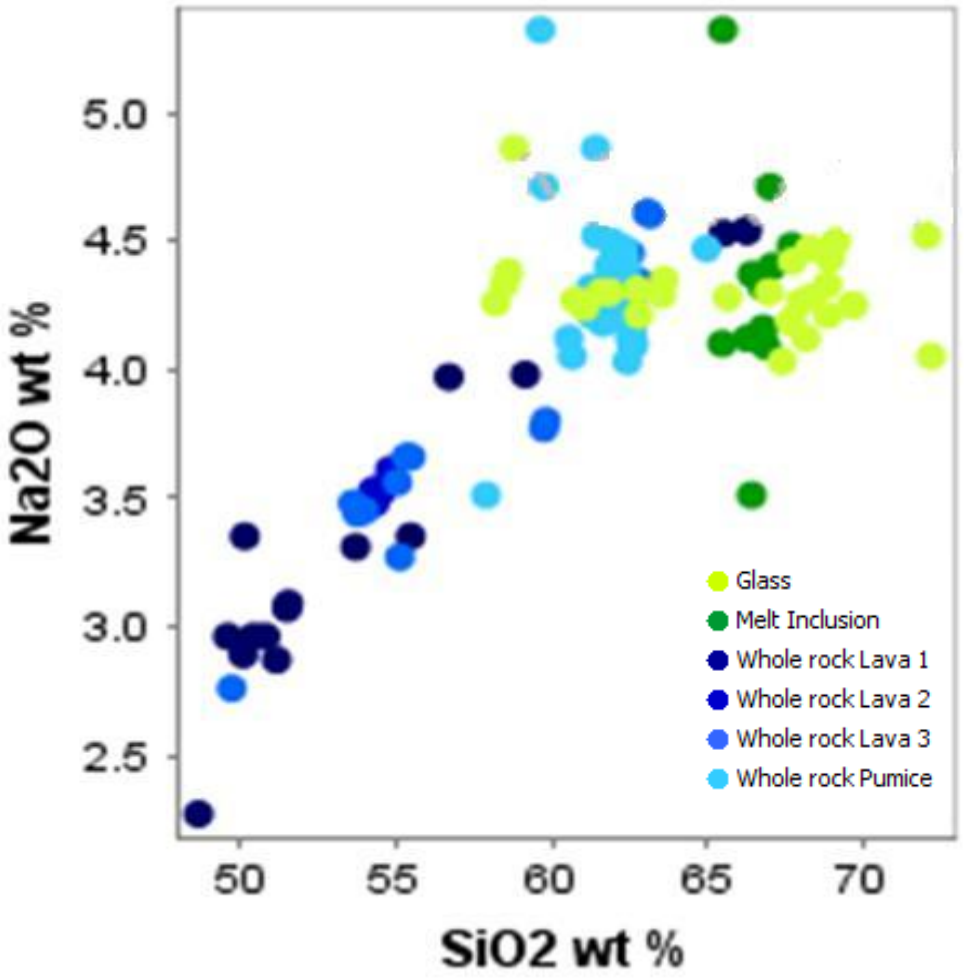
5.0
4.5
4.0
3.5
3.0
2.5
Na2O wt %
50
55
60
65
70
SiO2 wt %
Glass
Melt Inclusion
Whole rock Lava 1
Whole rock Lava 2
Whole rock Lava 3
Whole rock Pumice

Figure 20.

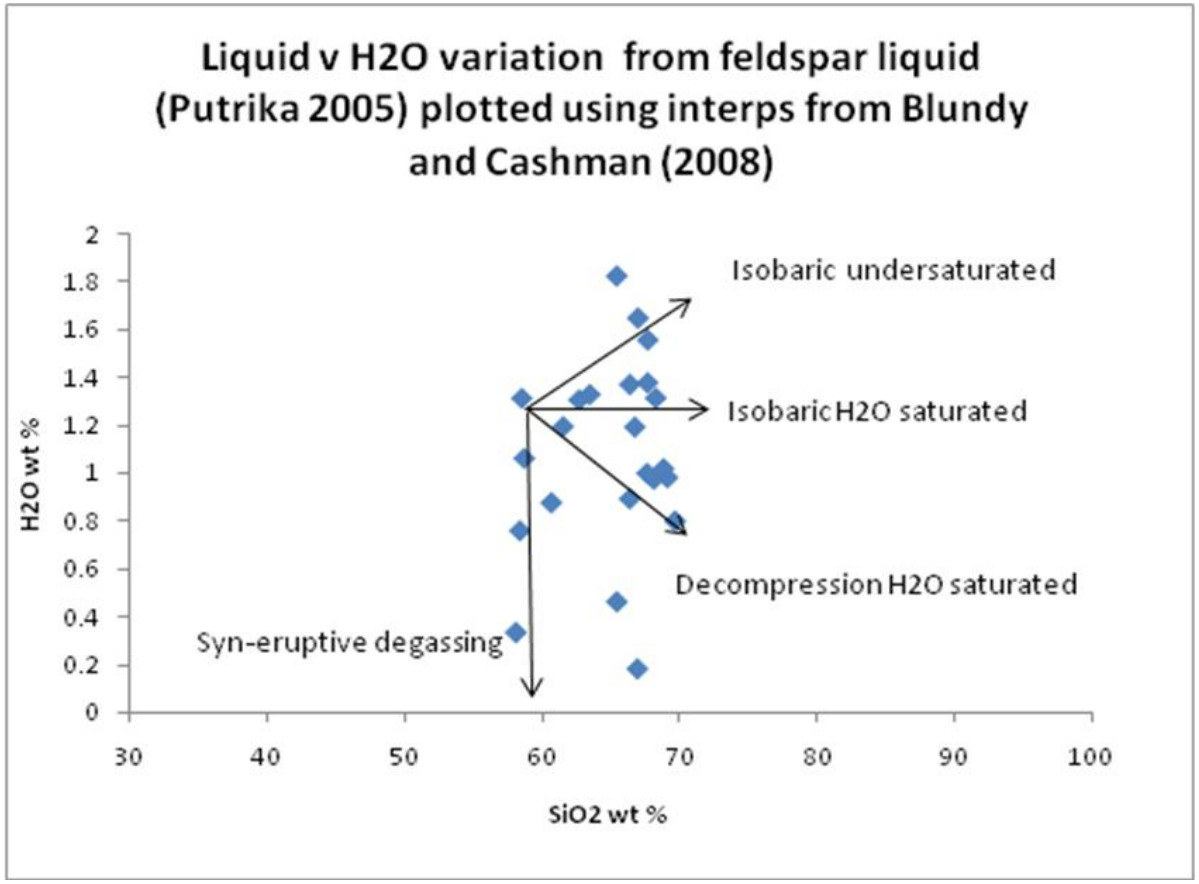
Liquid v H2O variation from feldspar liquid (Putrika 2005) plotted using interps from Blundy and Cashman (2008)
Isobaric undersaturated
Isobaric H2O saturated
Decompression H2O saturated
Syn-eruptive degassing
H2O wt %
SiO2 wt %
0
0.2
0.4
0.6
0.8
1
1.2
1.4
1.6
1.8
2
30
40
50
60
70
80
90
100

Figure 21.

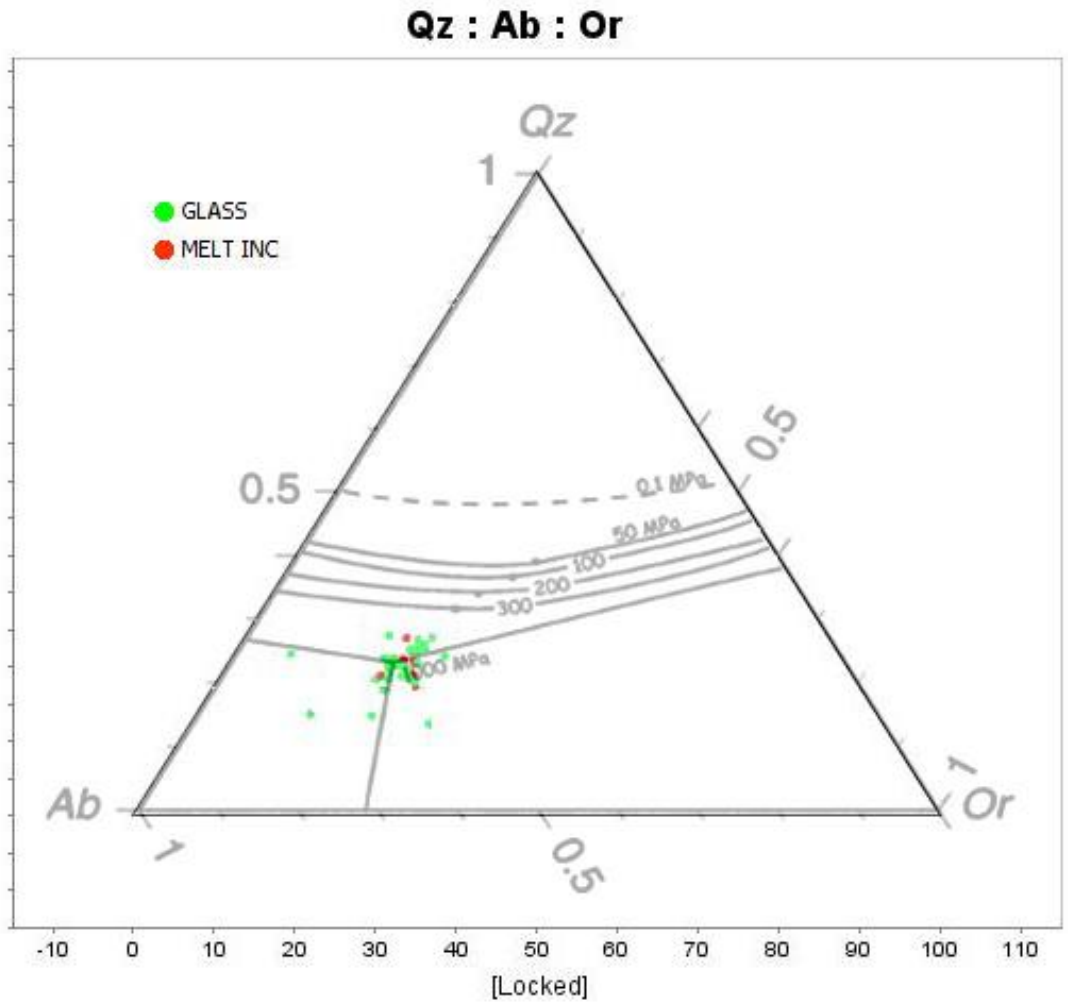
Qz : Ab : Or
Qz
1
0.5
GLASS
MELT INC
0.1 MPa
50 MPa
100
200
300
500 MPa
0.5
1
Ab
Or
-10
0
10
20
30
40
50
60
70
80
90
100
110
[Locked]

Figure 22.

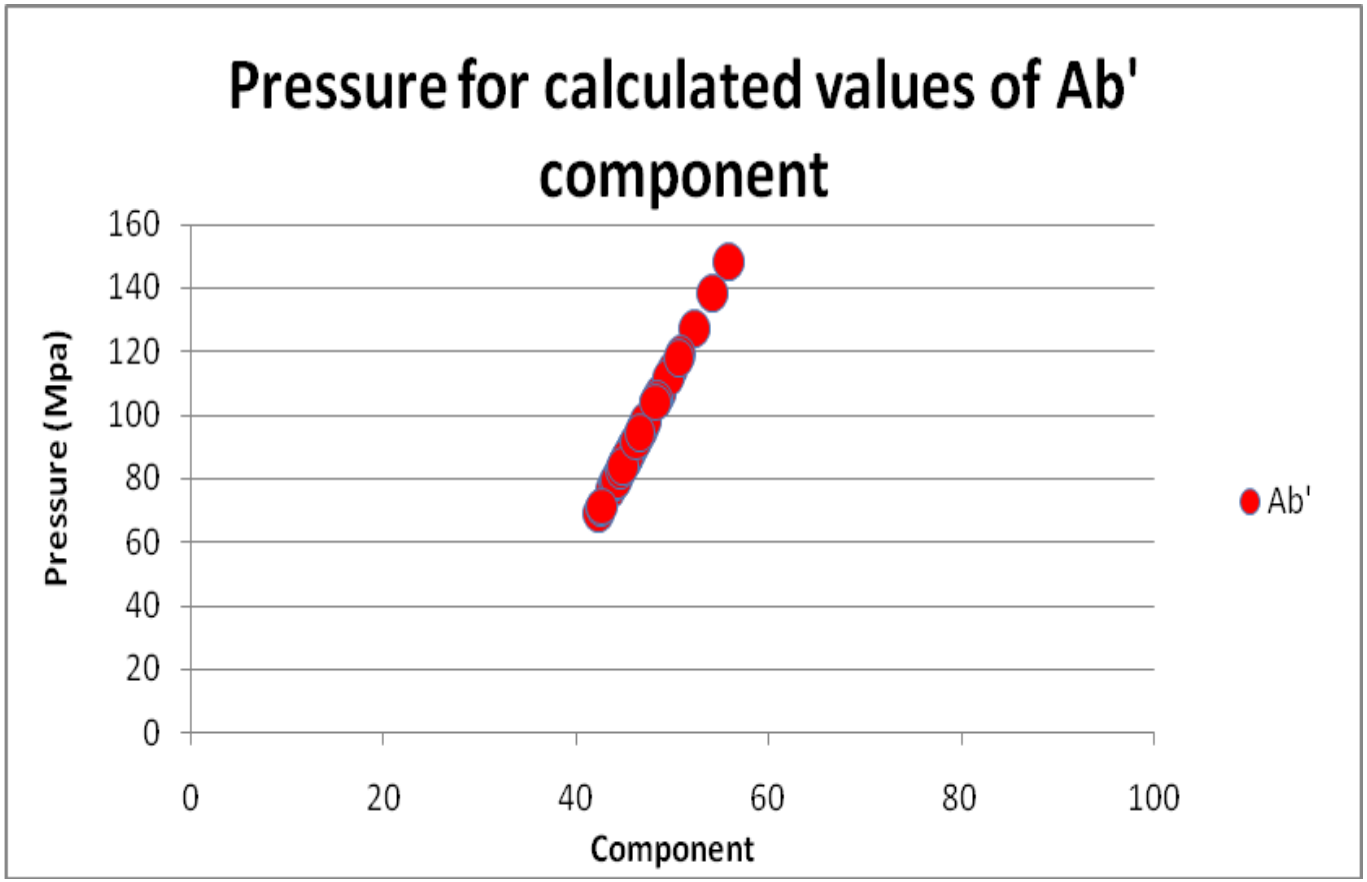
Pressure for calculated values of Ab' component
Pressure (Mpa)
160
140
120
100
80
60
40
20
0
0
20
40
60
80
100
Component
Ab'

Figure 23.

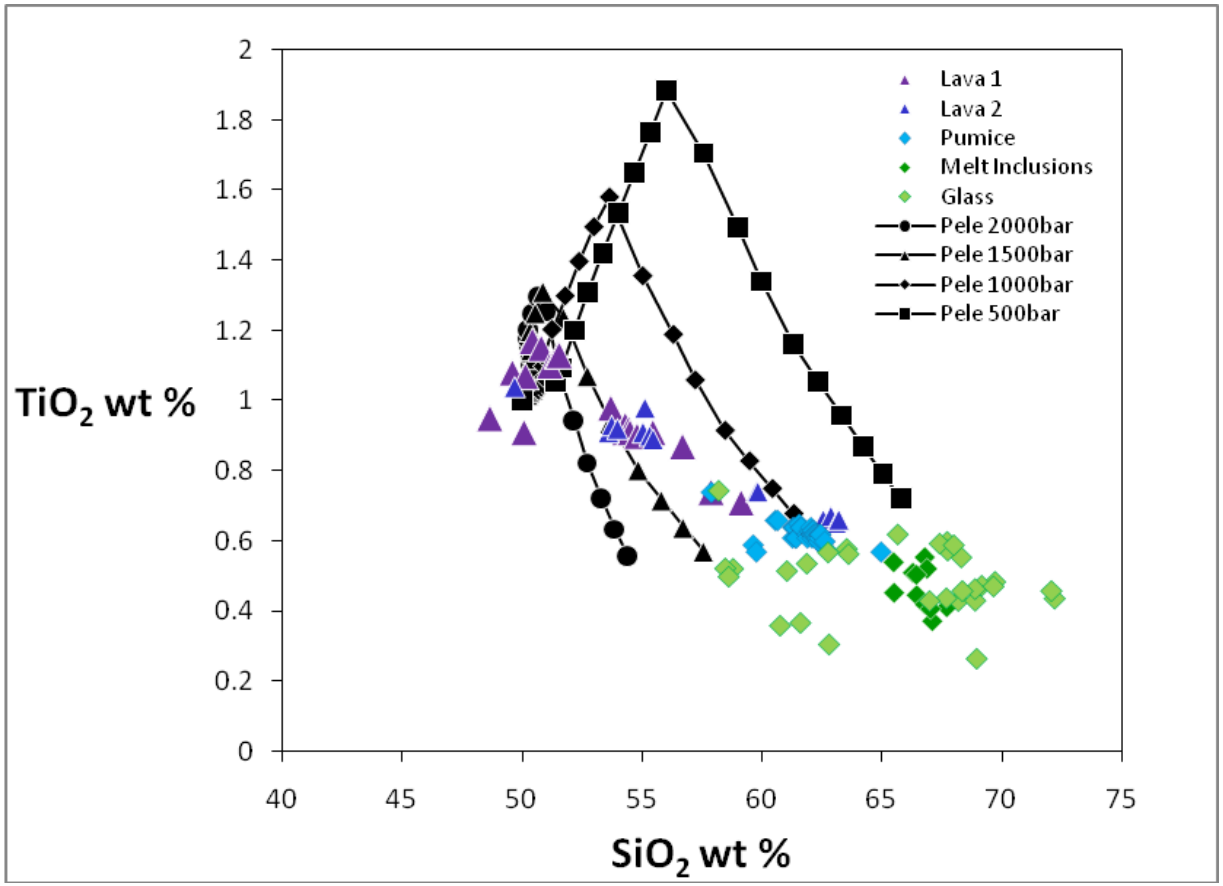
TiO2 wt %
SiO2 wt %
2
1.8
1.6
1.4
1.2
1
0.8
0.6
0.4
0.2
0
40
45
50
55
60
65
70
75
Lava 1
Lava 2
Pumice
Melt Inclusions
Glass
Pele 2000bar
Pele 1500bar
Pele 1000bar
Pele 500bar

Figure 24.

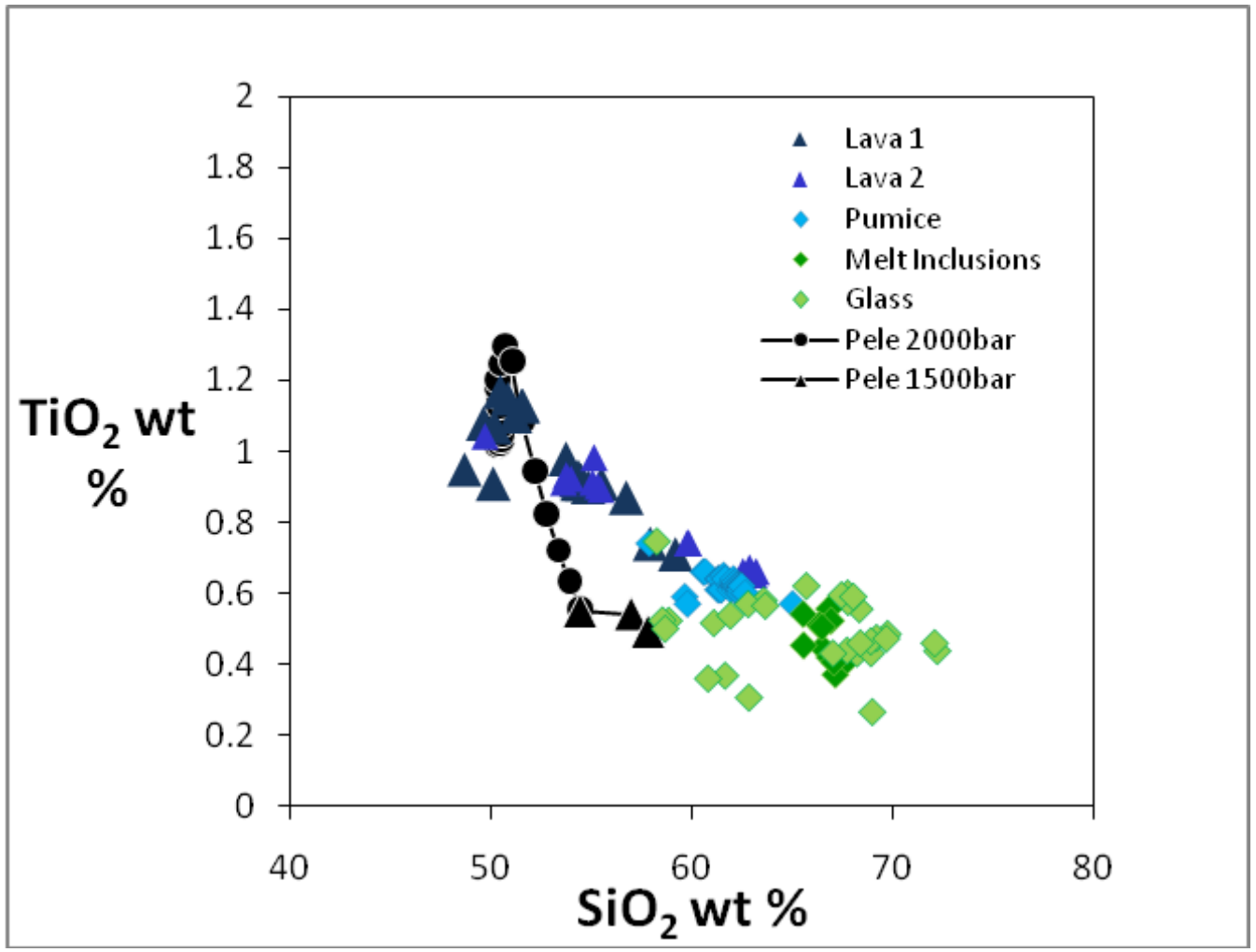
Lava 1
Lava 2
Pumice
Melt Inclusions
Glass
Pele 2000bar
Pele 1500bar
TiO2 wt %
SiO2 wt %
2
1.8
1.6
1.4
1.2
1
0.8
0.6
0.4
0.2
0
40
50
60
70
80

Figure 25.

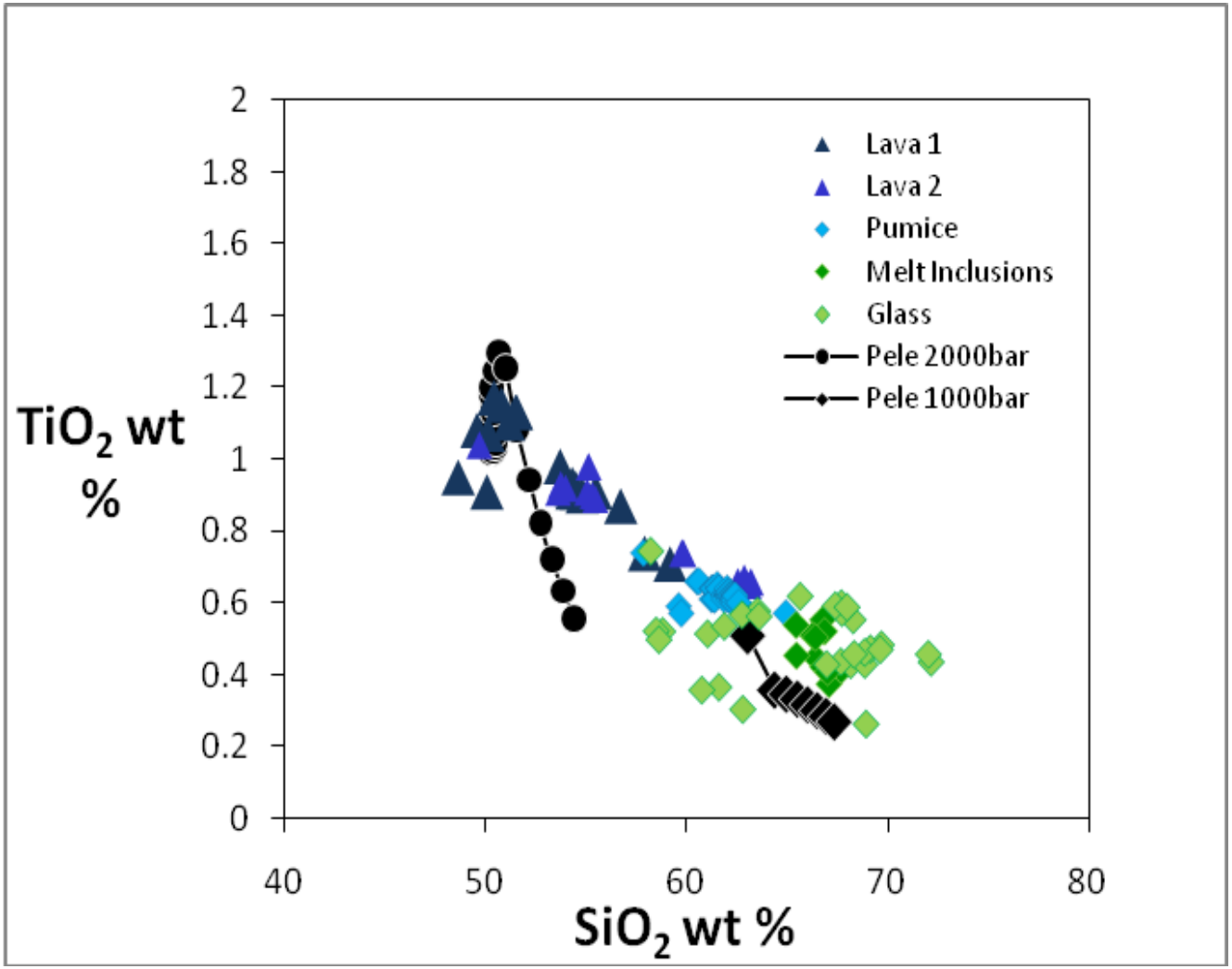
2
1.8
1.6
1.4
1.2
1
0.8
0.6
0.4
0.2
0
40
50
60
70
80
TiO2 wt %
SiO2 wt %
Lava 1
Lava 2
Pumice
Melt Inclusions
Glass
Pele 2000bar
Pele 1000bar

Figure 26.

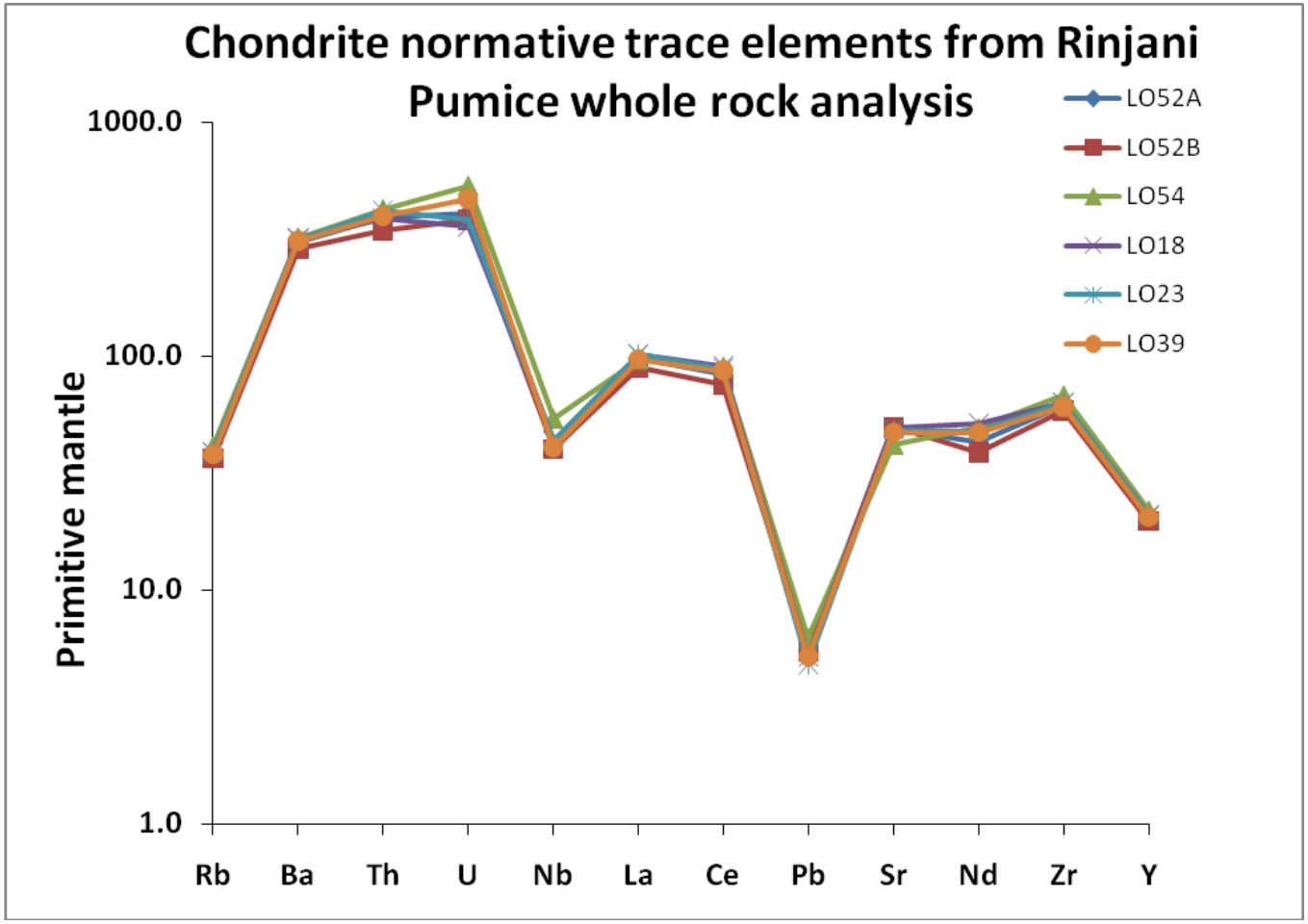
Chondrite normative trace elements from Rinjani
Pumice whole rock analysis
LO52A
LO52B
LO54
LO18
LO23
LO39
1000.0
100.0
10.0
1.0
Primitive mantle
Rb
Ba
Th
U
Nb
La
Ce
Pb
Sr
Nd
Zr
Y

Figure 27.

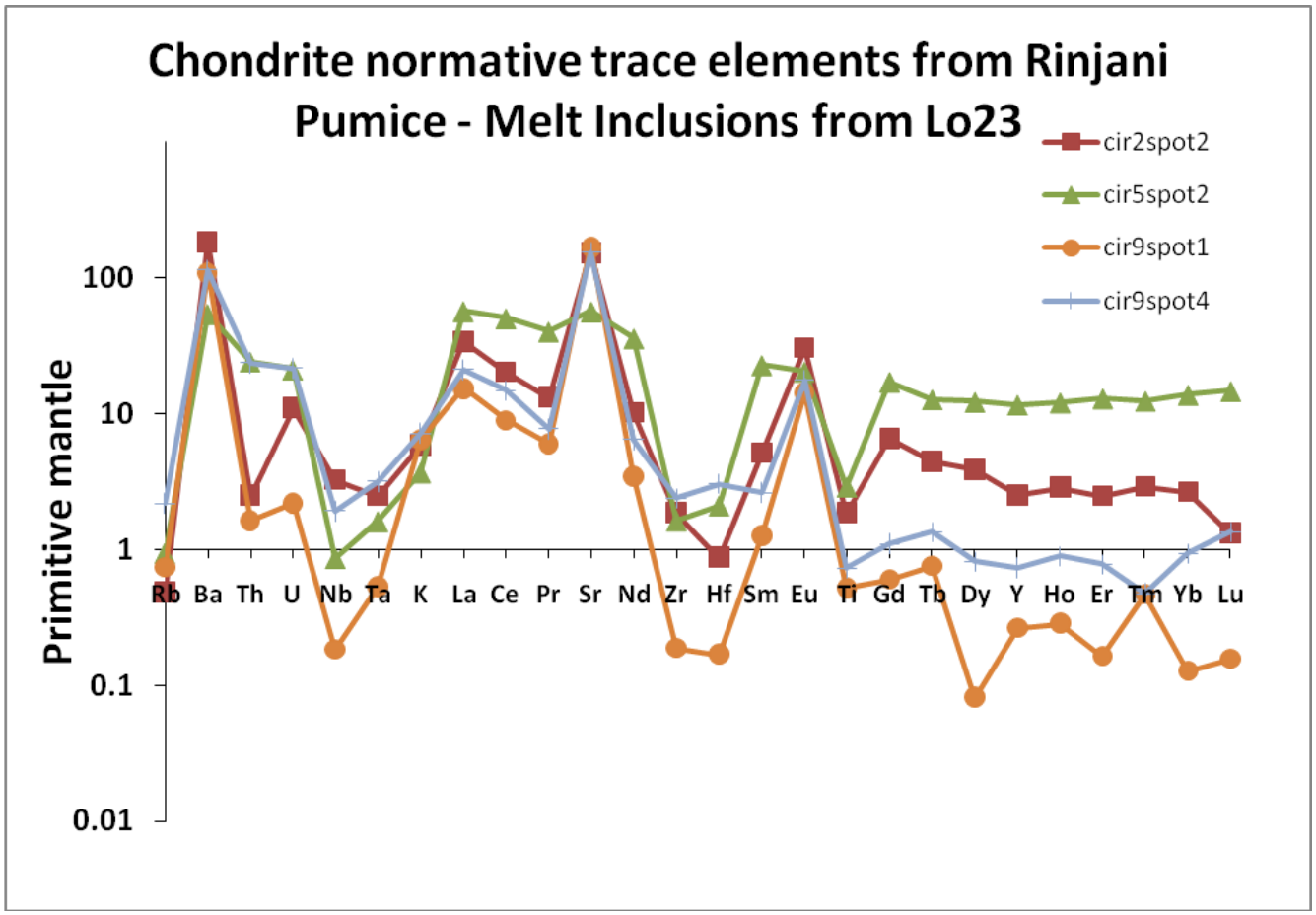
Chondrite normative trace elements from Rinjani Pumice - Melt Inclusions from Lo23
cir2spot2
cir5spot2
cir9spot1
cir9spot4
Primitive mantle
100
10
1
0.1
0.01
Rb Ba Th U Nb Ta K La Ce Pr Sr Nd Zr Hf Sm Eu Ti Gd Tb Dy Y Ho Er Tm Yb Lu

Figure 28.

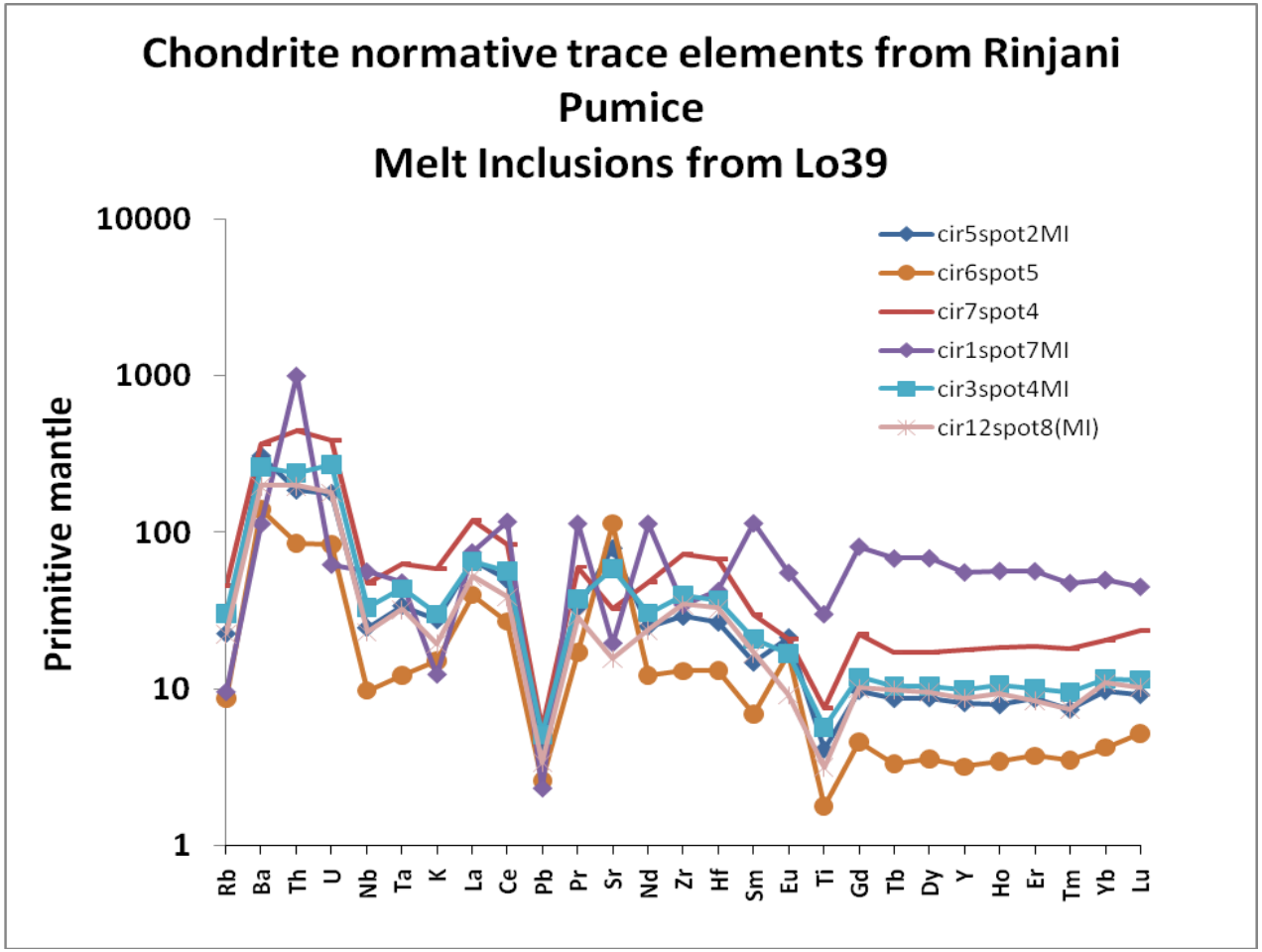
Chondrite normative trace elements from Rinjani Pumice
Melt Inclusions from Lo39
Primitive mantle
10000
1000
100
10
1
cir5spot2MI
cir6spot5
cir7spot4
cir1spot7MI
cir3spot4MI
cir12spot8(MI)
Rb
Ba
Th
U
Nb
Ta
K
La
Ce
Pb
Pr
Sr
Nd
Zr
Hf
Sm
Eu
Ti
Gd
Tb
Dy
Y
Ho
Er
Tm
Yb
Lu

Figure 29.

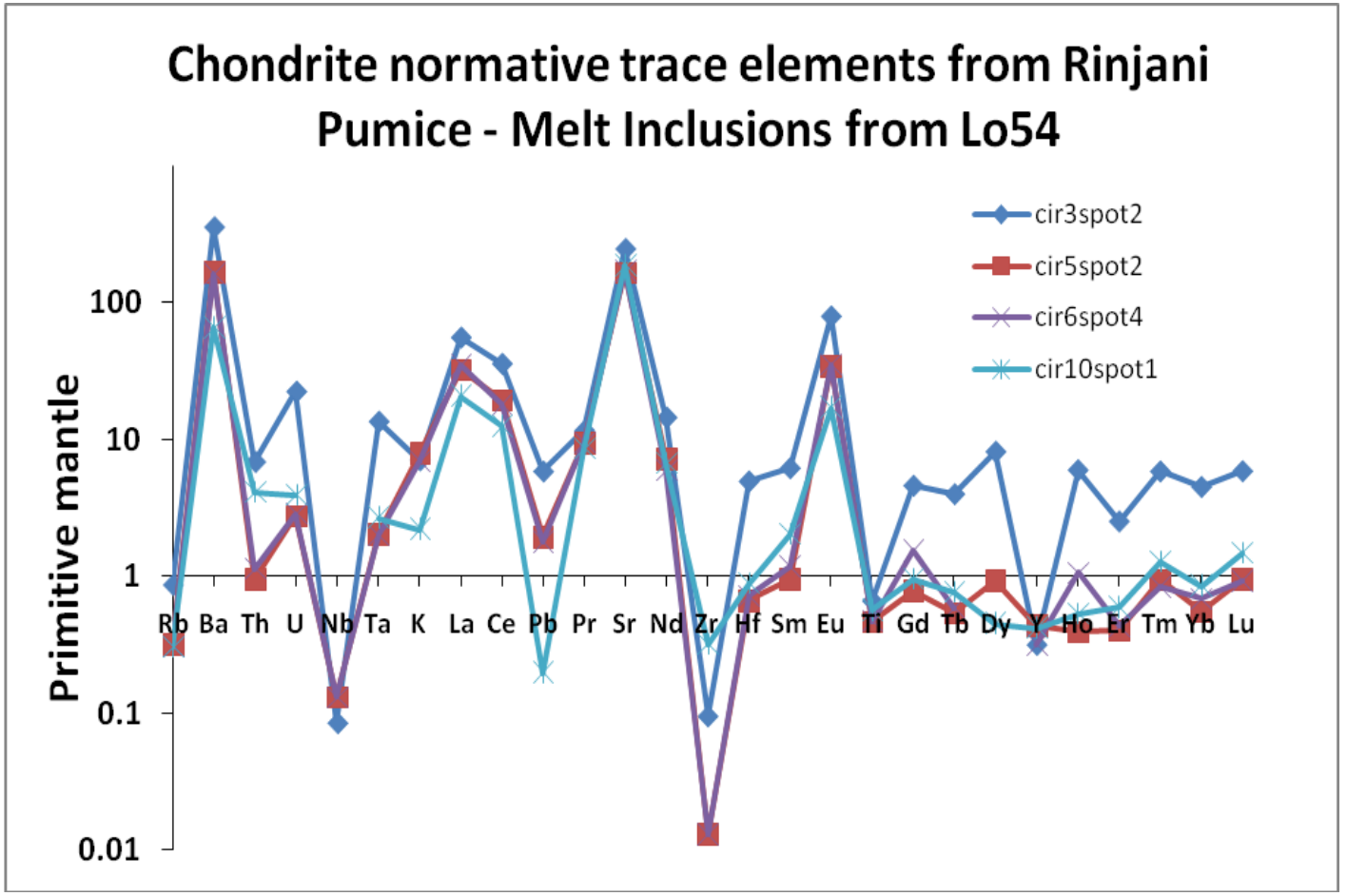
Chondrite normative trace elements from Rinjani Pumice - Melt Inclusions from Lo54
Primitive mantle
100
10
1
0.1
0.01
Rb Ba Th U Nb Ta K La Ce Pb Pr Sr Nd Zr Hf Sm Eu Ti Gd Tb Dy Y Ho Er Tm Yb Lu
cir3spot2
cir5spot2
cir6spot4
cir10spot1

Figure 30.

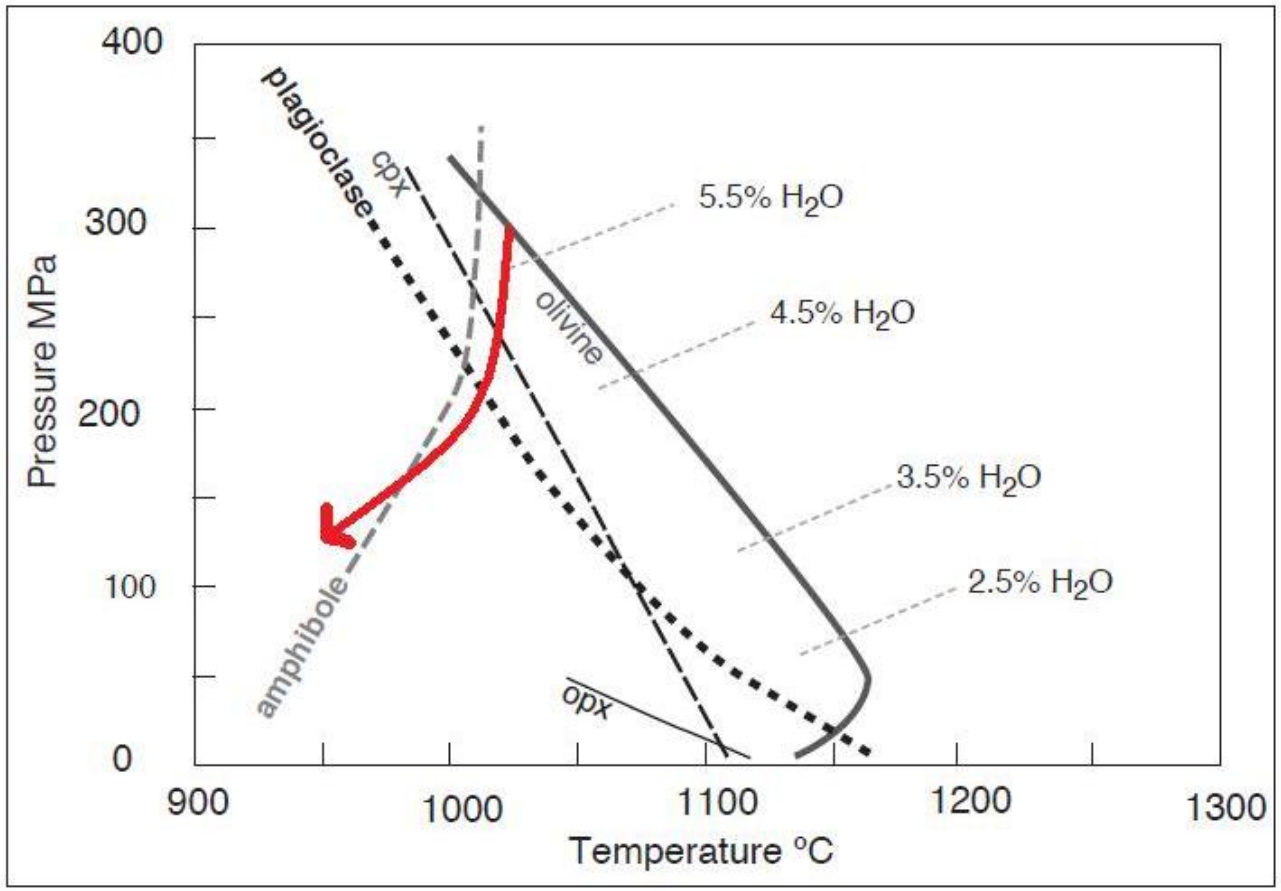

- Shows evolutionary trend of fractionating magma beneath Riniani

Figure 31.

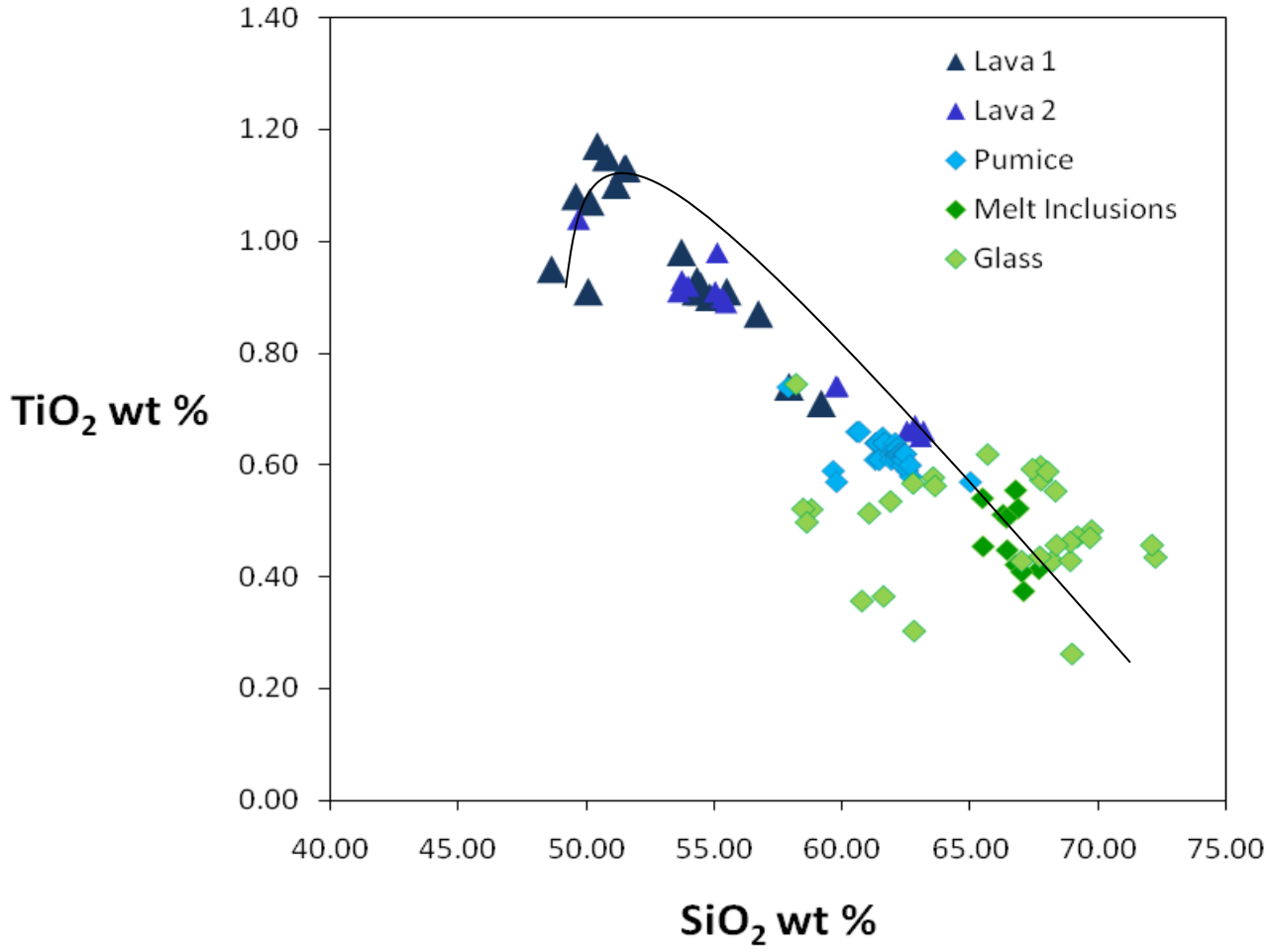
1.40
1.20
1.00
0.80
0.60
0.40
0.20
0.00
TiO2 wt %
40.00
45.00
50.00
55.00
60.00
65.00
70.00
75.00
SiO2 wt %
Lava 1
Lava 2
Pumice
Melt Inclusions
Glass

Figure 32.

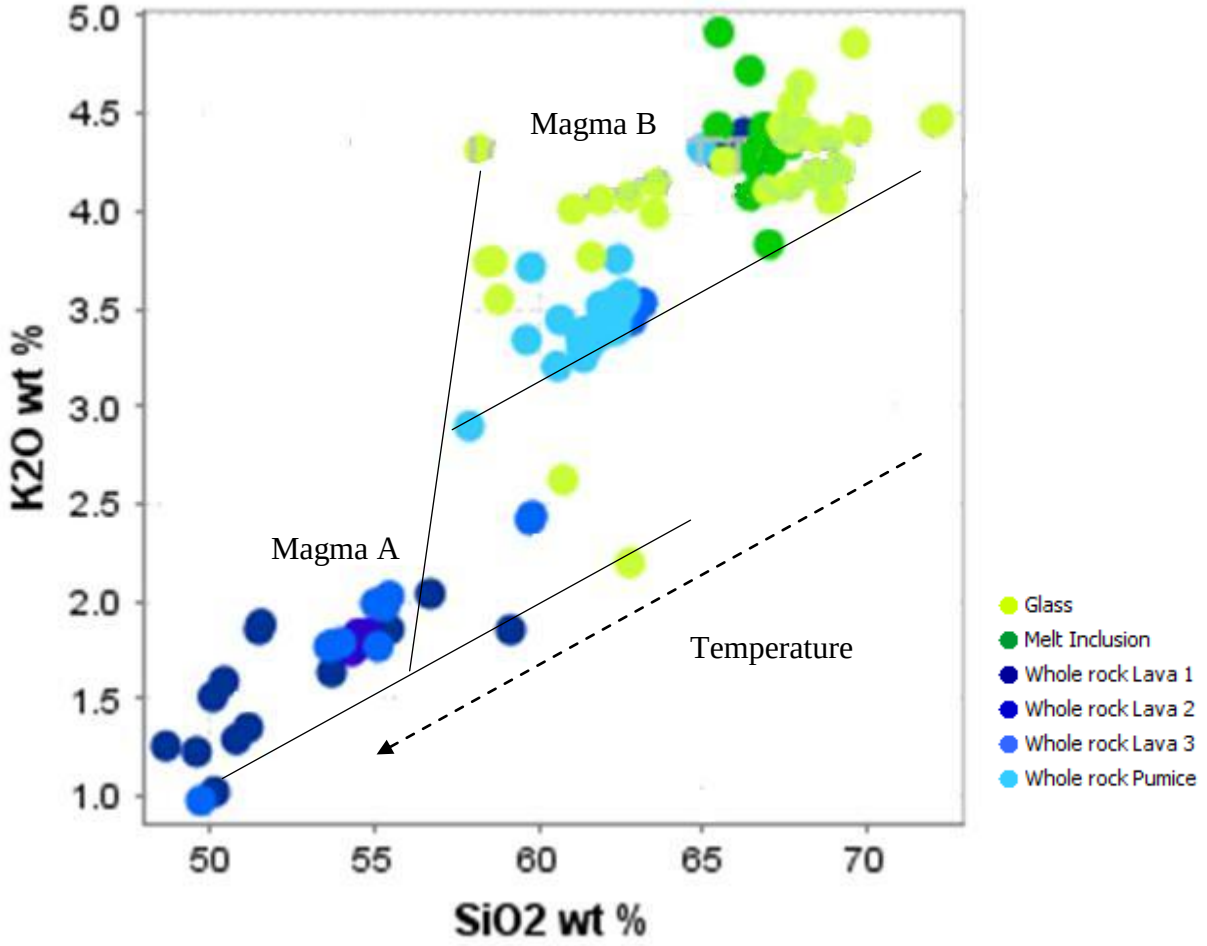
5.0
4.5
4.0
3.5
3.0
2.5
2.0
1.5
1.0
K2O wt %
50
55
60
65
70
SiO2 wt %
Magma B
Magma A
Temperature
Glass
Melt Inclusion
Whole rock Lava 1
Whole rock Lava 2
Whole rock Lava 3
Whole rock Pumice

Figure 33.

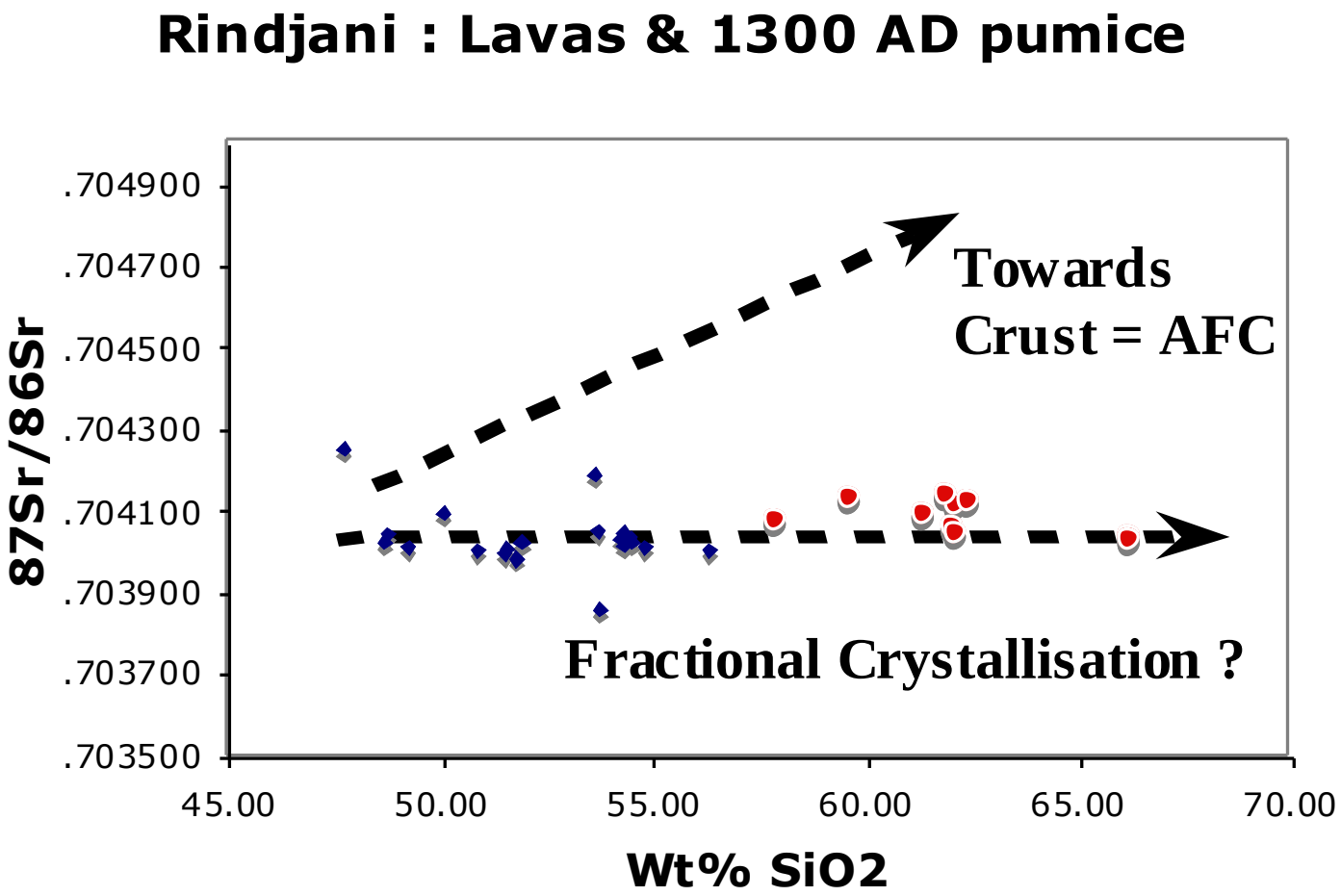

Foden (2001-2002)

Figure 34.

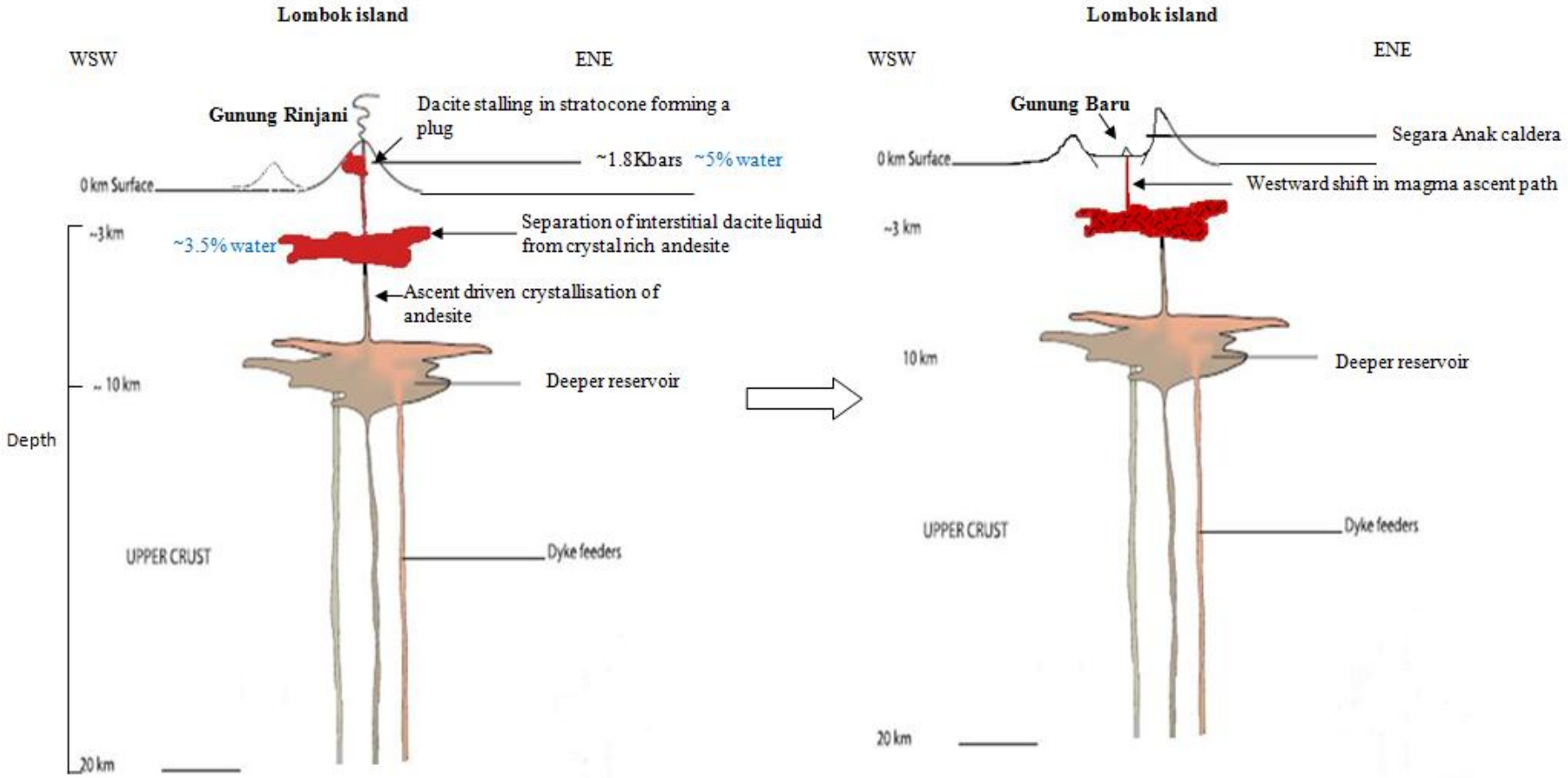
Lombok island
WSW
ENE
Gunung Rinjani
Dacite stalling in stratocone forming a plug
~1.8Kbars
~5% water
0 km Surface
~3 km
~3.5% water
Separation of interstitial dacite liquid from crystal rich andesite
Ascent driven crystallisation of andesite
~ 10 km
Deeper reservoir
Depth
UPPER CRUST
Dyke feeders
20 km
Lombok island
WSW
ENE
Gunung Baru
Segara Anak caldera
0 km Surface
Westward shift in magma ascent path
~3 km
10 km
Deeper reservoir
UPPER CRUST
Dyke feeders
20 km

Figure 35.

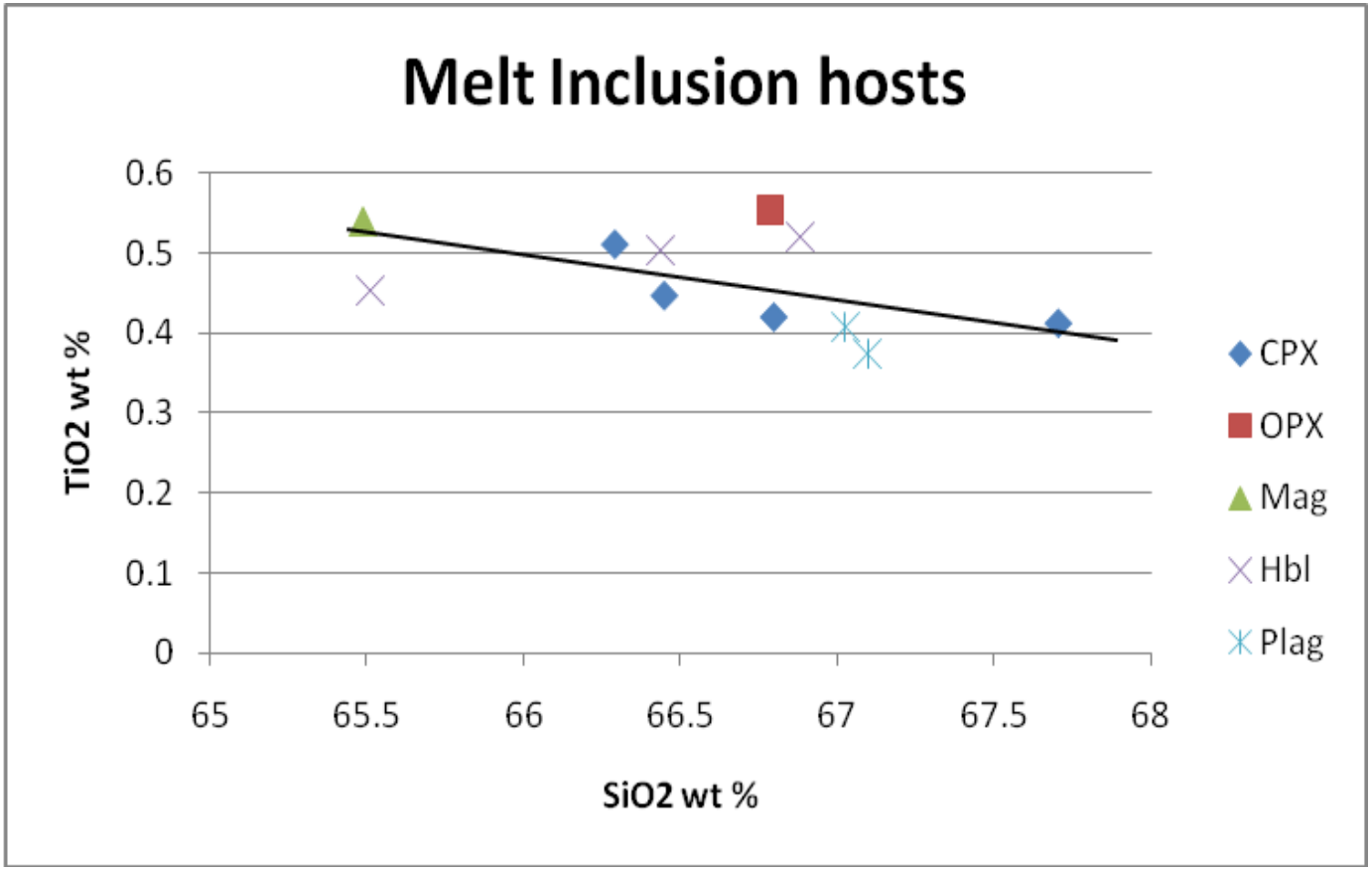
Melt Inclusion hosts
TiO2 wt %
0.6
0.5
0.4
0.3
0.2
0.1
0
65
65.5
66
66.5
67
67.5
68
SiO2 wt %
CPX
OPX
Mag
Hbl
Plag

Figure 36.

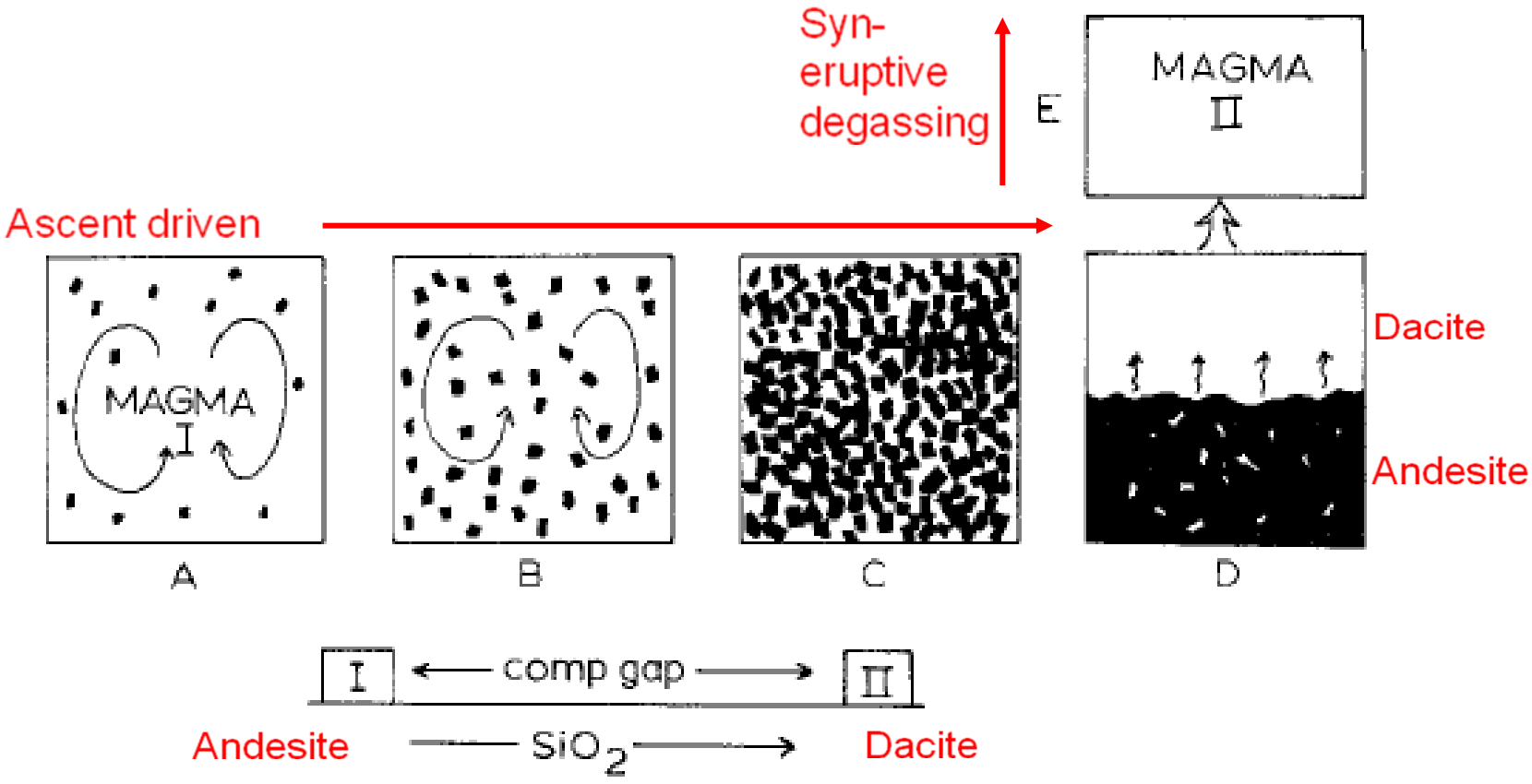

Adapted from Brophy (1991)

TABLES

Mineral Name	Abundance	Grain Size	Grain Shape	Relationships	Optical properties
Plagioclase	~14%	Coarse	Mostly Euhedral and Prismatic	Almost always observed in proximity with hornblende. Large phenocrysts almost always aggregated with large vesicles. Sometimes phenocrysts are slightly subhedral due to fragmentation. Often has melt inclusions in the core, less in the rims.	Twinning 95% of phenocrysts, oscillatory zoning in approximately 35% of phenocrysts and is broad (i.e. few changes in magma composition). Some phenocrysts show only one or two distinct oscillatory zones.
Hornblende	~8%	Coarse to Med	Mostly Euhedral and Tabular	Almost always observed in proximity to plagioclase. Melt inclusions and apatite inclusions often present in cores and rims. Was also seen to host small plagioclase inclusions.	Second order birefringence, seen being replaced by pyroxene in some cases. Around 5% of hornblende phenocrysts have oxidised rims. Appears stable and euhedral in most cases.
Magnetite	~4%	Fine	Mostly Euhedral and Equant	Found to occur in direct contact with all other mineral species. Is also present in minor traces in the glass groundmass.	Opaque
Orthopyroxene	~3%	Med to Fine	Mostly Euhedral and Equant to Bladed	Found commonly in direct contact with magnetite (grows around and next to it) and less commonly with clinopyroxene.	Second order Birefringence.
Clinopyroxene	~1%	Med to Fine	Mostly Euhedral and Equant to Bladed	Also found in direct contact with magnetite (grows around and next to it) and less commonly with orthopyroxene.	Higher Birefringence than orthopyroxene.
Biotite and Olivine	<1%	Fine		Not seen in thin section or grain mount observations but found in small traces with the Electron Microprobe.	
Glass Groundmass	~70%	Fine	Homogenous	Vesicle rich, groundmass abundance estimate includes vesicles which equate to approximately 80% of the groundmass.	Phenocrysts of all species are often in the proximity of large vesicles. Flow alignment (trachytic texture) directed around phenocrysts can be observed in some areas of samples within the groundmass.

Table 1. Typical characteristics observed of minerals within the Rinjani Pumice from thin section and grain mount petrography. The descriptions given for each mineral are based on observations from many thin section and grain mount petrographic observations, and are given to represent the Rinjani Pumice as a whole.

	XRF Whole rock	Microprobe analysis									
		Plag	Hbl	OPX	CPX	Mag	Apatite	Olivine	Biotite	Glass	Melt Inclusions
SiO2	61.84	53.95	42.88	52.84	51.18	0.16	1.91	37.96	37.43	65.10	66.59
TiO2	0.62	0.05	3.18	0.32	0.64	9.39	0.19	0.02	5.85	0.61	0.47
Al2O3	16.90	28.30	10.30	1.00	2.74	2.93	0.49	0.02	14.45	15.73	16.20
Cr2O3		0.01	0.01	0.00		0.04				0.00	
FeO	2.47	0.60	12.28	18.65	9.03	78.77	1.01	26.79	13.97	2.56	2.60
MnO	0.13	0.02	0.39	1.18	0.45	0.78	0.17	1.19	0.17	0.12	0.14
MgO	1.41	0.14	14.05	25.04	15.00	2.48	0.84	36.11	15.84	0.80	0.57
ZnO		0.03	0.04	0.06	0.04	0.11	0.08	0.08	0.01	0.02	0.04
CaO	3.58	11.41	11.12	1.30	21.13	0.04	51.48	0.08	0.03	2.28	1.92
Na2O	4.31	4.82	2.36	0.03	0.37	0.02	0.18	0.01	0.90	1.76	1.01
K2O	3.46	0.37	0.83	0.01	0.01	0.01	0.07	0.01	8.11	3.96	4.35
NiO		0.01	0.02	0.02	0.01	0.02	0.04	0.05	0.03	0.01	0.02
P2O5	0.22	0.03	0.02	0.01	0.01	0.01	30.33	0.01	0.01	0.08	0.05
SO3	0.03	0.01	0.01	0.00	0.00	0.60	0.03	0.01	0.03	0.01	0.02
Fe2O3	1.97										
Total	96.94	99.75	97.50	100.46	100.64	95.35	86.81	102.34	96.82	93.05	93.97
Total with whole rock Na										95.60	97.27
Assumed water loss	3.06	0.25	2.50			4.65	13.19		3.18	4.40	2.73

Table 2. Summary of major element analysis from previous whole rock (Foden 2001-2002) and Electron Microprobe analysis. The table shows the average oxide weight percent composition for minerals analysed with the electron microprobe. Totals for glass and melt inclusion analysis were added with the whole rock Na_2O wt %, where the measured Na_2O wt % were subtracted. Assumed water loss was calculated by taking the total sum of the elemental oxide weight % analysis from 100. This could only be done for totals less than 100.

Method	Texture	T (°C)	P (Kbar)	Water sat wt %
CPX LIQUID	avg core	1016.15		3.7
	avg rim	1011.15		3.7
CPX-OPX	avg core	915.92	3.03	5.6
	avg rim	901.70	2.99	5.6
HORN-PLAG	avg rim	914.74		5.3
SILICA	avg glass	993.22	2.54	4.0
	avg melt incs	986.08	1.80	4.0
OLIVINE-LIQUID	cores	989.70		4.0
PLAG LIQUID (Putrika 2005)		986.08	3.11	4.2
PLAG LIQUID (Putrika 2008)		675.24		10.0
Depth of saturation			1.82	
Average		**966.0811**	**2.58975**	**5.0**

Table 3. Summary of results from geothermometry, geobarometry and hygrometry methods.

Height of lake ASL (m)	2001.00
Avg depth of lake (m)	103.00
Bottom of lake/caldera ASL (m)	1898.00
Height of far most left caldera wall (m)	2200.00
Circumference caldera (Google Earth) (km)	22.96
Diameter of caldera km (d=C/π)	7.31
Radius of caldera (km)	3.66
Area of caldera (πr^2)	41.97
π	3.14
Volume of caldera (πr^2h)	**39.56 Km^3**

Table 4. Caldera volume calculations based on the depth of Segara Anak from the western most wall of the caldera. Depth estimates were taken from the western edge of the caldera as the eastern edge is host to the original stratocone vent prior to caldera formation which sits 3726m ASL and using this height as the roof of the caldera would return false data. Average depth of lake values were taken from Bernard et al. (2009). The circumference of the lake was calculated using visual tools in Google Earth (2009).

APPENDICES

Appendix A

Extended methods

Preparing the samples

Sample analysis with the Laser ICP-MS and Electron Microprobe, is time consuming and expensive. To reduce the time and cost of sample analysis, sample preparation was crucial to the efficiency of the project.

As thin section petrography revealed the pumice samples to be extremely crystal poor and vesicle rich, the chance of finding a phenocryst dense area to analyse with the Laser ICP-MS or Electron Microprobe was low. Therefore to create a phenocryst dense sample for easier and more resourceful analysis, grain mounts were prepared.

Pumice samples from the collection acquired by John Foden of the University of Adelaide from Lombok island were chosen at random. Some of these samples were the samples the thin sections were taken from. The samples chosen to create grain mounts were Lo23, Lo39 and Lo54. Each sample was crushed with the tungsten-carbide rock crusher at Adelaide University. Before and after each sample was crushed, the crusher was thoroughly cleaned with compressed air and ethanol, and scrubbed with a wire brush to remove any contamination. The samples were collected under the crusher in a paper lined tray and the crushed materials were transferred to a sieve.

Using a 3-compartment sieve, sieving mesh was inserted a two points to separate the crushed materials into three size categories. These were >1.5 mm, <1.5 mm but >75 µm and <0.75 µm. The sieve was put into a paint mixer and shaken intensely for approximately 2 minutes. Once the sieve had separated the sample into the three grain size categories, the resulting sections were bagged separately. The sieve and sieving mesh was then cleaned thoroughly with compressed air and ethanol, in preparation for grain size separation of the next samples. On inspection it was evident more sieving was needed to obtain a sample rich in crystals. The sample sizes with grains <1.5 mm but > 75µm were sieved again to obtain a further two sample sizes which were >.75 mm but <1.5 mm and <.75 mm but >75 µm.

The size interval with grains >0.75 mm but <1.5 mm was found using a dissection microscope to contain the highest amount of phenocrysts and therefore this grain size selection was used to make the all grain mounts. The crystals were still hard to see and pick out from the sample to make grain mounts as large amounts of very fine crushed pumice were still present and coating the phenocrysts. This meant the samples had to be washed. To do this, the crushed samples were each transferred to a beaker. The beaker was filled with distilled water and stirred. Once gravity settled the samples, the water overlying the grains was decanted and the beaker was filled with distilled water again. This was done four times for each sample. Once this was done, each sample was tipped over .75mm sieving mesh and more distilled water was rinsed through the grains. The

samples were then each transferred to paper where they were spread flat to sit on an oven and dry overnight. When the samples were dry, they were again bagged separately.

The selection of crushed materials from each sample was then roughly separated into magnetic and non-magnetic bags. To do this, a magnet was place inside a plastic cover and scanned over the crushed samples. The outside of the cover became accumulated in magnetic minerals (magnetite). The separated magnetic minerals from each crushed sample were placed into a further three sample bags. So from each sample within grain size interval >0.75 mm but <1.5 mm, there are now two sample bags of crystals, one for magnetic and one for non-magnetic minerals.

Using a dissection microscope, grains were separated by eye identification into groups. In turn, sample bags were tipped into a Petri dish and under the microscope, fine tweezers were used to pick grains of the same mineral and place them into vials. As eye identification is not extremely accurate, minerals were mainly separated into vials based on similar colours where black and green minerals, i.e. magnetite and pyroxenes were grouped, and lighter minerals i.e. plagioclase were grouped for each sample.

Two grain mounts were made for each sample, one for the mafic minerals and one for the felsic minerals where the sample numbers were denoted with ‘MGM’ (magnetite grain mount) or ‘PGM’ (Plagioclase grain mount) respectively. This was prepared by first lining glass slides with double sided clear tape. An approximately 2 cm PVC tube was then placed on the tape and a circle drawn on the inside of the tube. The tube was then removed and the slide was placed under the dissection microscope. For a dominantly felsic grain mount, grains were plucked from the handpicked vial for that sample and placed onto the double sided tape on the glass slide. Grains were placed in rows and a few millimetres apart to try and create a phenocryst dense mount. Once the grains were in place, the tube was fitted back to its circle, and fixed to the double sided tape. The slide was marked with sample identification ready for the epoxy resin to be introduced. Resin was then prepared by incorporating a 5:1 ratio of epoxy resin and catalyst respectively, and mixing the blend vigorously for approximately two minutes. The resin was then poured into tube to full it. Once the resin was poured, the slide was placed above an oven for approximately two days for the epoxy resin to set solid. This was repeated for all grain mounts. Once the mounts were set, the double sided tape and glass slide were removed from the tube and un-polished grain mounts were revealed. Sample identification was designated to each grain mount of Lo23PGM, Lo23MGM, Lo39PGM, Lo39MGM, Lo54PGM and Lo54MGM.

As the grains were un-exposed at the surface of the grain mount, the six samples were to each be polished. Problems arose while trying to use the lap cloth for the polishing of the grain mounts due to machine maintenance. Therefore the six grain mounts were sent to Pontifex for polishing to expose the mounts for analysis and also for polishing with the lap-cloth to attain a mirror shine for accurate results.

The samples then needed to be marked and targets numbered to make sample analysis at Adelaide Microscopy more efficient. Samples were each looked at under the Leica MZ16FA Stereomicroscope at Adelaide Microscopy and when a target mineral was found with prospective melt inclusions or glass also, it was circled, numbered, and a photo was taken and also labelled with the same number for visual reference. The photos from each sample were then turned into a PowerPoint presentation. Lines were also drawn between each circle with arrows along them for easy navigation, as when the samples are in the machines for analysis, they are not visible.

The same method of marking and photographing the samples was also used for thin sections Lo18, Lo39, Lo52 and Lo54. Although crystal poor and vesicle rich, some groundmass glass analysis, and associated mineral analysis could be obtained from these sections.

Once the thin sections and grain mounts were marked, they were sent to Adelaide Microscopy to be carbon coated for Electron Microprobe and following Laser ICP-MS analysis.

Major element analysis

To acquire major element data, the Rinjani pumice samples were analysed using the Cameca SX 51 Electron Microprobe at Adelaide Microscopy. The Microprobe runs on a booking schedule so the samples were run in series of batches when booking time was able to be acquired. A spread of elements was selected for the Microprobe to analyse for. These elements were selected based on the major elements typical of an arc volcanic suite. These included Na, Mg, Al, Si, P, S, Cl, K, Ca, Ti, Cr, Mn, Fe, Ni and Zn. All grain mounts and thin sections noted in the sample preparation were analysed using the Electron Microprobe.

Samples were prepared for the microprobe analysis by first mounting them into a sample holder. A plastic overlay with a grid of coordinates displayed was used to map where target areas to be analysed were located. Once coordinates were noted, the samples to be analysed were ready for introduction into the Microprobe. Using the Cameca SX51software on a computer linked to the Microprobe, the ‘airlock’ button was clicked. The gun valve on the probe was then turned to position 1. After a short while, the SX program indicated that the ‘airlock backup was complete’. Any previous sample cell in the Microprobe was then retrieved by inserting the extraction rod into the chamber and pulling it out with the existing sample cell attached. In the SX software, the button ‘pump’ was clicked and when the airlock was vented, the airlock door could be opened to retrieve the sample cell. To introduce the new sample cell, the cell was pushing against the exchange rod until it was secure. The airlock door was closed and in the SX software the ‘airlock’ button was clicked. When ‘airlock backup complete’ is displayed by the SX software, the exchange rod was inserted into the machine as far as possible. The shuttle then remained in the chamber and the rod was retrieved. In the SX

software, the icon ‘pump’ was again selected and then instruction was given to ‘turn gun valve to position 2 and this task was carried out. Eventually the SX software displayed ‘Gun valve ready’ and ‘Vacuum ready’ to indicate that the Microprobe is ready to turn the beam on. This process was completed for each sample exchange. In the SX window, the icon ‘Beam on 15kV’ was selected. The machine was then ready to navigate and analyse spots. Navigation was by thumb wheel movement where one wheel controlled the movement of the beam in the X direction, one in the Y direction, and one in the Z direction (depth).

Once the sample was ready for analysis, a position program file was created to run a series of spots in the absence of a controller. To do this, the thumbwheels were used to navigate to areas, specified by the coordinate map overlay for analysis. Once in an area desired for analysis, the position was saved with identification. Single spots or lines with many spots were saved into the position file to analyse many minerals and specifically target melt inclusions and glasses. Once the position file was completed, it was set to run. As each spot analysis takes approximately 3.5 minutes to run, position files were often left to analyse spots overnight. Once the file was finished running, the output was saved by selecting print from the file menu, and then saving to the ‘Ascii” option where a prompt asked for a specific file name and saving location. All output files were in the form of text files which were later converted to Microsoft Excel files.

Trace element analysis

It is usually standard to analyse samples first with the Electron Microprobe for major elements and secondly with the Laser ICP-MS for trace element data. Time constraints and booking restrictions created problems in synchronising analysis this way. Therefore due to booking availability, samples were first analysed with the Laser ICP-MS for trace elements. The setback with doing this is due to the standard for the Laser ICP-MS. The Laser uses an oxide weight percent of a selected mineral first found in major element data from the Microprobe for that sample. Due to volcanic rocks having a large percentage of silica, major element data in the form of silica oxide weight percents were used as a standard for each sample respectively. For example the Microprobe may give a reading of SiO_2 weight percent for hornblende minerals within the sample Lo39 of 45. This value can then be used for a silica standard for all hornblende minerals within the sample Lo39 for the trace element data analysis on the Laser. Because the Laser ICP-MS was used before the Microprobe had analysed the samples, a standard silica oxide weight percent value of 70 was used for all analysis run on the Laser ICP-MS. This value was only temporary as when the pumice thin sections and grain mounts had been analysed with the Microprobe, the actual silica oxide weight percent values for each sample would be re-entered as standards for the trace elements data.

To analyse the pumice samples with the Laser ICP-MS, a software program named Glitter was used on one of three computers. This program was used in conjunction with New Wave software which is used to view samples in the Laser cell, and also navigate

and operate the Laser Ablation on another computer. This software was also used in conjunction with another program known as ICP MS-TOP Chemistation on a third computer. Before sample analysis, a file with the name of the sample to be analysed had to be made within the shared drive at Adelaide Microscopy under the name of the operator. This file was then opened with the Glitter program and element concentrations were chosen from the analysis menu on computer 1. A previous method for analysis of volcanic rocks had been made by Foden (2001-2002) and this was used to run the current samples. This method was opened using the Chemistation software on computer 2. The elements this method analysed for were Mg24, Si29, K39, Ca43, Sc45, Ti49, V51, Cr53, Mn55, Fe56, Co59, Ni60, Cu63, Ga69, Rb85, Sr88, Y89, Zr90, Nb93, Ba137, La139, Ce140, Pr141, Nd146, Sm147, Eu153, Gd157, Tb159, Dy163, Ho165, Er166, Tm169, Yb172, Lu175, Hf178, Ta181, Pb208, Th232 and U238. The New Wave program on computer 3 was then set at 5Hertz with 40 micron spot sizes and the maximum power of the beam was also set to 75 percent. The best magnification found to ensure an accurate position of laser spot but also show an accurate position within a mineral was 75 percent. On computer 1, the PowerPoint file corresponding to the sample to be analysed was opened as a visual key to identify minerals and target Laser spots. The sample corresponding to the PowerPoint file was then ready to be introduced to the chamber for Laser ablation.

Many steps had to be taken to introduce a sample to the laser cell. First, a mixing chamber connected to the Laser Ablation system was slowly loosened to allow gas to escape from the system. The sample cell was then opened and slowly removed from the ablation chamber. The sample cell was then cleaned with ethanol and the sample to be analysed was placed into the cell, and then back into the ablation chamber carefully. The ‘make-up’ (argon) gas tap was then opened and the make-up gas flow in the Chemistation software was increased to 0.2L/min for approximately two minutes to expel air the system gained while having the ablation chamber open. The make-up gas was then reduced to zero in the Chemistation software, the ablation chamber was closed, the make-up gas tap was closed, and the mixing chamber was slowly re-tightened. This process was to be repeated each time a new sample needed to be analysed.

To run an analysis, first the ‘Method-Run’ protocol was selected from the Chemistation software. A new file name was then entered for each laser spot analysis corresponding to the spot identification within the PowerPoint file for that sample. Then again in the Chemistation software, ‘Run Method’ was clicked. A window on computer 2 showed the time elapsed and when it came to twenty seconds, the ‘Fire’ icon for the laser beam was selected on computer 3 using the New Wave program. This got the laser beam firing but not ablating the sample as the shutter was not open. Once thirty seconds had elapsed, the shutter for the laser beam was opened on the New Wave program and ablation began. Once the beam had been ablating the sample for 45 seconds, the shutter was closed and the beam turned off with the ‘Fire’ icon in the New Wave software.

After each laser ablation spot, the make-up gas tap was opened and the make-up gas flow in the Chemistation software was increased to 0.2L/min to purge and ablated materials out of the chamber. Once 1-2 minutes had passed, the make-up gas flow was decreased back to zero and the make-up gas tap was closed. In the ICP MS-TOP software on computer 2, the new ablated data had to be checked for processing in glitter, this was done by clicking 'update' in the QCDetail icon on the desktop. Once this was done, the icon 'update' was also clicked on computer 1 in the Glitter software. Data was then automatically imported to the *Glitter* software and an elemental analysis could be seen from the ablation. A silica standard for each spot had to be manually entered depending on the major element silica value for that mineral but as discussed above, this was initially impossible as major element data was not yet acquired. Therefore the standard silica value for each spot was 70 weight percent until major element data could be imported at a later stage. The New Wave software was then used to locate a new target spot for laser ablation and the process began again. This process was repeated for each spot on each sample. All grain mounts and thin sections noted in the sample preparation were analysed using the Laser Ablation ICP-MS methods.

Once the samples had been analysed using the Microprobe, the silica oxide weight percent values for each sample was re-entered as standards into the Glitter program and the laser data could then be exported. Each sample file was exported to be saved as a '.csv' file. Which was later converted to an excel file for each sample.

Appendix B

Specific mass numbers detected from ions dissociated by plasma gas using Laser Ablation ICP-MS

Mg24, Si29, K39, Ca43, Sc45, Ti49, V51, Cr53, Mn55, Fe56, Co59, Ni60, Cu63, Ga69, Rb85, Sr88, Y89, Zr90, Nb93, Ba137, La139, Ce140, Pr141, Nd146, Sm147, Eu153, Gd157, Tb159, Dy163, Ho165, Er166, Tm169, Yb172, Lu175, Hf178, Ta181, Pb208, Th232 and U238

Appendix C

Modelling crystallisation with Pele©
2000 bar

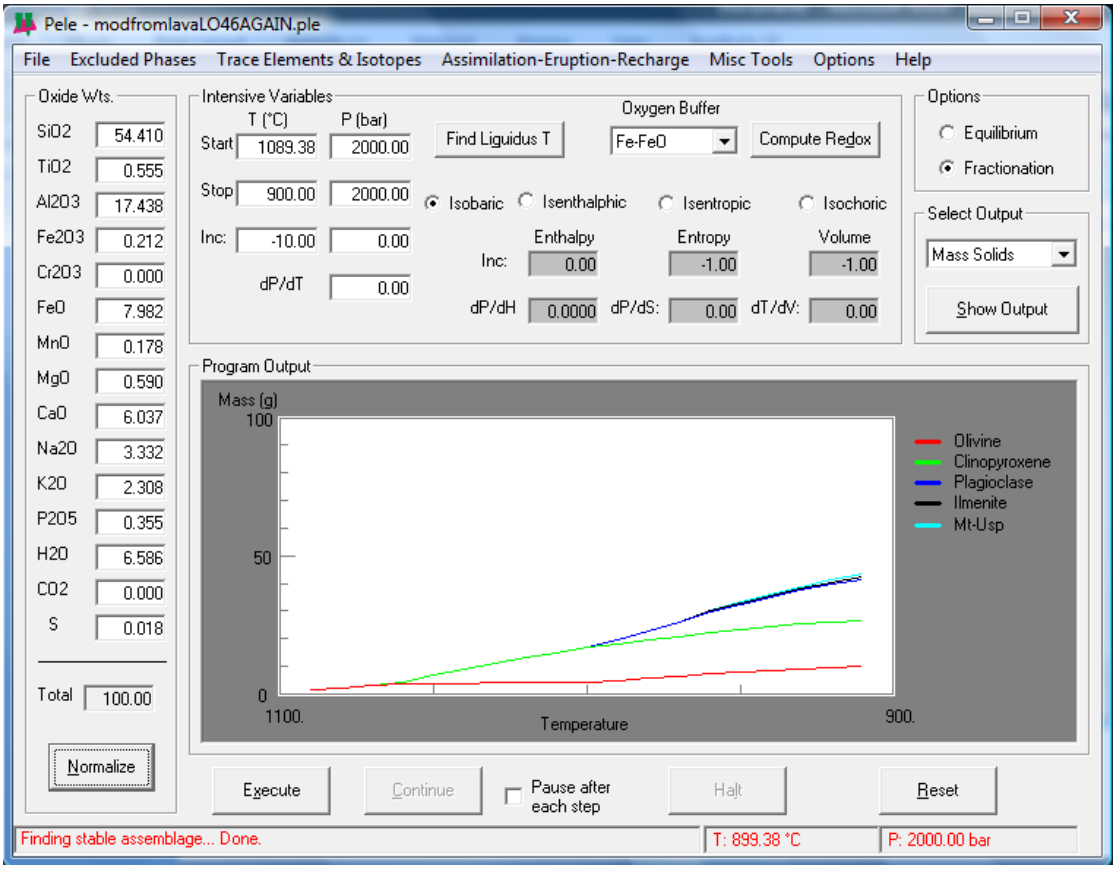

1500 bar

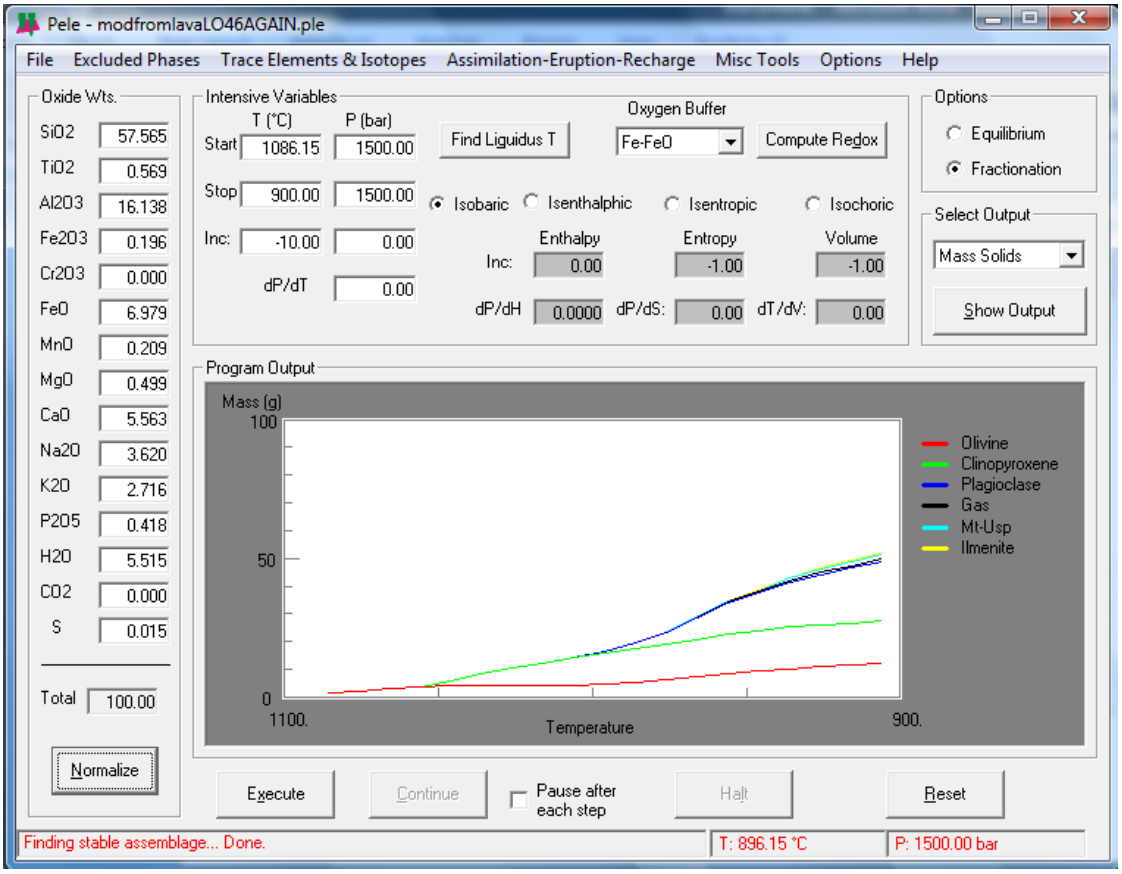
Pele - modfromlavaLO46AGAIN.ple
File
Excluded Phases
Trace Elements & Isotopes
Assimilation-Eruption-Recharge
Misc Tools
Options
Help
Oxide Wts.
SiO2 57.565
TiO2 0.569
Al2O3 16.138
Fe2O3 0.196
Cr2O3 0.000
FeO 6.979
MnO 0.209
MgO 0.499
CaO 5.563
Na2O 3.620
K2O 2.716
P2O5 0.418
H2O 5.515
CO2 0.000
S 0.015
Total 100.00
Normalize
Intensive Variables
T (°C)
P (bar)
Start 1086.15 1500.00
Stop 900.00 1500.00
Inc: -10.00 0.00
dP/dT 0.00
Find Liquidus T
Oxygen Buffer
Fe-FeO
Compute Redox
Isobaric
Isenthalphic
Isentropic
Isochoric
Enthalpy
Entropy
Volume
Inc: 0.00 -1.00 -1.00
dP/dH 0.0000
dP/dS: 0.00
dT/dV: 0.00
Options
Equilibrium
Fractionation
Select Output
Mass Solids
Show Output
Program Output
Mass (g)
100
50
0
1100.
900.
Temperature
Olivine
Clinopyroxene
Plagioclase
Gas
Mt-Usp
Ilmenite
Execute
Continue
Pause after each step
Halt
Reset
Finding stable assemblage... Done.
T: 896.15 °C
P: 1500.00 bar

1000 bar

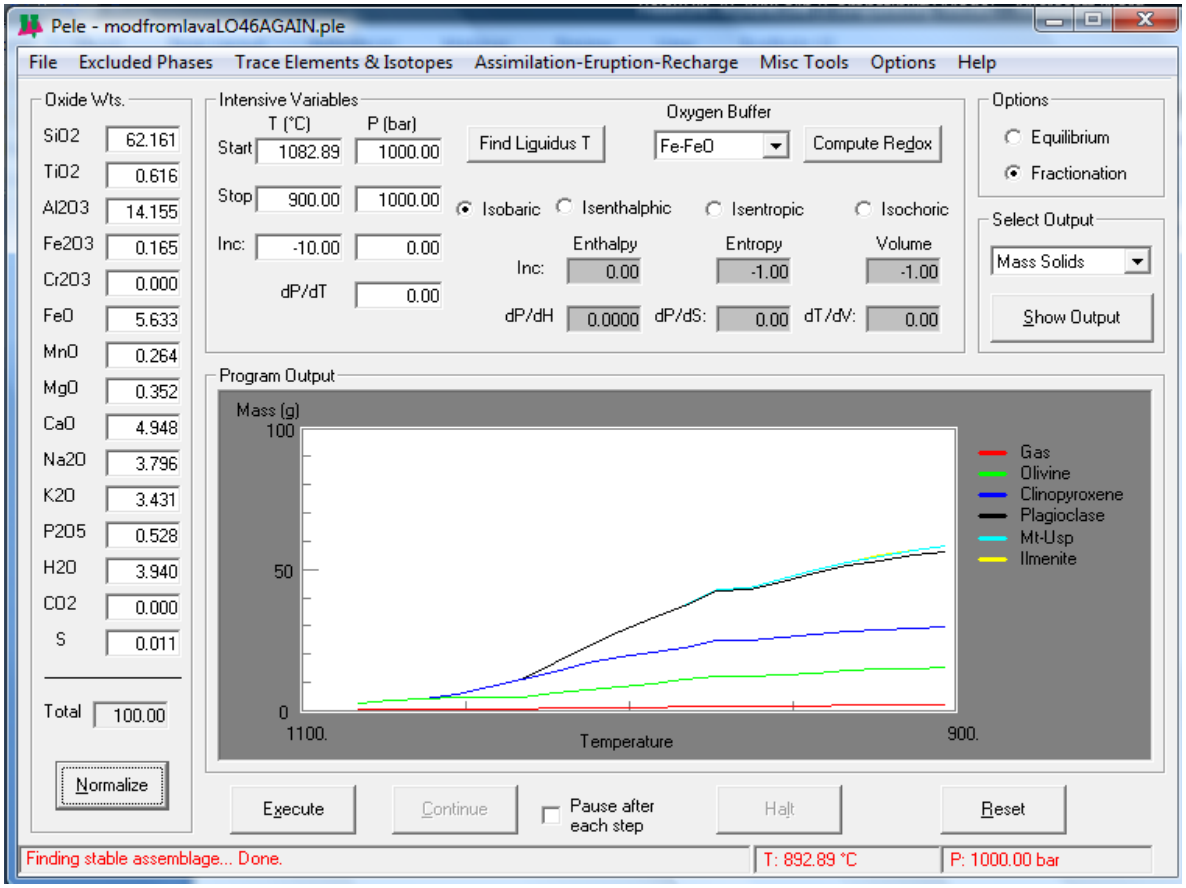
Pele - modfromlavaLO46AGAIN.ple
File
Excluded Phases
Trace Elements & Isotopes
Assimilation-Eruption-Recharge
Misc Tools
Options
Help
Oxide Wts.
SiO2 62.161
TiO2 0.616
Al2O3 14.155
Fe2O3 0.165
Cr2O3 0.000
FeO 5.633
MnO 0.264
MgO 0.352
CaO 4.948
Na2O 3.796
K2O 3.431
P2O5 0.528
H2O 3.940
CO2 0.000
S 0.011
Total 100.00
Normalize
Intensive Variables
T (°C)
P (bar)
Start 1082.89 1000.00
Stop 900.00 1000.00
Inc: -10.00 0.00
dP/dT 0.00
Find Liquidus T
Oxygen Buffer
Fe-FeO
Compute Redox
Isobaric
Isenthalphic
Isentropic
Isochoric
Enthalpy
Entropy
Volume
Inc: 0.00 -1.00 -1.00
dP/dH 0.0000
dP/dS: 0.00
dT/dV: 0.00
Options
Equilibrium
Fractionation
Select Output
Mass Solids
Show Output
Program Output
Mass (g)
100
50
0
1100.
900.
Temperature
Gas
Olivine
Clinopyroxene
Plagioclase
Mt-Usp
Ilmenite
Execute
Continue
Pause after each step
Halt
Reset
Finding stable assemblage... Done.
T: 892.89 °C
P: 1000.00 bar

500 bar

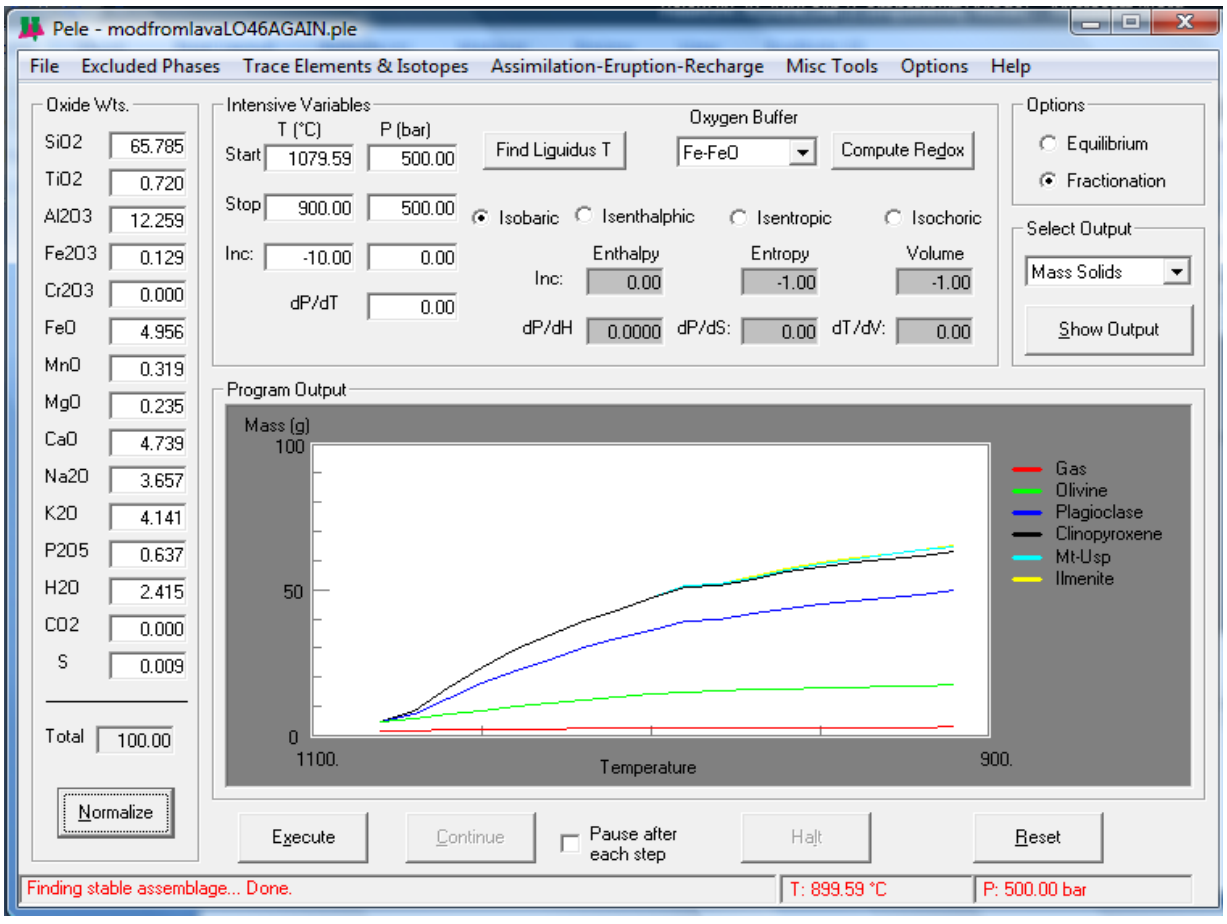
Pele - modfromlavaLO46AGAIN.ple
File
Excluded Phases
Trace Elements & Isotopes
Assimilation-Eruption-Recharge
Misc Tools
Options
Help
Oxide Wts.
SiO2 65.785
TiO2 0.720
Al2O3 12.259
Fe2O3 0.129
Cr2O3 0.000
FeO 4.956
MnO 0.319
MgO 0.235
CaO 4.739
Na2O 3.657
K2O 4.141
P2O5 0.637
H2O 2.415
CO2 0.000
S 0.009
Total 100.00
Normalize
Intensive Variables
T (°C)
P (bar)
Start 1079.59 500.00
Stop 900.00 500.00
Inc: -10.00 0.00
dP/dT 0.00
Find Liquidus T
Oxygen Buffer
Fe-FeO
Compute Redox
Isobaric
Isenthalphic
Isentropic
Isochoric
Enthalpy
Entropy
Volume
Inc: 0.00 -1.00 -1.00
dP/dH 0.0000
dP/dS: 0.00
dT/dV: 0.00
Options
Equilibrium
Fractionation
Select Output
Mass Solids
Show Output
Program Output
Mass (g)
100
50
0
1100.
900.
Temperature
Gas
Olivine
Plagioclase
Clinopyroxene
Mt-Usp
Ilmenite
Execute
Continue
Pause after each step
Halt
Reset
Finding stable assemblage... Done.
T: 899.59 °C
P: 500.00 bar

Starting again at 2000 bar

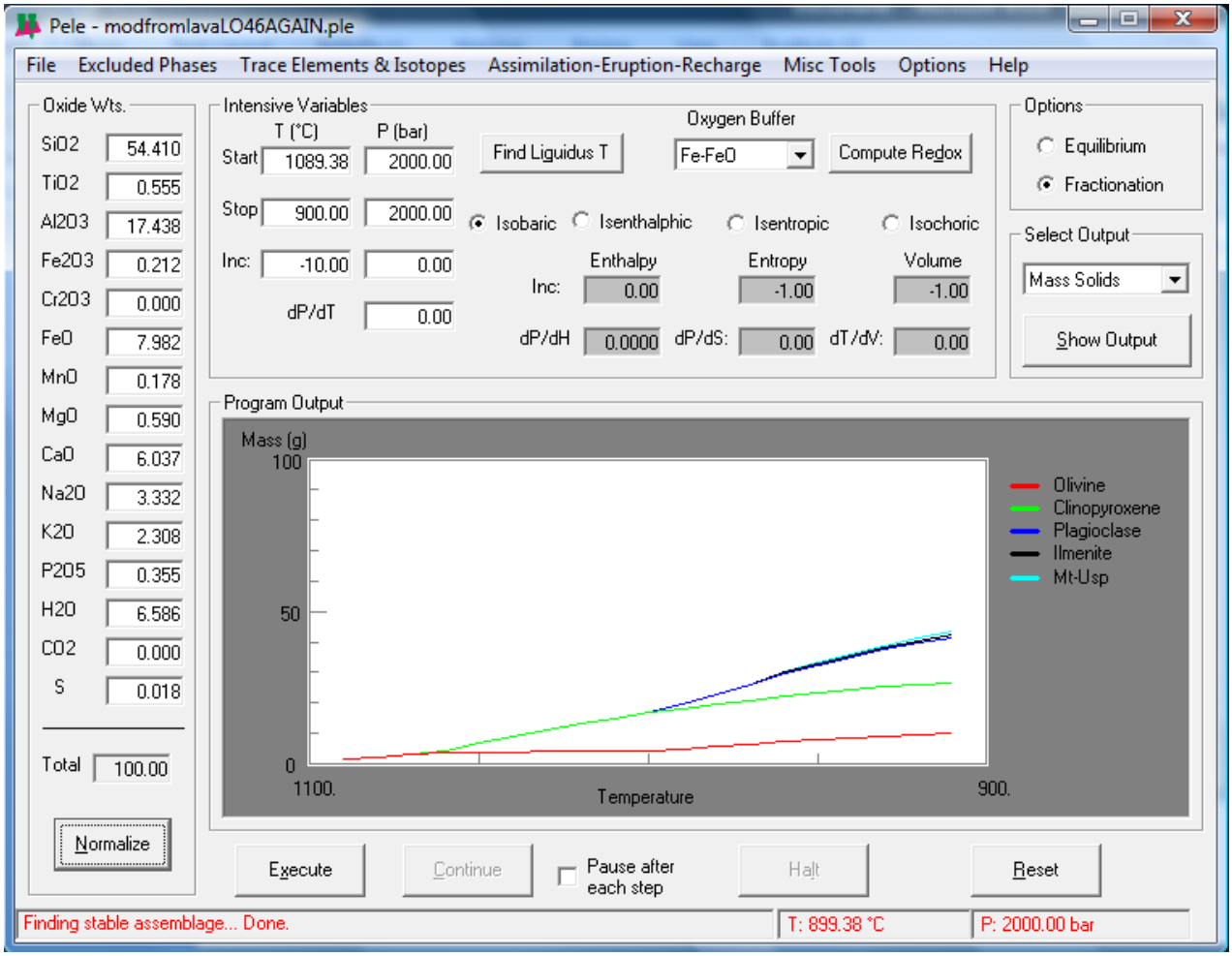

Then the end composition from that at 1500 bar

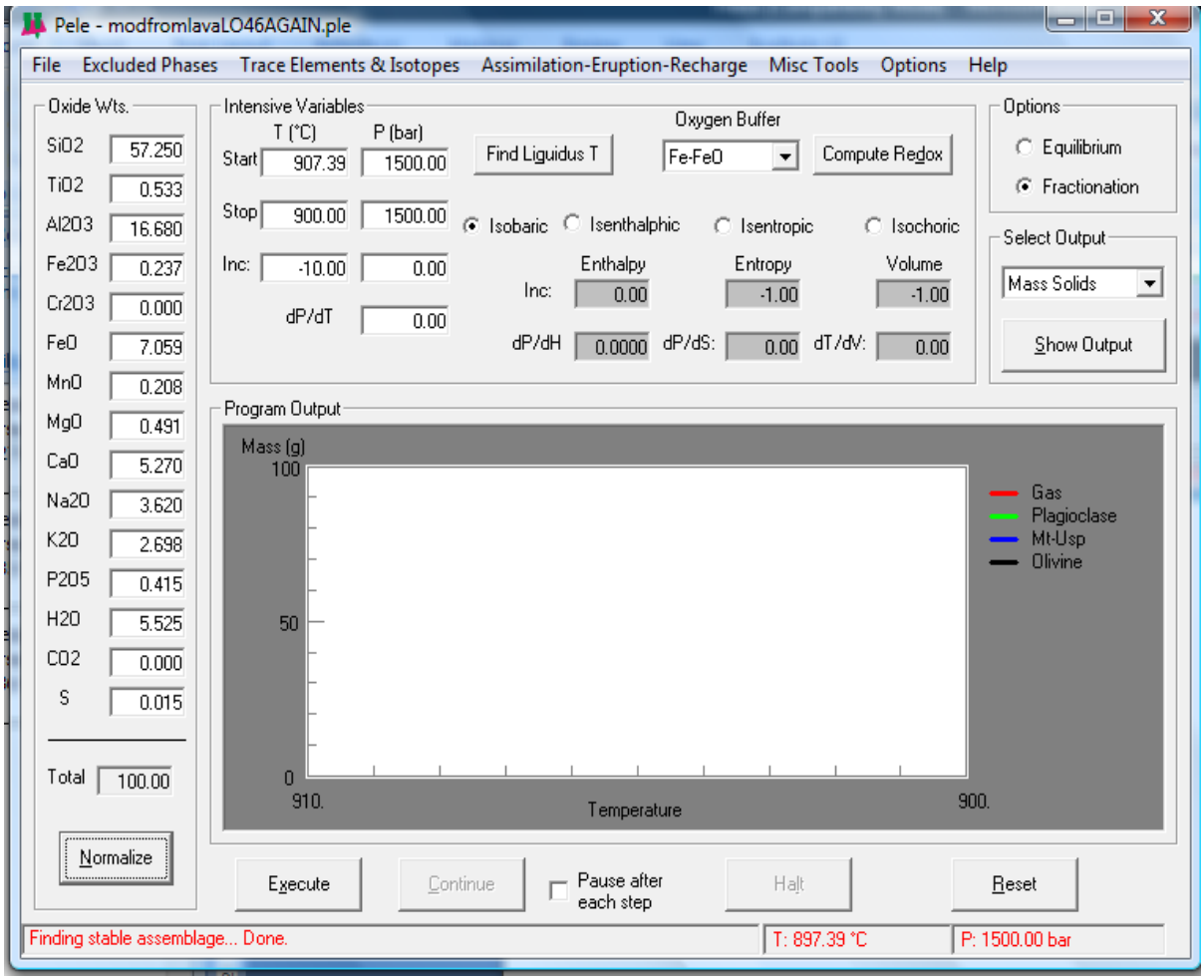

Composition from end of execution at 2000 bars again but starting at 1000 bars

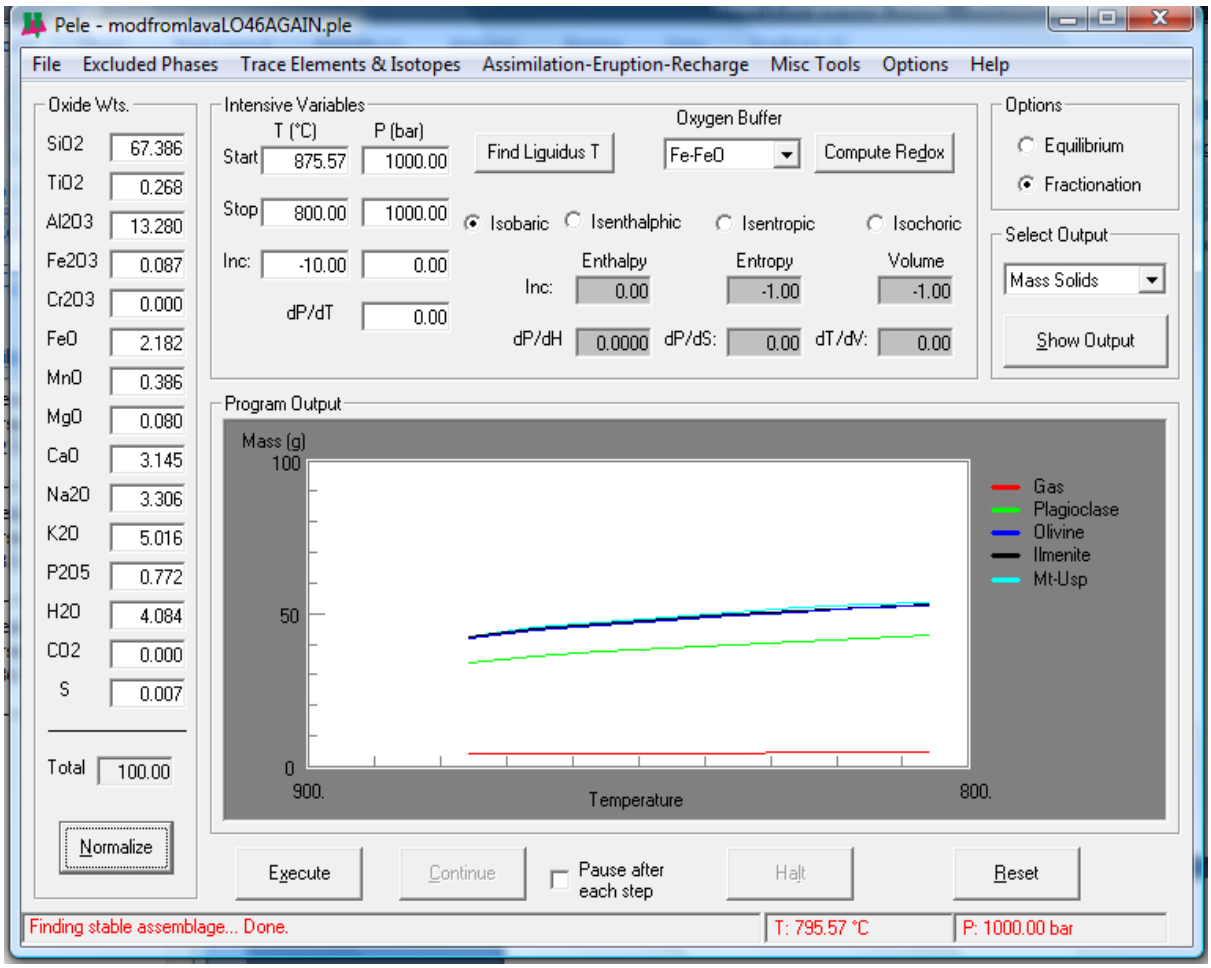

Appendix D

Electron Microprobe Raw Data

Mineral	pl	pl	pl	pl	pl	pl	pl	pl	pl	pl	pl	pl	pl
Analysis No.	LO18 c1 pt1	LO18 c3 pt14	LO18 c3 pt15	LO18 c3 pt16	LO52_C2point2	LO52_C5point1	LO52_C7line1_1	LO52_C10line1_2	LO52_C10line1_3	LO52_C10line1_4	LO52_C12point1MI	LO52_C10line1_5	LO52_C10line1_6
Run ID	tm010509	tm010509	tm010509	tm010509	tm130709	tm130709	tm130709	tm130709	tm130709	tm130709	tm130709	tm130709	tm130709
SiO2	56.2869	56.0061	48.6097	55.8359	55.1729	56.1768	55.3216	56.78	52.63	53.8514	57.6212	52.1397	49.3732
TiO2	0.057	0.0068	0.0461	0.0497	0.0375	0.0238	0.0303	0.0445	0.0243	0.0081	0.1284	0.0531	0.0309
Al2O3	26.7346	25.7433	30.1884	25.8532	27.661	28.2219	27.0734	24.5122	27.1324	26.888	26.1605	27.4694	29.9017
Cr2O3	0.0176	0.0002	0.0253	0.0002									
FeO	0.4852	0.4721	0.4825	0.4758	0.4407	0.434	0.6095	0.5135	0.4517	0.4121	1.4369	0.4351	0.4777
MnO	0.0254	0.0002	0.0002	0.0324	0.011	0.0202	0.0055	0.0239	0.022	0.0002	0.0202	0.0276	0.0002
MgO	0.0572	0.0502	0.031	0.0073	0.0252	0.0478	0.0307	0.051	0.0479	0.0285	0.0342	0.0564	0.0112
ZnO	0.0002	0.0002	0.0002	0.0002									
CaO	10.4209	10.2436	16.1798	10.4062	10.7366	10.8799	9.8651	7.585	10.3905	10.1736	8.6282	10.7219	13.5455
Na2O	5.5453	5.6164	2.6529	5.6013	5.3083	5.4557	5.754	6.8511	5.5584	5.6344	6.4333	5.1884	3.7042
K2O	0.419	0.3876	0.1239	0.3478	0.3213	0.3444	0.3979	0.6234	0.3416	0.3456	0.4191	0.3261	0.1739
NiO	0.00	0.00	0.00	0.00	0.0002	0.0002	0.0166	0.0002	0.0002	0.0002	0.0166	0.0147	0.0221
P					0.0438	0.0097	0.0341	0.0098	0.0003	0.0535	0.0585	0.0486	0.0048
S													
Cl													
F													
Total	100.05	98.53	98.34	98.61	99.76	101.61	99.14	96.99	96.60	97.40	100.96	96.48	97.25

Mineral	pl	pl	pl	pl	pl	pl	pl	pl	pl	pl
Analysis No.	LO52_C10line1_7	LO52_C10line1_8	LO52_C10line1_9	LO52_C10line1_10	LO52_C10line1_11	LO52_C10line1_12	LO52_C10line1_13	LO52_C10line1_14	LO52_C10line1_15	LO52_C10line1_16
Run ID	tm130709	tm130709	tm130709	tm130709	tm130709	tm130709	tm130709	tm130709	tm130709	tm130709
SiO2	48.3513	45.0459	44.7803	45.1428	44.4802	42.7536	43.6589	44.3041	44.4189	44.5653
TiO2	0.0319	0.0314	0.0309	0.0002	0.0203	0.0157	0.0101	0.0228	0.0025	0.0081
Al2O3	30.1218	33.0893	32.7073	32.6296	32.6157	32.4198	33.6501	33.6933	33.3603	33.9008
Cr2O3										
FeO	0.4349	0.4344	0.4148	0.436	0.4131	0.4112	0.3782	0.4755	0.4145	0.4062
MnO	0.022	0.0128	0.0002	0.0092	0.0165	0.011	0.0147	0.0275	0.0002	0.033
MgO	0.0002	0.0142	0.0174	0.0002	0.0206	0.1221	0.0002	0.0021	0.0016	0.0305
ZnO										
CaO	14.2445	16.7827	16.9264	16.9861	17.0526	17.0787	18.072	18.2	17.7191	17.738
Na2O	3.3504	1.7681	1.7436	1.8891	1.7391	1.3908	1.1511	1.2255	1.39	1.3037
K2O	0.1627	0.0622	0.065	0.084	0.0536	0.0798	0.0317	0.0331	0.0453	0.0698
NiO	0.0002	0.0002	0.0002	0.0002	0.0184	0.0018	0.0002	0.0002	0.011	0.0147
P	0.0625	0.0095	0.0334	0.0477	0.0239	0.0476	0.0476	0.0003	0.019	0.0048
S										
Cl										
F										
Total	96.78	97.25	96.72	97.23	96.45	94.33	97.01	97.98	97.38	98.07

Mineral	pl	pl	pl	pl	pl	pl	pl	pl	pl	pl
Analysis No.	LO52_C10line1_17	LO52_C10line1_18	LO52_C10line1_19	LO52_C10line1_20	LO52_C10line1_21	LO52_C10line1_22	LO52_C10line1_23	LO52_C10line2_2	LO52_C10line2_3	LO52_C10line2_4
Run ID	tm130709	tm130709	tm130709	tm130709	tm130709	tm130709	tm130709	tm130709	tm130709	tm130709
SiO2	44.4631	44.2802	43.8959	46.06	49.3673	54.0956	53.3208	57.1962	57.7186	56.9889
TiO2	0.0355	0.036	0.0284	0.0203	0.0466	0.0126	0.0293	0.0248	0.0344	0.0258
Al2O3	32.5599	34.0634	33.769	33.0958	30.4075	27.5258	27.2947	27.0975	26.6578	27.3682
Cr2O3										
FeO	0.466	0.4326	0.393	0.4594	0.461	0.4586	0.4898	0.3874	0.389	0.389
MnO	0.0147	0.0002	0.0349	0.0441	0.0496	0.0129	0.0441	0.0002	0.0037	0.0147
MgO	0.0248	0.0002	0.0142	0.01	0.0288	0.0296	0.0397	0.0151	0.014	0.0032
ZnO										
CaO	16.9126	18.1237	17.8881	16.9137	13.9801	10.2983	10.4715	9.3819	9.1188	9.7386
Na2O	1.7159	1.2147	1.2392	1.832	3.4696	5.4106	5.2072	6.0689	6.1592	5.8719
K2O	0.0799	0.0299	0.0503	0.0723	0.1962	0.3817	0.3259	0.4765	0.5055	0.4114
NiO	0.0002	0.0002	0.0002	0.0002	0.0809	0.0002	0.0002	0.0002	0.0332	0.0332
P	0.1288	0.0761	0.0095	0.0526	0.0289	0.0097	0.0389	0.0586	0.0391	0.0342
S										
Cl										
F										
Total	96.40	98.26	97.32	98.56	98.12	98.24	97.26	100.71	100.67	100.88

Mineral	pl	pl	pl	pl	pl	pl	pl	pl	pl	pl	pl
Analysis No.	LO52_C10line2_5	LO52_C10line2_6	LO52_C10line2_7	LO52_C10line2_8	LO52_C10line3_3	LO52_C10line3_4	LO52_C10line3_5	LO52_C10line3_6	LO52_C10line3_7	LO52_C10line3_9	LO52_C10line3_10
Run ID	tm130709	tm130709	tm130709	tm130709	tm130709	tm130709	tm130709	tm130709	tm130709	tm130709	tm130709
SiO2	56.6331	56.4813	55.7693	55.3066	53.0365	51.1434	43.2089	43.0372	43.8895	45.8292	43.6834
TiO2	0.0329	0.0313	0.0182	0.0425	0.051	0.0147	0.0127	0.0167	0.0304	0.0172	0.0238
Al2O3	27.2225	27.8583	28.2183	28.3856	26.3374	27.1601	33.2359	32.9251	33.5808	32.6512	33.2951
Cr2O3											
FeO	0.394	0.437	0.4105	0.4683	0.4269	0.4186	0.4821	0.4986	0.4079	0.4196	0.3796
MnO	0.0496	0.0129	0.0002	0.0165	0.0349	0.0147	0.0275	0.0239	0.0002	0.0018	0.0422
MgO	0.0366	0.0451	0.0172	0.0172	0.0264	0.0457	0.0158	0.0327	0.0002	0.0317	0.0058
ZnO											
CaO	9.6695	10.0596	10.7106	10.85	9.7803	10.8191	17.6136	17.4536	17.6503	16.5847	17.3796
Na2O	5.9277	5.6408	5.3644	5.3426	5.7955	5.1477	1.2679	1.352	1.3294	1.9202	1.3717
K2O	0.4294	0.3913	0.3317	0.3592	0.372	0.2891	0.0394	0.0453	0.0399	0.0627	0.0449
NiO	0.0002	0.0002	0.0002	0.0002	0.0276	0.0002	0.022	0.0092	0.011	0.0002	0.0349
P	0.0146	0.039	0.0341	0.0681	0.0003	0.0194	0.0003	0.0095	0.0238	0.0048	0.0476
S											
Cl											
F											
Total	100.41	101.00	100.87	100.86	95.89	95.07	95.93	95.40	96.96	97.52	96.31

Mineral	pl	pl	pl	pl	pl	pl	pl	pl	pl	pl	pl
Analysis No.	LO52_C10line3_11	LO52_C10line3_12	LO52_C10line3_13	LO52_C10line3_14	LO52_C11line1_2	LO52_C11line1_3	LO52_C11line1_4	LO52_C11line1_5	LO52_C11line1_6	LO52_C11line1_7	LO52_C11line1_8
Run ID	tm130709	tm130709	tm130709	tm130709	tm130709	tm130709	tm130709	tm130709	tm130709	tm130709	tm130709
SiO2	44.3225	43.5023	50.041	53.4645	56.0667	55.9473	55.9661	54.6509	53.7017	52.521	55.6257
TiO2	0.0025	0.0002	0.0339	0.0111	0.0465	0.0268	0.0556	0.0288	0.0334	0.047	0.0394
Al2O3	34.0288	33.7654	30.2969	27.2636	28.2148	28.0497	28.0325	28.5756	29.6599	25.2685	28.1493
Cr2O3											
FeO	0.388	0.4406	0.4215	0.4812	0.4948	0.4185	0.4535	0.5143	0.4579	0.435	0.3605
MnO	0.0092	0.0477	0.0239	0.0165	0.0294	0.0055	0.011	0.0055	0.0532	0.0367	0.011
MgO	0.0237	0.0002	0.0336	0.0478	0.0354	0.0413	0.0467	0.0284	0.0128	0.073	0.0498
ZnO											
CaO	17.8033	17.987	13.6624	10.4464	10.7468	10.5963	10.4398	11.3301	12.3053	9.5954	10.4425
Na2O	1.3666	1.1994	3.6946	5.4608	5.4988	5.4275	5.4204	5.0865	4.4771	5.0551	5.2801
K2O	0.0458	0.0376	0.1474	0.3373	0.3501	0.3874	0.3554	0.2785	0.2402	0.3723	0.3661
NiO	0.0331	0.0002	0.0331	0.0002	0.0002	0.0239	0.0002	0.0002	0.0258	0.0239	0.0002
P	0.0524	0.019	0.0337	0.0292	0.0003	0.0003	0.0292	0.0003	0.0003	0.0487	0.0146
S											
Cl											
F											
Total	98.08	97.00	98.42	97.56	101.48	100.92	100.81	100.50	100.97	93.48	100.34

Mineral	pl	pl	pl	pl	pl	pl	pl	pl	pl	pl
Analysis No.	LO52_C11line1_9	LO52_C11line1_10	LO52_C11line1_11	LO52_C11line1_12	LO52_C11line1_13	LO52_C11line1_14	LO52_C11line3_2	LO52_C11line3_3	LO52_C11line3_4	LO52_C11line3_5
Run ID	tm130709	tm130709	tm130709	tm130709	tm130709	tm130709	tm130709	tm130709	tm130709	tm130709
SiO2	55.2546	54.5783	54.4932	55.1954	55.7106	55.7088	53.9614	54.3813	53.7046	46.8106
TiO2	0.0091	0.0399	0.0293	0.0061	0.0338	0.0212	0.0455	0.0106	0.0002	0.0643
Al2O3	27.5302	28.9659	28.2765	28.1408	27.5283	27.7149	27.1535	27.2974	26.4954	31.3375
Cr2O3										
FeO	0.3855	0.5455	0.4068	0.5278	0.3871	0.4401	0.4017	0.4581	0.478	0.4772
MnO	0.0002	0.0257	0.0404	0.0257	0.0331	0.0002	0.0002	0.0459	0.0239	0.0002
MgO	0.0317	0.0257	0.0455	0.0365	0.0424	0.0479	0.0456	0.0457	0.0383	0.0002
ZnO										
CaO	10.3537	11.6144	11.1866	10.5346	10.0979	10.4473	10.331	10.0407	9.5606	15.2977
Na2O	5.5547	4.7986	5.1018	5.2996	5.6421	5.6247	5.4747	5.684	5.9608	2.7818
K2O	0.381	0.3063	0.3195	0.3593	0.3591	0.3502	0.3479	0.3967	0.3961	0.1084
NiO	0.0002	0.0626	0.0129	0.0424	0.0258	0.0553	0.0018	0.0002	0.0002	0.0459
P	0.0049	0.0242	0.0003	0.0003	0.0146	0.0003	0.0003	0.0003	0.0438	0.0003
S										
Cl										
F										
Total	99.51	100.99	99.91	100.17	99.87	100.41	97.76	98.36	96.70	96.92

Mineral	pl	pl	pl	pl	pl	pl	pl	pl	pl	pl
Analysis No.	LO52_C11line3_6	LO52_C11line3_7	LO52_C11line3_8	LO52_C11line3_9	LO52_C11line3_10	LO52_C11line3_11	LO52_C11line3_12	LO52_C11line3_13	LO52_C11line3_14	LO52_C12line2_2
Run ID	tm130709	tm130709	tm130709	tm130709	tm130709	tm130709	tm130709	tm130709	tm130709	tm130709
SiO2	45.3231	52.0776	51.6836	51.5187	46.6674	43.9107	47.2389	49.5917	48.4047	55.9717
TiO2	0.039	0.0399	0.0434	0.0525	0.051	0.0238	0.0202	0.0308	0.0136	0.0384
Al2O3	31.1462	27.2481	25.838	26.531	24.3213	31.0124	27.447	26.2948	26.0615	27.7875
Cr2O3										
FeO	0.4293	0.3787	0.435	0.3324	0.395	0.4408	0.385	0.4247	0.4116	0.3985
MnO	0.0404	0.0002	0.0002	0.0331	0.0002	0.0055	0.0514	0.0002	0.0294	0.0092
MgO	0.0217	0.0462	0.0302	0.0403	0.0371	0.0233	0.052	0.0414	0.0388	0.0504
ZnO										
CaO	15.4303	10.5454	9.4184	10.0449	10.1603	15.7195	12.2594	10.5201	10.3996	10.3565
Na2O	2.5838	5.2058	5.9494	5.4557	4.7861	2.3166	4.3833	5.2193	5.3112	5.4507
K2O	0.1033	0.3132	0.3889	0.336	0.3226	0.0822	0.218	0.3173	0.3302	0.3777
NiO	0.0002	0.0166	0.0002	0.0313	0.0002	0.0002	0.0239	0.0002	0.0002	0.0002
P	0.0383	0.0389	0.0003	0.0389	0.0436	0.0239	0.0003	0.0145	0.0339	0.0003
S										
Cl										
F										
Total	95.16	95.91	93.79	94.41	86.78	93.56	92.08	92.46	91.03	100.44

Mineral	pl	pl	pl	pl	pl	pl	pl	pl	pl	pl	pl
Analysis No.	LO52_C12line2_3	LO52_C12line2_4	LO52_C12line2_5	LO52_C12line2_6	LO52_C12line2_7	LO52_C12line2_8	LO52_C12line2_9	LO52_C12line2_10	LO52_C13line1_2	LO52_C13line1_3	LO52_C13line1_4
Run ID	tm130709	tm130709	tm130709	tm130709	tm130709	tm130709	tm130709	tm130709	tm130709	tm130709	tm130709
SiO2	56.2321	52.626	53.8457	54.5755	56.2185	55.8776	56.8596	54.9118	56.6834	56.1551	64.1288
TiO2	0.0091	0.0268	0.0389	0.0626	0.0222	0.0627	0.0328	0.0207	0.0379	0.047	0.1979
Al2O3	27.9889	29.3341	29.6135	27.2837	27.9281	28.1339	27.5955	28.1357	27.2953	27.7606	21.5567
Cr2O3											
FeO	0.3754	0.4497	0.481	0.4893	0.4714	0.44	0.3904	0.3936	0.5029	0.4645	1.4086
MnO	0.0257	0.0002	0.0422	0.0002	0.0002	0.0002	0.0002	0.0002	0.0147	0.0002	0.044
MgO	0.036	0.0384	0.0379	0.0198	0.0279	0.0515	0.05	0.0418	0.0522	0.0553	0.2624
ZnO											
CaO	10.5205	12.5513	12.307	10.671	10.2501	10.6677	10.1356	10.8509	9.9198	10.536	5.6082
Na2O	5.6128	4.3209	4.4958	5.265	5.7153	5.5951	5.9377	5.4002	5.9731	5.4572	4.6464
K2O	0.3441	0.2313	0.2591	0.3242	0.3521	0.3412	0.4017	0.3419	0.4022	0.3683	2.0467
NiO	0.0645	0.0002	0.0497	0.0002	0.0002	0.0002	0.0239	0.0166	0.0002	0.0534	0.0608
P	0.0341	0.0145	0.029	0.0003	0.0146	0.0097	0.0146	0.0003	0.0633	0.0049	0.0246
S											
Cl											
F											
Total	101.24	99.59	101.20	98.69	101.00	101.18	101.44	100.11	100.95	100.90	99.99

Mineral	pl	pl	pl	pl	pl	pl	pl	pl	pl	pl
Analysis No.	LO52_C13line1_5	LO52_C13line1_6	LO52_C13line1_7	LO52_C3_line1_2	LO52_C3_line1_3	LO52_C3_line1_4	LO52_C3_line1_5	LO52_C3_line1_6	LO52_C3_line1_7	LO52_C3_line3MI_2
Run ID	tm130709	tm130709	tm130709	tm130709	tm130709	tm130709	tm130709	tm130709	tm130709	tm130709
SiO2	57.8901	55.3674	55.7397	55.3167	53.9317	53.8774	53.3896	52.543	55.84	56.5014
TiO2	0.0328	0.0444	0.0318	0.046	0.046	0.0212	0.0465	0.0571	0.0263	0.0485
Al2O3	26.6442	28.0879	28.0851	28.5629	29.2865	29.4545	29.2703	30.1603	28.2193	27.3535
Cr2O3										
FeO	0.5176	0.4431	0.4414	0.4827	0.5501	0.5686	0.57	0.4692	0.4315	0.759
MnO	0.022	0.0002	0.0002	0.011	0.0514	0.0002	0.0312	0.022	0.0002	0.0679
MgO	0.0452	0.0316	0.0375	0.0171	0.0529	0.0299	0.0246	0.0389	0.0407	0.0285
ZnO										
CaO	9.1199	10.7583	10.69	10.9321	12.146	12.07	12.1249	13.2594	10.6424	9.98
Na2O	6.2142	5.2753	5.2878	5.276	4.5552	4.5729	4.5099	4.0751	5.4898	5.6552
K2O	0.491	0.3598	0.3069	0.3164	0.2654	0.2344	0.2493	0.2039	0.3655	0.3927
NiO	0.0002	0.0002	0.0184	0.0002	0.0478	0.0294	0.0002	0.0002	0.0002	0.0002
P	0.0003	0.0146	0.0243	0.0097	0.0242	0.0194	0.0003	0.0145	0.0097	0.0003
S										
Cl										
F										
Total	100.98	100.38	100.66	100.97	100.96	100.88	100.22	100.84	101.07	100.79

Mineral	pl	pl	pl	pl	pl	pl	pl	pl	pl
Analysis No.	LO52_C3_line3MI_3	LO52_C3_line3MI_4	LO52_C3_line3MI_5	Lo39MGM_cir6spot3MI	Lo39MGM_cir6spot5MI	Lo54PGM_cir1spot1	Lo54PGM_cir1line1_1	Lo54PGM_cir1line1_2	Lo54PGM_cir1line1_3
Run ID	tm130709	tm130709	tm130709	tm070909	tm070909	tm070909	tm070909	tm070909	tm070909
SiO2	53.7576	54.9242	57.1989	55.4496	54.3976	55.5781	55.8508	56.0668	55.8017
TiO2	0.1176	0.0177	0.0262	0.0034	0.0497	0.0263	0.0518	0.0047	0.0363
Al2O3	27.6491	28.7814	27.486	26.4481	26.8761	28.589	28.6984	28.1361	28.3532
Cr2O3									
FeO	0.7615	0.7468	0.7768	0.6615	0.83	0.3469	0.3469	0.3501	0.4892
MnO	0.0495	0.0002	0.0165	0.0111	0.0002	0.0019	0.0056	0.0037	0.0037
MgO	0.0349	0.037	0.0253	0.0391	0.0305	0.0149	0.0357	0.0374	0.0384
ZnO				0.0447	0.0119	0.0002	0.0002	0.0268	0.0119
CaO	10.7772	11.2268	9.9541	9.5118	10.2663	11.0538	10.8224	10.2927	10.7946
Na2O	5.0629	5.0696	5.6637	5.9273	5.413	5.31	5.2903	5.6934	5.4112
K2O	0.3078	0.2926	0.4042	0.4487	0.4029	0.3343	0.3587	0.398	0.3717
NiO	0.0331	0.0221	0.0313	0.0002	0.0002	0.0336	0.0112	0.0355	0.0486
P	0.0194	0.0485	0.0341	0.0242	0.0193	0.0072	0.029	0.0002	0.0097
S				0.0001	0.0001	0.0001	0.0056	0.0001	0.0042
Cl				0.005	0.0174	0.0002	0.0075	0.0002	0.005
F									
Total	98.57	101.17	101.62	98.57	98.31	101.30	101.51	101.05	101.38

Mineral	pl	pl	pl	pl	pl	pl	pl	pl	pl
Analysis No.	Lo54PGM_cir1line1_4	Lo54PGM_cir1line1_5	Lo54PGM_cir1line1_6	Lo54PGM_cir1line1_7	Lo54PGM_cir1line1_8	Lo54PGM_cir1line1_9	Lo54PGM_cir1line1_10	Lo54PGM_cir5spot1	Lo54PGM_cir5spot2
Run ID	tm070909	tm070909	tm070909	tm070909	tm070909	tm070909	tm070909	tm070909	tm070909
SiO2	53.8637	56.8502	54.8788	55.2482	54.7858	55.6498	51.7169	57.6611	57.4974
TiO2	0.0438	0.2798	0.0061	0.0002	0.0795	0.0114	0.0525	0.031	0.066
Al2O3	29.5225	24.4175	28.4994	28.6246	28.8045	28.2801	30.277	27.1508	26.9662
Cr2O3									
FeO	0.3786	1.6575	0.3973	0.3554	0.4258	0.3337	0.4504	0.3338	0.3791
MnO	0.0002	0.0203	0.0002	0.0002	0.0002	0.0222	0.0002	0.0002	0.0002
MgO	0.026	0.3439	0.0453	0.0213	0.0224	0.0272	0.0191	0.0359	0.0161
ZnO	0.0002	0.0804	0.0002	0.0685	0.003	0.0507	0.0743	0.0805	0.1104
CaO	12.423	7.8747	11.4126	11.4155	11.3403	10.8104	13.513	9.2747	9.2571
Na2O	4.5216	4.1038	5.1125	5.1456	5.094	5.4047	3.7583	6.2765	6.2664
K2O	0.2423	1.4243	0.3249	0.2849	0.3053	0.3747	0.2073	0.4583	0.5136
NiO	0.0002	0.0002	0.0187	0.0075	0.0093	0.0002	0.0002	0.0019	0.0224
P	0.0024	0.0726	0.0217	0.0145	0.0362	0.0338	0.0144	0.0002	0.0002
S	0.0194	0.0111	0.0125	0.0056	0.0069	0.0001	0.0041	0.0001	0.0001
Cl	0.0002	0.2271	0.0002	0.0075	0.0174	0.0249	0.0002	0.01	0.005
F									
Total	101.04	97.31	100.73	101.20	100.93	101.02	100.09	101.31	101.10

Mineral	pl	pl	pl	pl	pl	pl	pl	pl	pl
Analysis No.	Lo54PGM_cir5spot3	Lo54PGM_cir5spot4	Lo54PGM_cir5line1_1	Lo54PGM_cir5line1_3	Lo54PGM_cir5line1_4	Lo54PGM_cir5line1_5	Lo54PGM_cir5line1_6	Lo54PGM_cir5line1_7	Lo54PGM_cir7spot3
Run ID	tm070909	tm070909	tm070909	tm070909	tm070909	tm070909	tm070909	tm070909	tm070909
SiO2	56.6994	55.6793	57.5007	57.4957	58.0148	57.9803	57.4367	56.4596	57.9606
TiO2	0.0316	0.0222	0.0471	0.0518	0.0458	0.0175	0.0002	0.0296	0.0141
Al2O3	27.1456	27.6466	27.5732	27.0433	26.9299	26.7553	27.2705	27.1046	26.2001
Cr2O3									
FeO	0.5818	0.3705	0.3689	0.3154	0.3825	0.3539	0.3741	0.3323	0.3876
MnO	0.0002	0.0111	0.0002	0.0056	0.0002	0.0002	0.0002	0.0093	0.0037
MgO	0.0003	0.0357	0.0284	0.0171	0.0477	0.0445	0.0225	0.0508	0.0215
ZnO	0.0002	0.0002	0.1014	0.0328	0.0002	0.0209	0.0002	0.0002	0.1253
CaO	9.7531	10.2379	9.5591	9.2592	9.2844	9.0207	9.3594	9.6734	8.7521
Na2O	5.8392	5.5583	6.0259	6.2052	6.3771	6.2643	6.0186	5.8169	6.3448
K2O	0.4744	0.4038	0.4402	0.4826	0.4892	0.495	0.461	0.4468	0.5638
NiO	0.0206	0.0002	0.0131	0.0002	0.0002	0.0468	0.0002	0.0002	0.0002
P	0.0002	0.0048	0.0024	0.017	0.0121	0.017	0.0073	0.0002	0.0122
S	0.0028	0.0001	0.0001	0.0001	0.0126	0.0056	0.0028	0.0056	0.0001
Cl	0.02	0.0002	0.0002	0.0075	0.0002	0.0002	0.0025	0.0175	0.0002
F									
Total	100.56	99.97	101.66	100.93	101.60	101.02	100.96	99.94	100.39

Mineral	pl	pl	pl	pl	pl	pl	pl	pl	pl
Analysis No.	Lo54PGM_cir7spot4	Lo54PGM_cir7line1_3	Lo54PGM_cir7line1_4	Lo54PGM_cir7line1_5	Lo54PGM_cir7line1_6	Lo54PGM_cir7line1_7	Lo54PGM_cir7line1_8	Lo54PGM_cir7line1_9	Lo54PGM_cir7line1_10
Run ID	tm070909	tm070909	tm070909	tm070909	tm070909	tm070909	tm070909	tm070909	tm070909
SiO2	54.8641	59.0863	57.3151	57.9339	54.761	57.8384	57.5773	57.344	57.6323
TiO2	0.0404	0.0276	0.0054	0.0067	0.0175	0.0283	0.0269	0.103	0.0216
Al2O3	28.396	26.1925	27.0332	26.919	28.7136	26.7162	27.0741	26.6816	26.9004
Cr2O3									
FeO	0.4056	0.3475	0.3289	0.3978	0.4277	0.3741	0.3862	0.3206	0.3359
MnO	0.0002	0.0167	0.0093	0.0074	0.0002	0.0519	0.0002	0.0538	0.0002
MgO	0.0368	0.0118	0.0171	0.03	0.0559	0.0322	0.0391	0.0118	0.0407
ZnO	0.14	0.0209	0.0835	0.0328	0.0358	0.0328	0.0002	0.0002	0.0299
CaO	11.1007	8.5643	9.3347	9.2423	11.3575	8.8901	9.3551	9.364	9.1985
Na2O	5.2351	6.3379	6.0774	5.9883	4.9607	6.3013	5.9567	6.0593	6.1722
K2O	0.3371	0.5886	0.4584	0.5269	0.3055	0.5437	0.4942	0.5051	0.4223
NiO	0.0002	0.0002	0.0002	0.0002	0.0002	0.0094	0.0356	0.0002	0.0002
P	0.0193	0.0024	0.0243	0.0049	0.0314	0.0002	0.0002	0.0097	0.0073
S	0.0001	0.007	0.0001	0.0014	0.0097	0.0001	0.0154	0.0084	0.0001
Cl	0.0002	0.0002	0.0025	0.0325	0.0249	0.0002	0.005	0.015	0.0125
F									
Total	100.58	101.20	100.69	101.12	100.70	100.82	100.97	100.47	100.77

Mineral	pl	pl	pl	pl	pl	pl	pl	pl	pl	pl
Analysis No.	Lo54PGM_cir10spot1	Lo54PGM_cir10spot2	Lo54PGM_cir10spot3	Lo54PGM_cir6spot2	Lo54PGM_cir6spot3	Lo54PGM_cir6spot4	Lo39PGM_cir1spot1	Lo39PGM_cir1spot2	Lo39PGM_cir1spot3	Lo39PGM_cir2spot1
Run ID	tm070909	tm070909	tm070909	tm070909	tm070909	tm070909	tm070909	tm070909	tm070909	tm070909
SiO2	49.4859	50.8229	50.0047	55.9334	57.2643	57.792	57.8618	58.0012	53.0902	54.7013
TiO2	0.0074	0.0175	0.0546	0.0115	0.0431	0.031	0.0485	0.0559	0.0499	0.0027
Al2O3	31.8085	31.122	32.0792	27.963	27.2289	27.0697	27.1955	26.5451	28.6568	28.1362
Cr2O3										
FeO	0.5861	0.5446	0.5796	0.3473	0.3156	0.3727	0.4212	0.4817	0.5265	0.4646
MnO	0.0204	0.0037	0.0074	0.0185	0.0002	0.0148	0.0002	0.0167	0.0148	0.0315
MgO	0.0592	0.074	0.0765	0.047	0.0005	0.0027	0.0466	0.0493	0.0452	0.0448
ZnO	0.0535	0.0002	0.0002	0.0239	0.0328	0.0507	0.0418	0.0002	0.0002	0.0002
CaO	15.7165	14.4084	15.4521	10.3991	9.7538	9.392	9.2219	8.9665	11.5482	10.8489
Na2O	2.7639	3.3073	2.8918	5.4344	5.8389	6.0037	6.1451	6.2871	4.6221	5.1607
K2O	0.1097	0.1563	0.1301	0.406	0.4069	0.4905	0.4426	0.4597	0.254	0.3234
NiO	0.0541	0.0002	0.0373	0.0002	0.0468	0.0002	0.0019	0.0002	0.0411	0.0243
P	0.0001	0.012	0.0001	0.0097	0.0002	0.0002	0.0121	0.0073	0.0193	0.0387
S	0.0001	0.0001	0.0069	0.0001	0.0001	0.0001	0.0001	0.0001	0.0167	0.0001
Cl	0.0049	0.0025	0.0002	0.03	0.0175	0.025	0.0002	0.0125	0.0423	0.0002
F										
Total	100.67	100.47	101.32	100.62	100.95	101.24	101.44	100.88	98.92	99.78

Mineral	pl	pl	pl	pl	pl	pl	pl	pl	pl	pl
Analysis No.	Lo39PGM_cir2spot2	Lo39PGM_cir2spot3	Lo39PGM_cir2spot4	Lo39PGM_cir3spot1	Lo39PGM_cir3spot3	Lo39PGM_cir3spot4	Lo39PGM_cir3spot5	Lo39PGM_cir5spot1	Lo39PGM_cir5spot2	Lo39PGM_cir5spot3
Run ID	tm070909	tm070909	tm070909	tm070909	tm070909	tm070909	tm070909	tm070909	tm070909	tm070909
SiO2	63.2235	52.4683	43.3983	55.4419	57.3696	57.0807	55.9862	57.4965	57.954	40.9467
TiO2	0.3384	0.0216	2.744	0.0418	0.0673	0.0002	0.033	0.064	0.0317	0.0081
Al2O3	19.8857	30.5039	10.7307	27.7934	26.6374	27.1475	27.914	26.9599	26.5967	20.0732
Cr2O3										
FeO	1.7933	0.4894	12.8317	0.4531	0.453	0.4045	0.428	0.445	0.4903	0.5198
MnO	0.0204	0.0204	0.3935	0.0002	0.0612	0.0056	0.0167	0.0019	0.0002	0.0221
MgO	0.4217	0.0218	14.4235	0.0406	0.0434	0.0583	0.0433	0.0193	0.0477	0.0641
ZnO	0.0597	0.0208	0.0117	0.0002	0.0477	0.0002	0.0477	0.0002	0.0002	0.0383
CaO	5.2102	13.6855	11.4546	10.6588	9.2274	9.7264	10.5892	9.1743	9.1927	21.9886
Na2O	3.3264	3.9751	2.366	5.3797	6.0801	5.9262	5.5999	6.1309	6.1793	4.7136
K2O	1.995	0.1621	0.6703	0.3704	0.4556	0.4384	0.3761	0.47	0.5355	0.2528
NiO	0.0002	0.0002	0.0002	0.0561	0.0037	0.0019	0.0002	0.0002	0.0169	0.0002
P	0.0416	0.0048	0.035	0.0002	0.0002	0.0002	0.0002	0.0097	0.0002	5.2685
S	0.0056	0.0041	0.0027	0.0056	0.0001	0.0001	0.0001	0.0001	0.0126	0.0246
Cl	0.1357	0.0002	0.0702	0.0002	0.015	0.02	0.0374	0.0401	0.0002	0.3644
F										
Total	96.43	101.38	99.12	100.24	100.46	100.81	101.06	100.80	101.06	94.20

Mineral	pl	pl	pl	pl	pl	pl	pl	pl	pl	pl
Analysis No.	Lo39PGM_cir5spot4	Lo39PGM_cir5spot5	Lo39PGM_cir7spot1	Lo39PGM_cir7spot2	Lo39PGM_cir7spot3	Lo39PGM_cir7spot4	Lo39PGM_cir7spot5	Lo39PGM_cir7spot6	Lo39PGM_cir7spot7	Lo39PGM_cir7spot8
Run ID	tm070909	tm070909	tm070909	tm070909	tm070909	tm070909	tm070909	tm070909	tm070909	tm070909
SiO2	56.661	55.8503	57.0104	57.633	64.1069	50.7742	48.6693	55.7296	48.7187	50.6848
TiO2	0.0323	0.0532	0.0532	0.0249	0.8316	0.0695	0.0371	0.068	0.0824	0.0054
Al2O3	27.4541	27.9715	27.4887	27.1741	16.8064	31.3113	33.1199	27.922	32.6665	31.8365
Cr2O3										
FeO	0.3996	0.4529	0.485	0.4196	4.386	0.5348	0.5128	0.5907	0.4726	0.5378
MnO	0.0037	0.0148	0.0002	0.013	0.1714	0.0002	0.0222	0.0223	0.0002	0.0002
MgO	0.0337	0.0438	0.0429	0.0535	1.2525	0.0196	0.0089	0.0428	0.0205	0.0401
ZnO	0.0002	0.0002	0.0835	0.0002	0.0002	0.0002	0.003	0.0209	0.0059	0.0416
CaO	9.9489	10.4798	9.8269	9.052	3.1326	14.3369	16.4902	10.705	16.2043	14.8624
Na2O	5.8538	5.4436	5.9593	6.1328	1.4001	3.3756	2.3269	5.4497	2.3963	3.1308
K2O	0.3767	0.3499	0.4197	0.4512	4.351	0.1351	0.0682	0.2845	0.1226	0.219
NiO	0.0002	0.0449	0.0094	0.0002	0.0392	0.0056	0.0002	0.0112	0.0002	0.0002
P	0.0002	0.0002	0.0388	0.0243	0.3949	0.0024	0.0191	0.0002	0.0048	0.0167
S	0.0001	0.0279	0.0001	0.0154	0.0377	0.0014	0.0001	0.0097	0.0001	0.0001
Cl	0.0575	0.0075	0.0002	0.0002	0.3849	0.0223	0.0247	0.0175	0.0002	0.0049
F										
Total	100.81	100.74	101.42	100.99	97.21	100.58	101.30	100.87	100.70	101.38

Mineral	pl	pl	pl	pl	pl	pl	pl	pl	pl
Analysis No.	Lo54MGM_cir9spot3	Lo23PGM_cir1spot1	Lo23PGM_cir1spot2	Lo23PGM_cir1spot3	Lo23PGM_cir1line1_1	Lo23PGM_cir1line1_2	Lo23PGM_cir1line1_3	Lo23PGM_cir1line1_4	Lo23PGM_cir1line1_5
Run ID	tm070909	tm070909	tm070909	tm070909	tm070909	tm070909	tm070909	tm070909	tm070909
SiO2	59.748	56.0502	58.2089	50.016	55.9193	55.9742	55.8728	57.5175	58.9927
TiO2	0.0905	0.0317	0.0296	0.0453	0.0425	0.0128	0.0499	0.0492	0.0431
Al2O3	23.1546	28.11	26.476	31.4984	28.205	28.11	28.054	26.911	26.2651
Cr2O3									
FeO	2.1785	0.428	0.455	0.4261	0.4716	0.4565	0.448	0.4012	0.507
MnO	0.0852	0.0278	0.0204	0.0037	0.0002	0.0093	0.0111	0.0002	0.0186
MgO	1.3077	0.0321	0.0279	0.0259	0.0523	0.0299	0.0171	0.0536	0.0565
ZnO	0.0388	0.0418	0.0002	0.0002	0.0002	0.006	0.1014	0.0836	0.0687
CaO	5.6014	10.552	8.7078	15.0711	10.8916	10.4785	10.6526	9.2684	8.4948
Na2O	6.8832	5.5524	6.4889	3.017	5.3535	5.4554	5.4605	6.0075	6.6181
K2O	0.9869	0.3687	0.5426	0.1054	0.3797	0.4145	0.3844	0.4999	0.57
NiO	0.0002	0.0075	0.045	0.0002	0.0037	0.0094	0.0002	0.0002	0.03
P	0.0244	0.0002	0.0002	0.0001	0.0002	0.0291	0.0002	0.0146	0.0002
S	0.007	0.0084	0.0001	0.0001	0.0001	0.0001	0.0014	0.0042	0.0042
Cl	0.0025	0.0275	0.0002	0.0002	0.01	0.0002	0.0002	0.0125	0.0002
F									
Total	100.11	101.23	101.00	100.21	101.33	100.99	101.05	100.82	101.67

Mineral	pl	pl	pl	pl	pl	pl	pl	pl
Analysis No.	Lo23PGM_cir1line1_6	Lo23PGM_cir1line1_7	Lo23PGM_cir1line1_8	Lo23PGM_cir1line1_9	Lo23PGM_cir1line1_10	Lo23PGM_cir1line1_11	Lo23PGM_cir1line1_12	Lo23PGM_cir1line1_13
Run ID	tm070909	tm070909	tm070909	tm070909	tm070909	tm070909	tm070909	tm070909
SiO2	49.3407	49.9988	49.6676	49.7286	55.3921	51.2749	52.5474	54.381
TiO2	0.0257	0.0128	0.0196	0.0014	0.0681	0.0344	0.0189	0.0694
Al2O3	32.3012	31.9707	31.9212	32.2476	28.4027	31.1962	30.1704	28.896
Cr2O3								
FeO	0.4526	0.4709	0.4811	0.4794	0.502	0.4443	0.4999	0.4662
MnO	0.0002	0.0389	0.0037	0.0002	0.0002	0.0002	0.0093	0.0037
MgO	0.0105	0.0396	0.019	0.0002	0.039	0.0535	0.0477	0.0491
ZnO	0.0002	0.1219	0.0149	0.0446	0.0002	0.0327	0.0002	0.0715
CaO	15.8689	15.4271	15.4983	15.6266	10.9115	14.4869	12.8814	11.9362
Na2O	2.6245	2.9278	2.8004	2.7531	5.3097	3.5815	3.9668	4.9661
K2O	0.1162	0.1302	0.132	0.131	0.3462	0.1638	0.2535	0.2763
NiO	0.0112	0.0002	0.0131	0.0002	0.0002	0.0112	0.0002	0.0467
P	0.0095	0.0478	0.0048	0.0001	0.0266	0.0287	0.0192	0.0289
S	0.0193	0.0001	0.0041	0.0001	0.0139	0.0001	0.0001	0.0139
Cl	0.0002	0.0002	0.0002	0.0002	0.0002	0.0002	0.0002	0.0324
F								
Total	100.78	101.19	100.58	101.01	101.01	101.31	100.42	101.23

Mineral	pl	pl	pl	pl	pl	pl	pl	pl	pl
Analysis No.	Lo23PGM_cir1line1_14	Lo23PGM_cir1line1_15	Lo23PGM_cir1line1_16	Lo23PGM_cir1line1_17	Lo23PGM_cir2spot1	Lo23PGM_cir2spot2	Lo23PGM_cir2spot3	Lo23PGM_cir2spot4	Lo23PGM_cir3spot1
Run ID	tm070909	tm070909	tm070909	tm070909	tm070909	tm070909	tm070909	tm070909	tm070909
SiO2	49.2262	49.9077	49.6162	50.4783	57.9067	57.5508	57.283	57.1423	55.2831
TiO2	0.0432	0.0324	0.0412	0.0453	0.0047	0.0121	0.0465	0.0485	0.0324
Al2O3	32.2696	32.1433	32.258	32.0373	27.0321	26.8928	27.241	27.4389	28.5737
Cr2O3									
FeO	0.4578	0.5228	0.4495	0.4059	0.4502	0.4451	0.4015	0.4383	0.4078
MnO	0.0002	0.0426	0.0148	0.0352	0.0002	0.0002	0.0002	0.0223	0.0002
MgO	0.0179	0.0002	0.0332	0.0227	0.0601	0.0263	0.0348	0.0364	0.0277
ZnO	0.0327	0.0803	0.0002	0.0002	0.0269	0.009	0.0002	0.0687	0.0002
CaO	15.7528	15.0787	15.621	15.2419	9.2087	9.2788	9.5531	9.7354	11.3696
Na2O	2.6811	2.9527	2.7643	3.0988	6.2571	6.2093	6.0571	5.8306	5.1493
K2O	0.1172	0.1339	0.0951	0.147	0.4272	0.4683	0.454	0.3798	0.3616
NiO	0.0002	0.0075	0.0002	0.0355	0.0002	0.0487	0.0019	0.0487	0.0002
P	0.0001	0.0001	0.0119	0.0001	0.0024	0.0073	0.0049	0.0002	0.0242
S	0.0001	0.0001	0.0138	0.0001	0.0001	0.0196	0.0001	0.0001	0.0001
Cl	0.0074	0.0002	0.0321	0.0002	0.0075	0.0002	0.02	0.0002	0.0199
F									
Total	100.60	100.90	100.94	101.55	101.38	100.97	101.09	101.19	101.25

Mineral	pl	pl	pl	pl	pl	pl	pl	pl	pl
Analysis No.	Lo23PGM_cir3spot2	Lo23PGM_cir3spot3	Lo23PGM_cir3line1_1	Lo23PGM_cir3line1_2	Lo23PGM_cir3line1_3	Lo23PGM_cir3line1_4	Lo23PGM_cir3line1_5	Lo23PGM_cir3line1_6	Lo23PGM_cir3line1_7
Run ID	tm070909	tm070909	tm070909	tm070909	tm070909	tm070909	tm070909	tm070909	tm070909
SiO2	54.2086	55.7985	54.1624	56.2824	56.4733	55.0904	54.9634	54.1465	54.5496
TiO2	0.0256	0.0303	0.0452	0.0142	0.1004	0.0297	0.058	0.0223	0.0391
Al2O3	29.0446	27.9464	28.8522	27.726	27.9462	28.6746	28.4865	27.8555	28.9425
Cr2O3									
FeO	0.4362	0.4601	0.4328	0.4803	0.4366	0.4265	0.3828	0.4566	0.4835
MnO	0.0002	0.0002	0.0019	0.0002	0.0204	0.0204	0.0002	0.013	0.0002
MgO	0.0463	0.0294	0.0538	0.0402	0.046	0.0544	0.0171	0.0379	0.0299
ZnO	0.0358	0.0269	0.0745	0.0328	0.0328	0.0298	0.0716	0.0686	0.0002
CaO	12.0238	10.5882	11.9826	10.3235	10.3641	11.3329	11.2594	11.1512	11.8362
Na2O	4.7122	5.5418	4.7852	5.6431	5.7087	5.0237	5.0945	4.8815	4.9755
K2O	0.2838	0.3614	0.294	0.3793	0.3746	0.3263	0.3627	0.3626	0.3045
NiO	0.0002	0.0002	0.0002	0.0206	0.0002	0.0002	0.0002	0.0002	0.0019
P	0.0001	0.0024	0.0001	0.0002	0.0194	0.0002	0.0193	0.0002	0.0097
S	0.0001	0.0001	0.0001	0.0028	0.0126	0.0001	0.007	0.0264	0.0014
Cl	0.0002	0.0002	0.0002	0.0002	0.0002	0.0002	0.0449	0.0125	0.01
F									
Total	100.82	100.79	100.69	100.95	101.54	101.01	100.76	99.03	101.18

Mineral	pl	pl	pl	pl	pl	pl	pl	pl	pl
Analysis No.	Lo23PGM_cir3line1_8	Lo23PGM_cir3line1_9	Lo23PGM_cir3line1_10	Lo23PGM_cir3line1_11	Lo23PGM_cir3line1_12	Lo23PGM_cir3line1_13	Lo23PGM_cir3line1_14	Lo23PGM_cir3line1_15	Lo23PGM_cir3line1_16
Run ID	tm070909	tm070909	tm070909	tm070909	tm070909	tm070909	tm070909	tm070909	tm070909
SiO2	54.8571	54.472	55.9868	54.482	55.488	55.3337	54.0314	55.4449	55.9313
TiO2	0.0148	0.0418	0.033	0.0081	0.0459	0.0728	0.0283	0.0512	0.0142
Al2O3	28.5848	28.7602	28.1883	28.9225	28.2794	28.5785	29.1137	28.5346	28.7417
Cr2O3									
FeO	0.4599	0.4213	0.4635	0.4365	0.3846	0.4347	0.4367	0.4903	0.3996
MnO	0.0002	0.0002	0.0557	0.0408	0.0204	0.0002	0.0204	0.0002	0.0464
MgO	0.0272	0.0363	0.0401	0.0261	0.0304	0.0438	0.0224	0.0374	0.0208
ZnO	0.0597	0.0775	0.0002	0.003	0.0002	0.0179	0.0002	0.0002	0.0866
CaO	11.3058	11.6213	10.7955	11.8159	11.0056	11.0586	11.8538	11.0514	11.2227
Na2O	4.8581	5.1383	5.3826	4.8581	5.2769	5.1108	4.8323	5.2554	5.1297
K2O	0.3328	0.3186	0.3687	0.312	0.3732	0.3508	0.3046	0.3414	0.3453
NiO	0.0412	0.0002	0.0002	0.0002	0.0002	0.0842	0.0002	0.015	0.0693
P	0.0121	0.0266	0.0024	0.0001	0.0097	0.0193	0.0097	0.0048	0.0048
S	0.0111	0.0001	0.0001	0.0056	0.0001	0.0195	0.0056	0.0001	0.0056
Cl	0.0002	0.0548	0.0075	0.0249	0.0324	0.0499	0.0025	0.0075	0.0125
F									
Total	100.56	100.96	101.32	100.93	100.94	101.16	100.66	101.23	102.03

Mineral	hbl	hbl	hbl	hbl	hbl	hbl	hbl	hbl	hbl	hbl	hbl	hbl	hbl	hbl	hbl
Analysis No.	LO18 c1 pt6	LO18 c1 pt7	LO18 c1 pt8	LO52_	LO52_1	LO52_line1_1	LO52_line1_2	LO52_line1_3	LO52_line1_4	LO52_line1_5	LO52_line1_6	LO52_line1_7	LO52_line1_8	LO52_line1_9	LO52_C2line2_1
Run ID	tm010509	tm010509	tm010509	tm130709	tm130709	tm130709	tm130709	tm130709	tm130709	tm130709	tm130709	tm130709	tm130709	tm130709	tm130709
SiO2	43.5147	43.6412	43.1594	42.8703	41.7488	53.3401	42.9148	42.6196	42.9022	42.4017	42.1249	42.451	42.941	42.4802	40.1453
TiO2	3.3707	3.0131	2.6108	3.2136	3.1214	2.0811	3.0154	3.1705	3.1813	3.0298	3.1514	3.2541	3.0559	3.0881	2.9659
Al2O3	10.0306	10.7038	11.1313	10.0889	10.9746	12.2806	10.0477	9.9022	10.1984	10.2989	10.8667	10.0546	10.2746	10.2735	9.4048
Cr2O3	0.0218	0.0048	0.0169												
FeO	12.1889	11.9928	13.2251	11.975	12.5759	8.5505	12.2398	12.2879	11.9915	12.0903	12.4401	12.091	12.2366	11.9718	11.7748
MnO	0.471	0.4262	0.3584	0.342	0.3741	0.2756	0.3942	0.482	0.4357	0.403	0.4333	0.3978	0.4156	0.3635	0.349
MgO	13.9685	14.3506	13.8309	13.8439	13.9474	8.9633	14.1417	13.7151	14.0055	13.9597	14.028	13.7779	14.0305	13.8358	12.6454
ZnO	0.0884	0.0002	0.0002												
CaO	11.5924	11.4509	11.3438	11.3078	11.2538	7.981	10.9967	11.2075	11.0507	11.0298	11.2104	11.2038	11.2076	11.234	11.0011
Na2O	2.3054	2.3613	2.4965	2.3242	2.4287	2.5571	2.4303	2.4321	2.3759	2.4155	2.4932	2.4795	2.4564	2.3355	2.2394
K2O	0.832	0.7464	0.6508	0.8623	0.7261	1.9566	0.8498	0.8205	0.803	0.7173	0.7144	0.8758	0.8234	0.8202	0.7843
NiO				0.0002	0.0182	0.0256	0.0055	0.0002	0.0002	0.0109	0.0364	0.0002	0.0182	0.0002	0.0327
P				0.0003	0.0234	0.0908	0.0282	0.0421	0.0003	0.075	0.0937	0.0047	0.0234	0.0003	0.0328
S															
Cl															
F															
Total	98.38	98.69	98.82	96.83	97.19	98.10	97.06	96.68	96.94	96.43	97.59	96.59	97.48	96.40	91.38

Mineral	hbl	hbl	hbl	hbl	hbl	hbl	hbl	hbl	hbl	hbl	hbl	hbl
Analysis No.	LO52_C2line2_2	LO52_C2line2_4	LO52_C2line2_6	LO52_C2line2_7	LO52_C2line2_9	LO52_C2line3_2	LO52_C2line3_3	LO52_C2line3_4	LO52_C2line3_5	LO52_C2line3_6	LO52_C2line3_7	LO52_C2line3_8
Run ID	tm130709	tm130709	tm130709	tm130709	tm130709	tm130709	tm130709	tm130709	tm130709	tm130709	tm130709	tm130709
SiO2	43.062	42.5033	41.7179	41.4641	41.2409	43.0655	42.2124	42.5624	42.552	42.3869	42.4571	42.9746
TiO2	3.1154	2.97	3.2576	2.9801	2.9991	3.0078	3.0699	3.2478	2.9006	3.137	2.9278	3.2842
Al2O3	9.9518	10.1959	10.0762	9.5586	9.6815	9.895	9.8744	10.3558	10.6776	11.2401	10.9848	10.2905
Cr2O3												
FeO	12.0573	11.8888	11.9172	11.7701	11.6207	11.8046	12.2376	12.4214	12.4565	12.6941	12.5924	12.3616
MnO	0.4751	0.3079	0.3562	0.3545	0.3744	0.4105	0.3741	0.3886	0.3795	0.3757	0.4099	0.3778
MgO	14.0013	13.6942	13.6052	13.7435	13.7518	13.7834	13.8111	13.8966	13.8432	13.829	13.7649	14.1853
ZnO												
CaO	11.0933	11.2553	10.9057	11.0059	11.2686	11.1059	11.2479	11.4132	11.1767	11.1833	11.1364	11.22
Na2O	2.402	2.4393	2.4686	2.4132	2.4009	2.3218	2.2732	2.4114	2.4619	2.5891	2.4646	2.3093
K2O	0.8357	0.7871	0.8316	0.8084	0.8685	0.815	0.8255	0.8794	0.7143	0.6476	0.7398	0.8698
NiO	0.0002	0.02	0.0036	0.0055	0.0055	0.0002	0.0002	0.0182	0.0002	0.0073	0.0418	0.0002
P	0.0563	0.0375	0.0003	0.0047	0.0047	0.0281	0.0749	0.0515	0.0141	0.0094	0.0656	0.1124
S												
Cl												
F												
Total	97.05	96.10	95.14	94.11	94.22	96.24	96.00	97.65	97.18	98.10	97.59	97.99

Mineral	hbl	hbl	hbl	hbl	hbl	hbl	hbl	hbl	hbl	hbl	hbl	hbl
Analysis No.	LO52_C2line3_9	LO52_C5line1_2	LO52_C5line1_3	LO52_C5line1_4	LO52_C5line1_5	LO52_C5line1_6	LO52_C5line2_3	LO52_C5line2_4	LO52_C5line2_5	LO52_C5line2_7	LO52_C5line2_8	LO52_C5line2_9
Run ID	tm130709	tm130709	tm130709	tm130709	tm130709	tm130709	tm130709	tm130709	tm130709	tm130709	tm130709	tm130709
SiO2	43.8973	41.6623	42.4216	41.3566	42.6097	42.3788	43.4535	43.2896	43.8048	43.1738	43.6113	42.8036
TiO2	3.0372	2.8563	2.9081	2.8768	3.1034	3.121	3.1394	3.2418	3.3528	3.4279	3.3206	3.4321
Al2O3	10.1989	10.395	10.3891	10.1723	10.5543	10.3965	10.6117	10.5299	10.4469	10.3514	10.2221	10.1491
Cr2O3												
FeO	12.0138	12.0589	12.3051	11.4892	12.1618	12.0055	12.1191	12.6304	12.198	12.194	12.4948	11.3727
MnO	0.3547	0.3814	0.4208	0.3457	0.3005	0.3959	0.3944	0.356	0.3815	0.4172	0.4496	0.3891
MgO	14.1698	13.8992	13.5919	13.5428	13.7946	14.0054	14.2636	13.9826	14.1425	14.1825	14.264	13.9742
ZnO												
CaO	11.0234	11.1194	11.083	10.8973	11.1514	11.2554	11.2863	11.191	11.3274	11.3061	11.2956	10.7498
Na2O	2.265	2.4279	2.5082	2.3071	2.4626	2.3144	2.4223	2.3213	2.409	2.355	2.2676	2.398
K2O	0.8048	0.6865	0.7345	0.7089	0.7827	0.7806	0.7906	0.842	0.8581	0.8317	0.8854	0.8325
NiO	0.0002	0.0073	0.0002	0.0002	0.0055	0.0182	0.0002	0.0255	0.0455	0.0002	0.0455	0.0002
P	0.0188	0.0094	0.0003	0.0235	0.0422	0.0047	0.061	0.0234	0.0141	0.0515	0.0094	0.0422
S												
Cl												
F												
Total	97.78	95.50	96.36	93.72	96.97	96.68	98.54	98.43	98.98	98.29	98.87	96.14

Mineral	hbl	hbl	hbl	hbl	hbl	hbl	hbl	hbl	hbl	hbl	hbl	hbl
Analysis No.	LO52_C5line3_2	LO52_C5line3_3	LO52_C5line3_4	LO52_C5line3_5	LO52_C5line3_6	LO52_C5line3_7	LO52_C5line3_8	LO52_C5line3_9	LO52_C6line1_2	LO52_C6line1_3	LO52_C6line1_4	LO52_C6line1_7
Run ID	tm130709	tm130709	tm130709	tm130709	tm130709	tm130709	tm130709	tm130709	tm130709	tm130709	tm130709	tm130709
SiO2	43.8886	43.0977	43.3062	43.5319	43.7503	43.2587	43.4437	43.0592	43.6678	40.3549	42.4102	43.8071
TiO2	3.1757	3.3378	3.426	3.3322	3.3295	3.4403	3.4046	3.3863	3.1497	3.1364	3.329	3.3319
Al2O3	10.5908	10.4437	10.3719	10.3931	10.1835	10.3807	10.3671	10.3805	10.2232	9.5305	10.1718	10.2767
Cr2O3												
FeO	12.3297	12.2764	12.6454	12.5573	12.2972	12.3181	12.062	12.3749	12.4562	11.7668	12.199	12.4867
MnO	0.3887	0.3329	0.4226	0.4332	0.3977	0.3527	0.3834	0.3546	0.4246	0.3361	0.426	0.4515
MgO	14.6619	14.4602	14.628	14.5781	14.4161	14.4362	14.2904	14.513	14.5805	12.885	13.7595	14.4419
ZnO												
CaO	10.998	11.5892	11.1465	11.255	11.466	11.2413	11.276	11.2419	11.232	11.1314	11.3108	11.479
Na2O	2.333	2.2346	2.3349	2.3653	2.3241	2.3117	2.3146	2.3264	2.3924	2.1007	2.2095	2.3593
K2O	0.8423	0.8476	0.8581	0.8725	0.8735	0.8978	0.8446	0.8752	0.798	0.8295	0.8794	0.8625
NiO	0.0182	0.0127	0.0002	0.0854	0.0109	0.0002	0.0002	0.0182	0.0309	0.0002	0.0509	0.0073
P	0.0047	0.0515	0.0422	0.0141	0.0281	0.0656	0.0375	0.075	0.0234	0.0234	0.0234	0.0422
S												
Cl												
F												
Total	99.23	98.68	99.18	99.42	99.08	98.70	98.42	98.61	98.98	92.09	96.77	99.55

Mineral	hbl	hbl	hbl	hbl	hbl	hbl	hbl	hbl	hbl	hbl	hbl	hbl
Analysis No.	LO52_C6line1_8	LO52_C6line1_9	LO52_C6line2_2	LO52_C6line2_3	LO52_C6line2_4	LO52_C6line2_5	LO52_C6line2_6	LO52_C6line2_7	LO52_C6line2_8	LO52_C6line2_9	LO52_C7line1_3	LO52_C7line1_4
Run ID	tm130709	tm130709	tm130709	tm130709	tm130709	tm130709	tm130709	tm130709	tm130709	tm130709	tm130709	tm130709
SiO2	40.9615	43.7207	43.0605	42.0788	42.2697	42.9526	42.9711	43.0639	43.3581	43.0441	41.4944	40.9599
TiO2	3.1342	3.1266	3.2348	3.3465	3.4948	3.4827	3.3787	3.2697	3.3266	3.1013	3.2164	3.3313
Al2O3	10.0008	10.4804	10.662	10.2119	10.4325	10.5752	10.6318	10.2679	10.441	10.2712	10.7056	11.0939
Cr2O3												
FeO	11.7615	12.1651	12.2478	11.9264	12.5119	12.3451	12.502	12.2866	12.1886	12.2281	12.2017	12.1997
MnO	0.4117	0.3904	0.4229	0.4246	0.415	0.3363	0.4242	0.3868	0.3885	0.3974	0.3541	0.3111
MgO	13.5572	14.4202	14.6351	13.5936	14.2441	14.362	14.5223	14.2042	14.5703	14.1497	13.3136	13.3385
ZnO												
CaO	10.4205	11.3084	11.4215	10.9646	11.3166	11.2043	11.1716	11.3186	11.3906	11.3046	11.1824	11.1993
Na2O	2.2741	2.3504	2.3899	2.2404	2.317	2.3091	2.3422	2.2492	2.3236	2.357	2.3561	2.4756
K2O	0.7649	0.8549	0.8614	0.8446	0.8997	0.8908	0.8935	0.8518	0.8741	0.8543	0.8561	0.8092
NiO	0.0002	0.0002	0.0164	0.0255	0.069	0.0018	0.0473	0.0002	0.04	0.0002	0.0309	0.0091
P	0.0844	0.0047	0.0609	0.0422	0.0187	0.0003	0.0375	0.0281	0.0703	0.0375	0.0608	0.0374
S												
Cl												
F												
Total	93.37	98.82	99.01	95.70	97.99	98.46	98.92	97.93	98.97	97.75	95.77	95.77

Mineral	hbl	hbl	hbl	hbl	hbl	hbl	hbl	hbl	hbl	hbl	hbl
Analysis No.	LO52_C7line1_5	LO52_C7line1_6	LO52_C7line1_7	LO52_C7line1_8	LO52_C7line1_9	LO52_C7line1_10	LO52_C7line1_11	LO52_C7line1_12	LO52_C7line1_14	LO52_C7line1_15	LO52_C7line1_16
Run ID	tm130709	tm130709	tm130709	tm130709	tm130709	tm130709	tm130709	tm130709	tm130709	tm130709	tm130709
SiO2	41.4856	41.1762	41.5505	41.8831	42.9609	42.1251	42.3293	41.961	43.1941	42.8596	43.244
TiO2	3.2751	3.271	3.2867	3.274	3.2678	3.3372	3.3689	3.3253	3.3418	3.3496	3.4393
Al2O3	11.1277	10.9675	11.1952	10.6253	10.4565	10.7472	10.8176	10.8541	10.2729	10.2394	10.2444
Cr2O3											
FeO	12.3126	12.0806	12.5893	12.0314	11.9801	11.9909	12.3435	12.2018	12.0363	12.0224	12.1934
MnO	0.3917	0.4098	0.3358	0.3291	0.3004	0.4152	0.3415	0.3739	0.3957	0.3939	0.3363
MgO	13.2952	13.4224	13.2189	13.57	13.7224	13.6604	13.5569	13.5709	13.9327	13.9925	13.9443
ZnO											
CaO	11.1992	11.0546	11.2126	11.2228	11.1374	11.2514	11.1755	11.363	11.1622	11.7932	11.4392
Na2O	2.358	2.4228	2.4569	2.5398	2.3824	2.3874	2.3986	2.4413	2.3009	2.3763	2.3064
K2O	0.8161	0.8105	0.8549	0.7906	0.8151	0.7969	0.8031	0.8436	0.863	0.8368	0.8942
NiO	0.0618	0.02	0.0002	0.0254	0.0182	0.0145	0.0254	0.0073	0.0091	0.0255	0.0002
P	0.0515	0.0281	0.1308	0.0234	0.0141	0.014	0.0328	0.0748	0.0515	0.1543	0.0328
S											
Cl											
F											
Total	96.37	95.66	96.83	96.31	97.06	96.74	97.19	97.02	97.56	98.04	98.07

Mineral	hbl	hbl	hbl	hbl	hbl	hbl	hbl	hbl	hbl	hbl	hbl
Analysis No.	LO52_C7line1_17	LO52_C7line1_18	LO52_C7line1_19	LO52_C7point1	LO52_C7line2_2	LO52_C7line2_3	LO52_C7line2_5	LO52_C7line2_6	LO52_C7line2_7	LO52_C7line2_8	LO52_C7line2_9
Run ID	tm130709	tm130709	tm130709	tm130709	tm130709	tm130709	tm130709	tm130709	tm130709	tm130709	tm130709
SiO2	43.1966	43.4678	43.3538	42.5832	41.5764	41.7846	41.8239	42.1323	41.8386	41.9683	42.1289
TiO2	3.4479	3.269	3.2055	3.4206	3.0032	3.3105	3.0746	3.2553	3.2036	3.1527	3.204
Al2O3	10.4858	10.303	10.4868	10.2343	9.937	10.3935	10.645	10.9746	10.5875	10.9167	11.1007
Cr2O3											
FeO	11.9743	11.8939	11.9346	12.3988	11.9235	11.957	12.0123	12.1514	12.2416	12.6944	12.4588
MnO	0.4101	0.3941	0.3401	0.3844	0.3737	0.3432	0.3723	0.4027	0.4114	0.3916	0.3808
MgO	13.9505	13.871	14.1882	13.8159	12.9046	13.4646	13.7708	13.4733	13.5841	13.5111	13.6161
ZnO											
CaO	11.2269	11.3426	11.3088	10.7378	10.8133	11.1035	11.3459	11.1533	11.1481	11.187	11.3921
Na2O	2.3484	2.4039	2.382	2.1802	2.2258	2.423	2.4231	2.4604	2.4564	2.4132	2.3767
K2O	0.865	0.9313	0.8068	0.8475	0.7686	0.839	0.7781	0.8181	0.8174	0.8001	0.8364
NiO	0.0818	0.0002	0.0002	0.0002	0.0002	0.0491	0.0002	0.0002	0.0002	0.0002	0.0073
P	0.0003	0.0703	0.0094	0.0281	0.0468	0.0003	0.0375	0.0328	0.0421	0.014	0.0234
S											
Cl											
F											
Total	97.99	97.95	98.02	96.63	93.57	95.67	96.28	96.85	96.33	97.05	97.53

Mineral	hbl	hbl	hbl	hbl	hbl	hbl	hbl	hbl	hbl	hbl	hbl
Analysis No.	LO52_C7line2_10	LO52_C7line2_11	LO52_C7line2_12	LO52_C7line2_13	LO52_C7line2_14	LO52_C12line1_2	LO52_C12line1_3	LO52_C12line1_4	LO52_C1_line1_3	LO52_C1_line1_4	LO52_C1_line1_5
Run ID	tm130709	tm130709	tm130709	tm130709	tm130709	tm130709	tm130709	tm130709	tm130709	tm130709	tm130709
SiO2	42.2988	43.285	43.5296	43.2728	43.5277	43.3395	42.8606	43.1813	43.5602	43.7043	43.3781
TiO2	3.3103	3.3716	3.6543	3.6352	3.0565	3.1929	3.1966	3.2118	2.851	2.8807	2.9743
Al2O3	11.0378	10.7954	10.1819	10.1559	10.6992	10.8022	10.399	10.6062	9.7255	9.9332	9.791
Cr2O3											
FeO	12.159	12.2014	12.2634	11.943	12.2965	12.1255	11.9548	12.2604	12.2357	12.2889	12.4777
MnO	0.3469	0.338	0.374	0.4048	0.338	0.3341	0.3556	0.4204	0.4256	0.4382	0.4146
MgO	13.5919	13.7062	13.9436	13.8704	14.1255	14.2941	13.7639	13.9051	14.0669	14.1368	13.9489
ZnO											
CaO	11.2555	11.3006	11.1987	11.1902	11.0766	11.3705	11.265	11.558	10.947	11.164	10.9039
Na2O	2.4837	2.5019	2.3924	2.365	2.3386	2.4875	2.3573	2.3543	2.4151	2.4126	2.367
K2O	0.7711	0.8314	0.9449	0.9294	0.8291	0.8328	0.8124	0.8615	0.7804	0.7941	0.7657
NiO	0.0055	0.0091	0.0473	0.0002	0.0002	0.0002	0.02	0.0002	0.0002	0.0036	0.0054
P	0.0515	0.0003	0.0003	0.0328	0.0375	0.0515	0.0421	0.0094	0.0234	0.0003	0.0003
S											
Cl											
F											
Total	97.31	98.34	98.53	97.80	98.33	98.83	97.03	98.37	97.03	97.76	97.03

Mineral	hbl	hbl	hbl	hbl	hbl	hbl	hbl	hbl	hbl	hbl	hbl
Analysis No.	LO52_C1_line1_6	LO52_C1_line1_7	LO52_C1_line1_8	LO52_C1_line1_9	LO52_C1_line1_10	LO52_C1_line1_11	LO52_C1_line1_12	LO52_C1_line1_13	LO52_C1_line1_14	LO52_C1_line1_15	LO52_C1_line1_16
Run ID	tm130709	tm130709	tm130709	tm130709	tm130709	tm130709	tm130709	tm130709	tm130709	tm130709	tm130709
SiO2	44.0098	42.3925	44.1742	44.0087	43.5478	43.724	43.6739	43.3513	43.5514	43.8141	43.8488
TiO2	2.8111	2.7349	2.8479	2.8834	2.9017	3.014	3.054	3.1733	3.1907	3.1515	3.1245
Al2O3	9.8154	9.5948	10.1705	9.994	10.3679	10.3175	10.2745	10.2292	10.3628	10.2988	10.1614
Cr2O3											
FeO	12.2728	12.0115	12.23	12.1459	12.2942	12.2625	12.2457	12.161	12.2163	12.3859	12.415
MnO	0.5154	0.4219	0.4311	0.3808	0.3701	0.3879	0.4382	0.3878	0.4238	0.4525	0.4201
MgO	14.2149	13.7795	14.4697	14.2086	14.2268	14.1282	13.8905	14.0575	13.9992	14.3665	14.1554
ZnO											
CaO	11.2044	10.6004	10.9915	11.2409	11.1121	11.1044	11.357	11.3836	11.2184	11.1865	11.1823
Na2O	2.3267	2.3499	2.4647	2.3522	2.4648	2.3698	2.3167	2.3238	2.3746	2.3296	2.352
K2O	0.7874	0.6922	0.733	0.7988	0.7821	0.809	0.7892	0.7985	0.7991	0.8458	0.8364
NiO	0.0002	0.0254	0.0002	0.0182	0.0002	0.0218	0.0002	0.0002	0.0002	0.0002	0.0127
P	0.0234	0.0469	0.0141	0.0003	0.0516	0.0047	0.0003	0.0748	0.0187	0.0003	0.0047
S											
Cl											
F											
Total	97.98	94.65	98.53	98.03	98.12	98.14	98.04	97.94	98.16	98.83	98.51

Mineral	hbl	hbl	hbl	hbl	hbl	hbl	hbl	hbl	hbl
Analysis No.	LO52_C1_line1_17	Lo39MGM_cir1line1_1	Lo39MGM_cir1line1_2	Lo39MGM_cir1line1_3	Lo39MGM_cir1line1_4	Lo39MGM_cir1line1_5	Lo39MGM_cir1line1_6	Lo39MGM_cir1line1_7	Lo39MGM_cir1line1_8
Run ID	tm130709	tm070909	tm070909	tm070909	tm070909	tm070909	tm070909	tm070909	tm070909
SiO2	43.2067	42.3071	42.6984	42.144	42.1653	42.0649	41.7786	41.7525	41.6169
TiO2	3.1088	3.1682	3.0994	3.058	3.2839	3.3243	3.2753	3.2488	3.1926
Al2O3	10.4533	10.0243	9.9083	10.1143	10.0031	9.8745	9.9476	9.7312	9.7004
Cr2O3									
FeO	12.3167	12.1347	12.1566	12.3257	12.138	12.2864	11.9713	11.8364	11.9232
MnO	0.4004	0.3561	0.461	0.3815	0.4049	0.3975	0.3544	0.4175	0.3904
MgO	14.2978	13.8574	13.9526	13.8164	13.6424	13.9537	13.8271	13.5978	13.6475
ZnO		0.0263	0.0029	0.0029	0.0175	0.1021	0.0002	0.1489	0.0671
CaO	11.4308	11.3958	11.1661	11.2753	11.2328	11.0553	11.1863	10.9916	10.9627
Na2O	2.3916	2.269	2.3553	2.3192	2.3422	2.3931	2.3788	2.3096	2.2113
K2O	0.8319	0.883	0.8023	0.8881	0.8568	0.8577	0.8722	0.8264	0.8571
NiO	0.0002	0.0368	0.0002	0.0002	0.0002	0.0221	0.0002	0.0002	0.0221
P	0.0374	0.0001	0.0093	0.0371	0.0162	0.0093	0.0139	0.0464	0.0278
S		0.0013	0.0201	0.0107	0.0201	0.0001	0.0001	0.004	0.0282
Cl									
F									
Total	98.48	96.46	96.63	96.37	96.12	96.34	95.61	94.91	94.65

Mineral	hbl	hbl	hbl	hbl	hbl	hbl	hbl	hbl	hbl
Analysis No.	Lo39MGM_cir1line1_9	Lo39MGM_cir1line1_10	Lo39MGM_cir1line1_11	Lo39MGM_cir1line1_12	Lo39MGM_cir10spot2	Lo39MGM_cir10spot3	Lo39MGM_cir10spot4	Lo39MGM_cir11spot2	Lo39MGM_cir11line1_1
Run ID	tm070909	tm070909	tm070909	tm070909	tm070909	tm070909	tm070909	tm070909	tm070909
SiO2	41.3428	41.5362	41.2879	41.1678	42.2106	42.3854	42.7177	41.8901	42.3663
TiO2	3.3093	3.1719	2.8831	2.9805	3.0048	2.8172	3.0145	3.0578	3.1477
Al2O3	9.6977	9.8737	9.7828	10.1582	10.1331	10.9591	10.2257	9.9722	9.9305
Cr2O3									
FeO	11.7993	11.9959	11.9942	12.022	12.4276	12.194	12.6634	12.5113	12.1722
MnO	0.3707	0.3834	0.4087	0.3348	0.4436	0.3514	0.3892	0.3747	0.4022
MgO	13.7826	13.6778	13.8797	13.7579	13.7929	13.9859	13.7584	13.961	13.9749
ZnO	0.0002	0.0234	0.0002	0.0002	0.0002	0.0381	0.0292	0.0002	0.0002
CaO	10.8589	11.0976	10.8387	11.0191	11.0921	11.1158	11.2886	11.3675	11.2184
Na2O	2.3836	2.4213	2.2847	2.3933	2.3502	2.4753	2.3113	2.3983	2.3377
K2O	0.7994	0.823	0.7929	0.8554	0.8317	0.5799	0.8433	0.8012	0.8535
NiO	0.0147	0.0349	0.0002	0.0002	0.0184	0.0553	0.0002	0.07	0.0002
P	0.0162	0.0464	0.0093	0.0139	0.0001	0.014	0.0186	0.0093	0.007
S	0.0067	0.0121	0.0001	0.0081	0.0202	0.0067	0.0134	0.0295	0.0001
Cl									
F									
Total	94.38	95.10	94.16	94.71	96.33	96.98	97.27	96.44	96.41

Mineral	hbl	hbl	hbl	hbl	hbl	hbl	hbl	hbl
Analysis No.	Lo39MGM_cir11line1_2	Lo39MGM_cir11line1_3	Lo39MGM_cir11line1_4	Lo39MGM_cir11line1_5	Lo39MGM_cir11line1_6	Lo39MGM_cir11line1_8	Lo39MGM_cir11line1_9	Lo39MGM_cir11line1_10
Run ID	tm070909	tm070909	tm070909	tm070909	tm070909	tm070909	tm070909	tm070909
SiO2	42.5297	42.2498	42.4446	39.6964	42.3501	42.2393	42.0531	42.1977
TiO2	3.0683	3.1455	3.0535	2.9767	3.1045	2.9634	2.9392	2.9897
Al2O3	10.2509	10.2437	10.3689	10.122	9.9015	9.9762	9.852	9.9389
Cr2O3								
FeO	12.2326	12.2237	12.6116	10.2784	12.1616	12.505	12.5881	12.5417
MnO	0.4236	0.3367	0.3856	0.3486	0.4309	0.3926	0.4452	0.4852
MgO	13.9052	13.799	13.7201	13.4034	13.8875	13.9749	13.9361	14.1965
ZnO	0.0263	0.0175	0.0117	0.0002	0.0439	0.0002	0.0263	0.1726
CaO	11.0601	11.0694	11.1508	10.3773	11.1686	11.1912	11.1664	11.3413
Na2O	2.3091	2.2843	2.3544	2.38	2.3239	2.3993	2.3147	2.3569
K2O	0.8209	0.8198	0.8959	0.713	0.826	0.7662	0.8277	0.8425
NiO	0.0002	0.0368	0.0239	0.0277	0.0002	0.0589	0.0055	0.0147
P	0.0001	0.0023	0.0001	0.0093	0.0001	0.0441	0.0093	0.0232
S	0.0188	0.004	0.0363	0.0189	0.0188	0.0148	0.0001	0.0148
Cl								
F								
Total	96.65	96.23	97.06	90.35	96.22	96.53	96.16	97.12

Mineral	hbl	hbl	hbl	hbl	hbl	hbl	hbl	hbl
Analysis No.	Lo39MGM_cir11line1_11	Lo39MGM_cir11line1_12	Lo39MGM_cir11line1_13	Lo39MGM_cir11line1_14	Lo39MGM_cir11line1_15	Lo54MGM_cir1spot2	Lo54MGM_cir1spot3MI	Lo54MGM_cir2spot2
Run ID	tm070909	tm070909	tm070909	tm070909	tm070909	tm070909	tm070909	tm070909
SiO2	41.9188	41.6717	41.9576	41.7574	42.5718	43.0469	45.3537	42.952
TiO2	3.0312	3.2652	3.0635	2.9778	2.9842	3.6522	3.5055	3.5467
Al2O3	9.9658	10.0414	10.169	9.985	9.8511	10.4315	10.7622	10.3077
Cr2O3								
FeO	12.4082	12.4476	12.4356	12.19	12.1285	13.6376	13.6916	13.4746
MnO	0.335	0.3564	0.3584	0.373	0.4383	0.3999	0.4113	0.4363
MgO	13.8652	13.8175	13.837	13.7621	14.1767	13.517	14.5663	13.465
ZnO	0.0002	0.0585	0.1111	0.0176	0.0819	0.1053	0.0002	0.0263
CaO	11.2197	11.1182	11.0899	11.3042	11.2633	11.3793	11.1101	11.2791
Na2O	2.3173	2.4032	2.3112	2.2782	2.4018	2.3635	2.6745	2.4198
K2O	0.8297	0.7845	0.8125	0.7645	0.8166	0.88	0.9051	0.8766
NiO	0.0147	0.0002	0.0002	0.0553	0.0387	0.0479	0.0002	0.0129
P	0.0093	0.0046	0.0001	0.0001	0.007	0.0116	0.014	0.0163
S	0.0081	0.0001	0.0188	0.0067	0.0054	0.0001	0.0256	0.0001
Cl								
F								
Total	95.92	95.97	96.16	95.47	96.77	99.47	103.02	98.81

Mineral	hbl	hbl	hbl	hbl	hbl	hbl	hbl	hbl	hbl
Analysis No.	Lo54MGM_cir2spot3	Lo54MGM_cir2spot4	Lo54MGM_cir3spot2	Lo54MGM_cir3spot3	Lo54MGM_cir4spot2	Lo54MGM_cir4spot3	Lo23PGM_cir6spot6	Lo23MGM_cir3spot2	Lo23MGM_cir3line1_1
Run ID	tm070909	tm070909	tm070909	tm070909	tm070909	tm070909	tm070909	tm070909	tm070909
SiO2	34.2574	42.8489	43.3513	42.9876	43.2816	43.1255	43.2887	43.6058	42.9049
TiO2	2.8086	3.4859	3.4853	3.5357	3.5794	3.5723	3.1747	3.1998	3.1149
Al2O3	8.7949	10.3921	10.3331	10.5146	10.5314	10.7405	10.3986	10.4534	10.0392
Cr2O3									
FeO	10.4197	13.0063	13.5298	13.3927	13.3789	13.4085	12.5834	12.2409	12.5862
MnO	0.2936	0.4113	0.3856	0.4778	0.4312	0.4129	0.3958	0.4508	0.3523
MgO	11.4595	13.4766	13.7316	13.7458	13.642	13.5464	14.0047	14.4296	13.9635
ZnO	0.0002	0.0002	0.0936	0.1638	0.0468	0.0002	0.0528	0.0088	0.0117
CaO	8.9607	11.1404	11.3009	11.1323	11.0925	11.1075	11.2148	11.4751	11.0536
Na2O	1.9928	2.356	2.3162	2.4177	2.3528	2.3673	2.3646	2.3591	2.3169
K2O	0.7203	0.8748	0.9042	0.9629	0.9448	0.889	0.8087	0.8175	0.7574
NiO	0.0516	0.0332	0.0037	0.0461	0.0111	0.0111	0.0002	0.0002	0.0166
P	0.0001	0.0395	0.0001	0.0279	0.0046	0.0023	0.021	0.021	0.0001
S	0.0148	0.0175	0.004	0.0001	0.0188	0.0001	0.0337	0.0013	0.0081
Cl									
F									
Total	79.77	98.08	99.44	99.41	99.32	99.18	98.34	99.06	97.13

Mineral	hbl	hbl	hbl	hbl	hbl	hbl	hbl	hbl
Analysis No.	Lo23MGM_cir3line1_5	Lo23MGM_cir3line1_6	Lo23MGM_cir3line1_7	Lo23MGM_cir3line1_8	Lo23MGM_cir3line1_9	Lo23MGM_cir3line1_10	Lo23MGM_cir5line1_6	Lo23MGM_cir5line1_7
Run ID	tm070909	tm070909	tm070909	tm070909	tm070909	tm070909	tm070909	tm070909
SiO2	43.5646	43.4204	43.531	43.6727	43.7609	43.4047	43.9003	43.998
TiO2	3.3215	3.3591	3.3309	3.3756	3.1806	3.2926	2.9283	2.8935
Al2O3	10.6828	10.4765	10.5221	10.5537	10.499	10.646	10.0478	9.8955
Cr2O3								
FeO	12.4662	12.5489	12.4021	12.5031	12.5185	12.3738	12.6805	12.6761
MnO	0.3964	0.3781	0.3673	0.4253	0.3872	0.3945	0.5397	0.4489
MgO	14.3752	14.3552	14.4149	14.4483	14.6604	14.6063	14.2467	14.3005
ZnO	0.0002	0.0176	0.0002	0.0675	0.0587	0.0881	0.0002	0.0002
CaO	11.4443	11.3412	11.3226	11.3985	11.2615	11.3516	11.2847	10.9116
Na2O	2.4251	2.4036	2.3746	2.4646	2.4493	2.4306	2.3679	2.3719
K2O	0.8141	0.8557	0.8479	0.8177	0.8246	0.8724	0.7735	0.8059
NiO	0.0002	0.0388	0.0388	0.0296	0.0002	0.0148	0.0002	0.0002
P	0.0093	0.0047	0.0373	0.0001	0.021	0.0001	0.0327	0.0001
S	0.0001	0.0013	0.0094	0.0121	0.0122	0.0189	0.0001	0.0001
Cl								
F								
Total	99.50	99.20	99.20	99.77	99.63	99.49	98.80	98.30

Mineral	hbl	hbl	hbl	hbl	hbl	hbl	hbl	hbl	hbl
Analysis No.	Lo23MGM_cir5line1_8	Lo23MGM_cir5line1_9	Lo23MGM_cir8line1_2	Lo23MGM_cir8line1_3	Lo23MGM_cir8line1_4	Lo23MGM_cir8line1_5	Lo23MGM_cir8line1_6	Lo23MGM_cir8line1_7	Lo23MGM_cir8line1_8
Run ID	tm070909	tm070909	tm070909	tm070909	tm070909	tm070909	tm070909	tm070909	tm070909
SiO2	43.7399	43.9667	43.4012	43.2428	43.1886	43.0327	43.5512	43.2907	43.4272
TiO2	2.9836	2.8701	3.1947	3.177	3.3086	3.5571	3.5571	3.5637	3.5175
Al2O3	9.9563	9.8188	10.311	10.3841	10.1567	10.2316	10.2557	10.3515	10.442
Cr2O3									
FeO	12.775	13.0285	12.2496	12.4993	12.5433	12.4408	12.6429	12.3426	12.6485
MnO	0.4996	0.4669	0.413	0.3182	0.4182	0.3618	0.4184	0.2892	0.3672
MgO	14.1563	14.2928	14.08	14.3124	14.2494	14.1686	14.2434	14.2717	14.2692
ZnO	0.0002	0.0734	0.0206	0.1263	0.0002	0.0617	0.0002	0.0294	0.0352
CaO	11.3323	11.0054	11.4103	11.1695	11.1061	11.1523	11.2749	11.26	11.1676
Na2O	2.3383	2.2976	2.3674	2.3342	2.3833	2.4752	2.3946	2.4026	2.3914
K2O	0.8502	0.8176	0.7737	0.8829	0.8108	0.8896	0.8963	0.8753	0.8815
NiO	0.037	0.0703	0.013	0.0259	0.0002	0.0185	0.0002	0.0296	0.0351
P	0.014	0.007	0.007	0.0001	0.0257	0.021	0.0187	0.0233	0.0093
S	0.0081	0.0176	0.027	0.0108	0.0149	0.0202	0.0054	0.0001	0.0001
Cl									
F									
Total	98.69	98.73	98.27	98.48	98.21	98.43	99.26	98.73	99.19

Mineral	hbl	hbl	hbl	hbl	hbl	hbl	hbl	hbl	hbl	hbl	hbl
Analysis No.	Lo23MGM_cir8line1_9	Lo23MGM_cir8line1_10	Lo23MGM_cir12spot2	Lo23MGM_cir12spot3	Lo39_cir1spot1	Lo39_cir1spot2	Lo39_cir1spot3	Lo39_cir1line1_5	Lo39_cir1line1_6	Lo39_cir1line1_7	Lo39_cir1line1_8
Run ID	tm070909	tm070909	tm070909	tm070909	tm070909	tm070909	tm070909	tm070909	tm070909	tm070909	tm070909
SiO2	43.2803	43.6918	43.7471	44.0085	43.58	43.5797	42.9653	42.2055	43.1673	42.9671	43.2818
TiO2	3.4206	3.1277	3.2791	3.1294	3.0414	3.2279	3.228	3.0672	3.2028	2.7787	3.196
Al2O3	10.4969	10.6371	10.4961	10.4977	10.1344	10.4614	10.2951	10.187	10.3991	10.2912	10.3474
Cr2O3											
FeO	12.6102	12.1691	12.61	12.4925	12.4174	11.9387	12.5287	12.071	12.2879	12.5593	12.4938
MnO	0.4401	0.3385	0.3965	0.4623	0.437	0.3197	0.4255	0.431	0.3688	0.4312	0.411
MgO	14.2842	14.4092	14.7267	14.808	14.1778	14.4277	14.2972	14.0456	14.3303	14.1446	14.2338
ZnO	0.1439	0.0118	0.0088	0.0176	0.1098	0.0445	0.003	0.2104	0.0207	0.0415	0.1186
CaO	11.3116	11.2525	11.3711	11.2037	11.3416	11.2951	11.2546	11.0929	11.2755	11.2409	11.2398
Na2O	2.4617	2.3858	2.3977	2.4693	2.3564	2.3902	2.3276	2.2306	2.3597	2.2966	2.3202
K2O	0.8663	0.8109	0.8465	0.8503	0.8492	0.8118	0.88	0.7858	0.8474	0.8589	0.8935
NiO	0.0002	0.0167	0.0002	0.0002	0.0037	0.0392	0.0002	0.0002	0.0504	0.0002	0.0002
P	0.0257	0.028	0.014	0.0094	0.0047	0.0142	0.0071	0.0094	0.0141	0.0001	0.0024
S	0.0121	0.0001	0.0001	0.0108	0.0001	0.0082	0.0204	0.0001	0.0163	0.0286	0.0123
Cl											
F											
Total	99.35	98.88	99.89	99.96	98.45	98.56	98.23	96.34	98.34	97.64	98.55

Mineral	hbl	hbl	hbl	hbl	hbl	hbl	hbl	hbl	hbl	hbl	hbl
Analysis No.	Lo39_cir1line1_9	Lo39_cir1line1_10	Lo39_cir1line1_11	Lo39_cir1line1_12	Lo39_cir1line1_13	Lo39_cir1line1_14	Lo39_cir1line1_15	Lo39_cir2spot1	Lo39_cir2spot2	Lo39_cir2spot3	Lo39_cir2line1_7
Run ID	tm070909	tm070909	tm070909	tm070909	tm070909	tm070909	tm070909	tm070909	tm070909	tm070909	tm070909
SiO2	43.0741	43.1382	43.081	41.8009	43.6497	43.2975	42.9997	42.4834	43.1694	54.2047	42.3252
TiO2	3.2743	3.3217	3.2725	3.2198	3.1309	3.2292	3.3053	3.0703	2.8965	0.2235	3.0336
Al2O3	10.2936	10.4739	10.4256	10.1672	10.1785	10.187	10.4007	11.1089	11.0381	1.0129	10.9117
Cr2O3											
FeO	12.3031	11.9842	12.1903	11.7977	12.4432	12.3811	12.4878	12.3527	11.7866	17.1333	12.0481
MnO	0.448	0.3637	0.3524	0.4443	0.4055	0.3249	0.389	0.3965	0.4117	1.1855	0.2241
MgO	14.178	14.2078	14.2376	13.9354	14.4615	14.2461	14.2913	14.1086	14.5867	26.3723	13.9176
ZnO	0.1008	0.0002	0.0002	0.0002	0.0002	0.0445	0.0563	0.0002	0.0002	0.1162	0.0002
CaO	11.2261	11.4616	11.3028	10.8717	8.6546	11.4617	11.2438	11.249	11.115	1.2184	11.4687
Na2O	2.4501	2.4663	2.4499	2.2832	2.4014	2.3605	2.3096	2.3874	2.4515	0.0418	2.3275
K2O	0.9278	0.8946	0.8245	0.7956	0.8724	0.864	0.8357	0.779	0.727	0.0001	0.9735
NiO	0.0448	0.0149	0.0002	0.028	0.0002	0.0317	0.0131	0.0149	0.0002	0.0188	0.0355
P	0.0259	0.0001	0.0141	0.0071	0.0001	0.0188	0.0471	0.0094	0.0001	0.0001	0.0001
S	0.015	0.0136	0.0001	0.0259	0.0301	0.0001	0.0191	0.0068	0.0109	0.0001	0.03
Cl											
F											
Total	98.36	98.34	98.15	95.38	96.23	98.45	98.40	97.97	98.19	101.53	97.30

Mineral	hbl	hbl	hbl	hbl	hbl	hbl	hbl	hbl	hbl	hbl	hbl
Analysis No.	Lo39_cir3line1_6	Lo39_cir3line1_7	Lo39_cir3line1_8	Lo39_cir3line1_9	Lo39_cir3line1_10	Lo39_cir3line1_11	Lo39_cir3line1_12	Lo39_cir3line1_13	Lo39_cir3line1_14	Lo39_cir3line1_15	Lo39_cir3line1_18
Run ID	tm070909	tm070909	tm070909	tm070909	tm070909	tm070909	tm070909	tm070909	tm070909	tm070909	tm070909
SiO2	43.3729	41.204	43.3227	43.0049	43.0055	43.0164	43.1846	42.6299	43.2659	42.7992	42.9618
TiO2	3.2204	3.3474	3.3454	3.3782	3.4679	3.5047	3.4986	3.4618	3.5194	3.5819	3.311
Al2O3	10.291	9.6917	10.4447	10.4753	10.3829	10.3207	10.3315	10.0526	10.2332	10.4016	10.3736
Cr2O3											
FeO	12.1011	11.6771	12.4482	12.4606	12.2951	12.5562	12.2385	11.6795	12.4716	11.8758	12.3163
MnO	0.3861	0.421	0.3236	0.3621	0.375	0.3253	0.3919	0.3534	0.4303	0.4086	0.3513
MgO	14.2075	13.6623	14.3628	14.3435	14.1305	14.241	14.1862	14.0376	14.2647	14.293	14.3139
ZnO	0.0148	0.1009	0.0002	0.0505	0.0653	0.0002	0.0002	0.0178	0.0148	0.0002	0.0743
CaO	11.183	10.9327	11.1518	11.173	11.2691	11.2039	11.2769	11.0238	11.567	10.9184	11.379
Na2O	2.3895	2.1164	2.3674	2.4306	2.3697	2.358	2.3757	2.2692	2.2932	2.3947	2.3383
K2O	0.9272	0.8155	0.9604	0.8902	0.9167	0.9185	0.8952	0.9389	0.9413	0.8665	0.8703
NiO	0.0002	0.0002	0.0318	0.028	0.0449	0.0112	0.0002	0.1123	0.0318	0.0002	0.0393
P	0.0001	0.0283	0.0236	0.0001	0.0354	0.0377	0.0001	0.0189	0.0189	0.0094	0.0071
S	0.0259	0.0395	0.0096	0.0123	0.0082	0.0136	0.0177	0.0164	0.0177	0.0205	0.0096
Cl											
F											
Total	98.12	94.04	98.79	98.61	98.37	98.51	98.40	96.61	99.07	97.57	98.35

Mineral	hbl	hbl	hbl	hbl	hbl	hbl	hbl	hbl	hbl	hbl	hbl
Analysis No.	Lo39_cir3line1_19	Lo39_cir5spot2	Lo39_cir5line1_9	Lo39_cir5line1_10	Lo39_cir5line1_11	Lo39_cir5line1_12	Lo39_cir5line1_13	Lo39_cir5line1_14	Lo39_cir5line1_15	Lo39_cir5line1_16	Lo39_cir6spot2
Run ID	tm070909	tm070909	tm070909	tm070909	tm070909	tm070909	tm070909	tm070909	tm070909	tm070909	tm070909
SiO2	42.9066	43.1323	43.4661	43.1619	42.986	42.7215	41.8877	43.1514	42.8331	43.2886	43.0349
TiO2	3.205	3.6122	2.9763	3.2118	3.1797	3.4162	3.4508	3.0693	3.1942	2.8372	3.1594
Al2O3	10.421	10.2827	10.0787	10.3936	10.4668	10.7028	10.077	10.2161	10.3699	10.1517	10.585
Cr2O3											
FeO	12.3104	12.2089	12.3543	12.3139	12.095	12.1609	11.8814	12.6462	12.7037	12.3124	12.2346
MnO	0.3294	0.3038	0.3573	0.4216	0.4239	0.3517	0.2836	0.3846	0.4506	0.4125	0.3573
MgO	14.2004	14.2546	13.9789	14.0115	14.0489	13.8892	13.6287	14.1122	13.982	14.3319	14.279
ZnO	0.0002	0.0002	0.0002	0.1398	0.0002	0.0178	0.0089	0.0476	0.0238	0.0002	0.0357
CaO	11.0954	11.317	11.1167	11.0381	11.1062	11.1587	10.9008	11.0648	11.4515	11.0827	11.2261
Na2O	2.3759	2.3679	2.374	2.3374	2.4165	2.4652	2.2887	2.3707	2.304	2.3684	2.4135
K2O	0.8815	0.9089	0.8455	0.8138	0.8209	0.922	0.8999	0.8312	0.8425	0.7508	0.789
NiO	0.0262	0.1011	0.0002	0.0002	0.0094	0.0468	0.0375	0.0002	0.0187	0.0002	0.0002
P	0.0024	0.026	0.0095	0.0284	0.0001	0.0142	0.0142	0.0001	0.0189	0.0001	0.0001
S	0.0001	0.0123	0.015	0.0109	0.0082	0.0001	0.0001	0.0109	0.0136	0.0164	0.0001
Cl											
F											
Total	97.75	98.53	97.57	97.88	97.56	97.87	95.36	97.91	98.21	97.55	98.11

Mineral	hbl	hbl	hbl	hbl	hbl	hbl	hbl	hbl	hbl	hbl	hbl	hbl
Analysis No.	Lo39_cir6spot3	Lo39_cir6spot4	Lo39_cir9spot1	Lo39_cir9spot2	Lo39_cir9spot3	Lo39_cir12spot2	Lo39_cir12spot3	Lo39_cir12spot4	Lo39_cir12spot6	Lo39_cir12line1_6	Lo39_cir12line1_7	Lo39_cir12line1_8
Run ID	tm070909	tm070909	tm070909	tm070909	tm070909	tm070909	tm070909	tm070909	tm070909	tm070909	tm070909	tm070909
SiO2	43.0138	43.631	43.0752	43.0257	43.8029	43.0727	42.8548	43.3078	43.3029	43.5893	41.909	42.7811
TiO2	3.2157	3.0903	3.4934	3.5891	3.383	3.1437	3.1085	3.5024	3.4188	3.0939	3.1197	2.845
Al2O3	10.2426	10.3794	10.3032	10.2717	9.6459	10.451	10.9338	10.1228	10.3752	10.3765	10.2505	11.0729
Cr2O3												
FeO	12.099	12.3489	12.3435	12.2213	12.168	12.2019	12.4622	12.2138	12.3688	12.2987	12.1823	12.3499
MnO	0.3887	0.3647	0.3867	0.3851	0.4292	0.3575	0.3111	0.3554	0.3536	0.352	0.3479	0.348
MgO	14.3686	14.3923	14.1348	13.9419	14.4189	14.3722	14.2235	14.0599	14.3117	14.2392	13.6889	14.1448
ZnO	0.0625	0.0625	0.0059	0.0002	0.0387	0.0208	0.116	0.0743	0.0002	0.0002	0.0595	0.0714
CaO	11.4819	11.305	11.0621	11.1141	11.2386	11.3015	11.3989	11.2039	11.2826	11.1382	10.8955	11.1497
Na2O	2.2985	2.234	2.2892	2.3992	2.3068	2.3774	2.3921	2.3383	2.3429	2.4153	2.2407	2.3528
K2O	0.8355	0.7799	0.8917	0.9436	0.846	0.8188	0.8235	0.887	0.9358	0.846	0.8135	0.851
NiO	0.0037	0.0002	0.0002	0.0002	0.0281	0.0002	0.0056	0.0655	0.0318	0.0506	0.0002	0.0002
P	0.0047	0.0284	0.0165	0.0283	0.0001	0.0142	0.0001	0.0165	0.0378	0.0001	0.0095	0.0402
S	0.0068	0.0164	0.0082	0.0301	0.015	0.0001	0.0001	0.026	0.0082	0.0274	0.0178	0.0205
Cl												
F												
Total	98.02	98.63	98.01	97.95	98.32	98.13	98.63	98.17	98.77	98.43	95.54	98.03

Mineral	hbl	hbl	hbl	hbl	hbl	hbl	hbl	hbl	hbl	hbl	hbl
Analysis No.	Lo39_cir12line1_9	Lo39_cir12line1_13	Lo39_cir12line1_14	Lo39_cir12line1_15	Lo39_cir13spot2	Lo39_cir14line1_4	Lo39_cir14line1_5	Lo39_cir14line1_7	Lo39_cir14spot1	Lo39_cir14spot2	Lo39_cir14spot3
Run ID	tm070909	tm070909	tm070909	tm070909	tm070909	tm070909	tm070909	tm070909	tm070909	tm070909	tm070909
SiO2	42.7073	43.7026	43.3752	43.3719	43.2232	43.0924	42.8397	43.5253	43.0354	43.0732	42.8036
TiO2	2.9075	3.1326	3.0134	3.0152	3.4169	3.0777	3.1439	3.1763	3.176	2.8845	3.1565
Al2O3	10.9967	10.2884	10.1811	10.1157	10.3502	10.4405	10.4753	10.651	10.418	10.9465	10.4665
Cr2O3											
FeO	12.5298	12.405	12.2356	12.2186	12.1429	12.1922	12.3596	12.1782	12.2392	12.4383	12.3682
MnO	0.381	0.4162	0.3905	0.3776	0.374	0.3518	0.3813	0.4294	0.3868	0.3425	0.3259
MgO	14.1908	14.4277	14.2842	14.4213	14.0801	14.3647	14.3217	14.3391	14.1262	14.0887	14.1862
ZnO	0.0803	0.0654	0.0476	0.0002	0.1458	0.0002	0.0536	0.0002	0.0002	0.0416	0.0002
CaO	10.9733	11.2335	11.2661	11.2185	11.2188	11.2339	11.2413	11.1631	11.2721	11.3963	11.2266
Na2O	2.4374	2.3737	2.3136	2.2386	2.2372	2.3318	2.4334	2.4132	2.4351	2.3465	2.396
K2O	0.8408	0.7919	0.7781	0.8602	0.9115	0.8269	0.8343	0.8431	0.8515	0.7706	0.8421
NiO	0.0002	0.0002	0.0002	0.0094	0.0002	0.0002	0.0281	0.0862	0.0002	0.0002	0.0599
P	0.0001	0.0047	0.0213	0.0001	0.0189	0.0189	0.0001	0.0118	0.0118	0.0047	0.0001
S	0.0109	0.0027	0.0014	0.0232	0.0164	0.0001	0.0342	0.0068	0.015	0.0246	0.026
Cl											
F											
Total	98.06	98.84	97.91	97.87	98.14	97.93	98.15	98.82	97.97	98.36	97.86

Mineral	hbl	hbl	hbl
Analysis No.	Lo54_cir5spot1	Lo54_cir5spot2	Lo54_cir5spot3
Run ID	tm070909	tm070909	tm070909
SiO2	42.6483	42.2758	41.4038
TiO2	3.483	3.4215	3.2812
Al2O3	11.0936	11.1697	10.7734
Cr2O3			
FeO	11.7686	11.7537	11.5644
MnO	0.2634	0.2672	0.2488
MgO	14.3583	14.2551	14.1211
ZnO	0.1279	0.0002	0.0744
CaO	11.4762	11.3458	11.2254
Na2O	2.4445	2.3732	2.4032
K2O	0.8436	0.7577	0.8016
NiO	0.0002	0.0206	0.0037
P	0.0071	0.0213	0.0307
S	0.015	0.0301	0.0369
Cl			
F			
Total	98.53	97.69	95.97

Mineral	mag	mag	mag	mag	mag	mag	mag	mag	mag	mag	mag	mag
Analysis No.	LO18 c3 pt12	LO52_C6point1	LO52_C6line3_2	LO52_C6line3_3	LO52_C6line3_4	LO52_C6line3_5	LO52_C6line3_6	LO52_C6line3_7	LO52_C6line3_8	LO52_C6line3_9	LO52_C10point1	LO52_C10point2MI
Run ID	tm010509	tm130709	tm130709	tm130709	tm130709	tm130709	tm130709	tm130709	tm130709	tm130709	tm130709	tm130709
SiO2	0.0563	0.0561	0.0674	0.0421	0.0309	0.1226	0.0983	0.0534	0.0795	0.0721	0.0646	0.0982
TiO2	9.2773	9.4316	9.4172	9.3441	9.3611	9.3557	9.3224	9.2334	9.3308	9.1399	9.0502	8.7686
Al2O3	2.9699	2.9904	3.0853	2.9981	3.0293	3.0641	3.0221	3.1188	2.9878	2.9867	2.9649	2.9272
Cr2O3	0.0412											
FeO	78.9122	79.1483	78.6512	79.1221	79.1553	79.2966	79.3911	78.314	78.9607	78.3583	78.1345	77.2308
MnO	0.8226	0.8009	0.7368	0.7364	0.8336	0.8359	0.7338	0.765	0.807	0.7679	0.813	0.7216
MgO	2.5708	2.57	2.569	2.5095	2.5054	2.63	2.6263	2.6989	2.5659	2.6473	2.5198	2.4536
ZnO	0.0954											
CaO	0.009	0.0304	0.0078	0.0243	0.0043	0.0001	0.007	0.0096	0.0001	0.0357	0.0374	0.0747
Na2O	0.0005	0.0005	0.0445	0.0666	0.0005	0.0157	0.0326	0.0004	0.0005	0.0338	0.0005	0.0005
K2O	0.0001	0.0289	0.0001	0.0001	0.0125	0.008	0.0052	0.0001	0.0001	0.0028	0.0177	0.0001
NiO	0.00	0.0001	0.0001	0.0219	0.0067	0.0539	0.0001	0.0286	0.0001	0.0001	0.0001	0.0051
P		0.0003	0.0125	0.0167	0.0375	0.0584	0.0292	0.0003	0.0003	0.0292	0.0003	0.0003
S												
Cl												
F												
Total	94.76	95.06	94.59	94.88	94.98	95.44	95.27	94.22	94.73	94.07	93.60	92.28

Mineral	mag	mag	mag	mag	mag	mag	mag	mag	mag	mag	mag
Analysis No.	LO52_C10point3	LO52_C10point4	LO52_C11line2_2	LO52_C11line2_3	LO52_C11line2_4	LO52_C11line2_5	LO52_C11line2_6	LO52_C11line2_7	LO52_C11line2_8	LO52_C12point2	LO52_C1_point1M1
Run ID	tm130709	tm130709	tm130709	tm130709	tm130709	tm130709	tm130709	tm130709	tm130709	tm130709	tm130709
SiO2	0.1094	0.113	0.129	0.0935	0.057	0.1075	0.1122	0.0393	0.0766	0.0785	1.5476
TiO2	9.0585	9.5459	8.7795	8.9173	9.0931	9.0758	9.0506	8.9742	8.9784	9.4209	9.0488
Al2O3	2.9984	2.8101	2.9215	2.9767	3.0416	2.9906	3.1129	2.9987	3.0259	3.0865	3.0132
Cr2O3											
FeO	77.9585	78.1559	76.1178	78.1312	76.7746	77.8848	76.3335	78.0509	76.9669	79.2282	74.5198
MnO	0.7376	0.8272	0.7887	0.7992	0.8003	0.7981	0.7814	0.8185	0.8249	0.7922	0.8773
MgO	2.5446	2.3802	2.4156	2.295	2.339	2.3316	2.4006	2.2824	2.3624	2.5382	2.88
ZnO											
CaO	0.04	0.0825	0.0001	0.0001	0.0061	0.0001	0.0374	0.0495	0.0408	0.0069	0.7336
Na2O	0.0005	0.0005	0.0005	0.0005	0.0005	0.0107	0.0004	0.0005	0.0127	0.0004	0.0487
K2O	0.008	0.0076	0.0229	0.0001	0.0001	0.0124	0.0044	0.0056	0.0225	0.0052	0.0705
NiO	0.0001	0.0001	0.0001	0.0034	0.0236	0.0219	0.1044	0.0001	0.0522	0.0001	0.0152
P	0.0003	0.0042	0.0003	0.0208	0.0003	0.0374	0.0003	0.0003	0.0374	0.025	0.0125
S											
Cl											
F											
Total	93.46	93.93	91.18	93.24	92.14	93.27	91.94	93.22	92.40	95.18	92.77

Mineral	mag	mag	mag	mag	mag	mag	mag	mag	mag	mag
Analysis No.	LO52_C3_line4_2	LO52_C3_line4_3	LO52_C3_line4_4	LO52_C3_line4_5	LO52_C3_line4_6	LO52_C3_line4_7	Lo39MGM_cirspot1	Lo39MGM_cir2spot4MI	Lo39MGM_cir3spot1	Lo39MGM_cir3spot4
Run ID	tm130709	tm130709	tm130709	tm130709	tm130709	tm130709	tm070909	tm070909	tm070909	tm070909
SiO2	0.0672	0.1073	0.069	0.069	0.098	0.0961	0.0666	0.1281	0.1034	0.1242
TiO2	9.6712	9.6172	9.7883	9.7911	9.5948	9.2183	8.8329	8.8556	9.2774	9.2436
Al2O3	2.9046	2.7574	2.7597	2.7562	2.8506	2.9066	2.5841	2.6927	2.9489	2.9441
Cr2O3										
FeO	78.6866	78.532	78.1397	78.8186	78.9223	77.9969	73.7385	78.872	78.8884	78.8411
MnO	0.8452	0.8717	0.8605	0.7702	0.9046	0.893	0.8414	0.6991	0.8075	0.7754
MgO	2.4015	2.4581	2.4133	2.5499	2.4713	2.5356	2.286	2.2913	2.5966	2.4373
ZnO							0.0717	0.0797	0.1011	0.1808
CaO	0.0521	0.0001	0.0035	0.0312	0.0061	0.0001	0.0978	0.0393	0.0227	0.0166
Na2O	0.0239	0.0473	0.0055	0.0024	0.0005	0.0431	0.0005	0.0005	0.0054	0.0231
K2O	0.0001	0.0001	0.0001	0.0001	0.0108	0.0257	0.0065	0.0121	0.0001	0.0097
NiO	0.0488	0.0001	0.0286	0.0084	0.0001	0.0001	0.0001	0.0136	0.0001	0.0222
P	0.0003	0.0003	0.0042	0.0003	0.0416	0.0003	0.0041	0.0021	0.0001	0.0001
S							0.0001	0.0132	0.0001	0.0001
Cl										
F										
Total	94.70	94.39	94.07	94.80	94.90	93.72	88.53	93.70	94.75	94.62

Mineral	mag	mag	mag	mag	mag	mag	mag	mag	mag
Analysis No.	Lo39MGM_cir3line1_1	Lo39MGM_cir3line1_2	Lo39MGM_cir3line1_3	Lo39MGM_cir3line1_7	Lo39MGM_cir3line1_8	Lo39MGM_cir3line1_9	Lo39MGM_cir3line1_10	Lo39MGM_cir3line1_11	Lo39MGM_cir3line1_12
Run ID	tm070909	tm070909	tm070909	tm070909	tm070909	tm070909	tm070909	tm070909	tm070909
SiO2	0.0762	0.2666	0.0805	0.09	0.0823	0.1185	0.0729	0.0667	0.0791
TiO2	9.0971	8.8426	9.0826	8.9472	9.0169	9.0608	9.004	9.0125	8.9645
Al2O3	2.9397	2.9706	2.987	3.0347	2.9251	2.8485	3.0697	2.9255	2.817
Cr2O3									
FeO	77.5768	77.8824	76.4823	78.0365	77.7917	78.7165	79.615	78.6568	78.8647
MnO	0.7612	0.8226	0.8483	0.7816	0.7354	0.7987	0.7817	0.7308	0.7484
MgO	2.3805	2.4325	2.495	2.5098	2.4204	2.4311	2.5494	2.4387	2.4972
ZnO	0.1515	0.1356	0.1037	0.0638	0.0505	0.0001	0.0505	0.1037	0.1117
CaO	0.0175	0.0001	0.0001	0.0001	0.0001	0.007	0.0001	0.0035	0.0184
Na2O	0.0005	0.0297	0.0004	0.0124	0.0005	0.0358	0.0032	0.0005	0.0005
K2O	0.0211	0.0559	0.0001	0.0001	0.0057	0.0001	0.0332	0.0001	0.0001
NiO	0.0001	0.0001	0.0392	0.0273	0.0392	0.0153	0.0001	0.0001	0.0392
P	0.0021	0.0001	0.0001	0.0186	0.0103	0.0041	0.0001	0.0001	0.0001
S	0.0001	0.0001	0.0204	0.0001	0.0156	0.0001	0.0001	0.0001	0.006
Cl									
F									
Total	93.02	93.44	92.14	93.52	93.09	94.04	95.18	93.94	94.15

Mineral	mag	mag	mag	mag	mag	mag	mag	mag	mag
Analysis No.	Lo39MGM_cir3line1_13	Lo39MGM_cir3line1_14	Lo39MGM_cir3line1_15	Lo39MGM_cir4spot4	Lo39MGM_cir5spot1	Lo39MGM_cir6spot1	Lo39MGM_cir7spot1	Lo39MGM_cir8spot2	Lo39MGM_cir9spot1
Run ID	tm070909	tm070909	tm070909	tm070909	tm070909	tm070909	tm070909	tm070909	tm070909
SiO2	0.0833	0.0039	0.1062	0.0571	0.0824	0.079	0.1086	0.0872	0.1157
TiO2	9.0672	0.312	8.9259	9.5162	9.1178	9.6117	9.2273	9.0768	9.7196
Al2O3	2.9811	0.0053	2.965	2.6966	2.8566	2.6212	2.9594	3.0562	2.6714
Cr2O3									
FeO	78.5442	78.9688	78.7029	80.4216	79.5334	78.44	78.6243	78.6963	79.2432
MnO	0.7578	0.07	0.7449	0.8192	0.824	0.9482	0.7331	0.7	0.933
MgO	2.4723	0.0003	2.3916	2.2243	2.3689	2.3013	2.4005	2.4729	2.3368
ZnO	0.0824	0.0295	0.0877	0.0585	0.0771	0.0931	0.1223	0.1224	0.0878
CaO	0.0001	0.0009	0.0001	0.0035	0.0236	0.0061	0.0201	0.0376	0.0052
Na2O	0.0005	0.0275	0.0005	0.0251	0.0005	0.0219	0.0075	0.0004	0.0164
K2O	0.0001	0.0001	0.0016	0.0032	0.0138	0.0032	0.017	0.0001	0.0001
NiO	0.0307	0.0344	0.0324	0.0392	0.0375	0.0001	0.0273	0.0001	0.0137
P	0.0001	0.0001	0.0001	0.0001	0.0062	0.0041	0.0083	0.0001	0.0001
S	0.0001	40.1928	0.0024	0.0144	0.0096	0.0001	0.0001	0.0001	0.0084
Cl									
F									
Total	94.02	119.65	93.96	95.88	94.95	94.13	94.26	94.25	95.15

Mineral	mag	mag	mag	mag	mag	mag	mag	mag	mag
Analysis No.	Lo39MGM_cir10spot1	Lo39MGM_cir12spot1	Lo39MGM_cir12spot3	Lo39MGM_cir13spot1	Lo39MGM_cir13spot4	Lo39MGM_cir14spot3	Lo54PGM_cir6spot1	Lo39PGM_cir3spot2	Lo54MGM_cir1spot1
Run ID	tm070909	tm070909	tm070909	tm070909	tm070909	tm070909	tm070909	tm070909	tm070909
SiO2	0.0971	0.1864	0.0915	0.1111	0.1235	0.0768	0.0736	0.1136	0.1326
TiO2	9.5533	9.3038	9.2618	9.3661	9.1289	9.1675	13.2746	9.2654	12.7491
Al2O3	2.699	2.9621	2.8946	3.0427	3.0153	2.9495	2.6301	2.8373	2.6819
Cr2O3									
FeO	79.7734	79.6275	79.4587	79.0081	80.0624	79.4625	77.0794	80.2646	77.2198
MnO	0.9193	0.7971	0.7954	0.6963	0.7843	0.729	0.8919	0.861	0.8673
MgO	2.2688	2.4757	2.5007	2.5052	2.6167	2.5763	2.8685	2.4748	2.7456
ZnO	0.1755	0.1092	0.0001	0.1518	0.1172	0.0373	0.1709	0.1599	0.0774
CaO	0.0001	0.0001	0.0621	0.0123	0.0061	0.0219	0.0061	0.0149	0.0298
Na2O	0.0255	0.0123	0.0209	0.0503	0.0004	0.0005	0.0094	0.0005	0.0028
K2O	0.0001	0.0001	0.0097	0.017	0.0057	0.0001	0.0081	0.0001	0.0041
NiO	0.0904	0.0051	0.0307	0.0239	0.0785	0.0034	0.0086	0.0034	0.0325
P	0.0001	0.0001	0.0001	0.0041	0.0352	0.0062	0.0001	0.0001	0.0001
S	0.0001	0.0096	0.0001	0.006	0.0156	0.006	0.0096	0.0001	0.0084
Cl									
F									
Total	95.60	95.49	95.13	94.99	95.99	95.04	97.03	96.00	96.55

Mineral	mag	mag	mag	mag	mag	mag	mag	mag	mag	mag
Analysis No.	Lo54MGM_cir2spot1	Lo54MGM_cir3spot1	Lo54MGM_cir3spot6	Lo54MGM_cir4spot1	Lo54MGM_cir4spot4	Lo54MGM_cir7spot1	Lo54MGM_cir7spot2	Lo54MGM_cir9spot1	Lo54MGM_cir10spot1	Lo54MGM_cir10spot3
Run ID	tm070909	tm070909	tm070909	tm070909	tm070909	tm070909	tm070909	tm070909	tm070909	tm070909
SiO2	0.1036	0.1221	0.106	0.1089	0.1461	0.1063	0.1255	0.3161	0.1173	0.0844
TiO2	12.9124	13.041	12.9346	10.2571	10.313	10.4087	10.2725	10.334	9.3127	9.2952
Al2O3	2.7224	2.64	2.7058	3.4781	3.3633	4.0148	4.128	0.637	4.0425	4.2249
Cr2O3										
FeO	76.2366	76.7372	76.7468	78.7236	78.8189	77.8608	77.9689	78.6696	79.4678	79.1759
MnO	0.8903	0.8353	0.6973	0.6897	0.8408	0.5376	0.5409	0.6481	0.615	0.4474
MgO	2.816	2.8557	2.7647	2.7344	2.7015	3.614	3.6949	0.0427	3.1722	3.656
ZnO	0.0588	0.1604	0.0855	0.1095	0.1202	0.1445	0.0001	0.0318	0.0001	0.0669
CaO	0.0499	0.2841	0.0263	0.0001	0.0588	0.0194	0.0001	0.0478	0.0317	0.0273
Na2O	0.0004	0.0004	0.0004	0.0283	0.0207	0.0258	0.0596	0.0074	0.0013	0.0179
K2O	0.0016	0.0138	0.0001	0.0024	0.0163	0.0236	0.0001	0.0113	0.0001	0.0196
NiO	0.0001	0.0325	0.0462	0.0342	0.0257	0.0326	0.0223	0.0001	0.0034	0.0001
P	0.0001	0.0103	0.0001	0.0021	0.0001	0.0001	0.0062	0.0062	0.0001	0.0208
S	0.0001	0.0001	0.0001	0.0145	0.0001	0.0001	0.0001	0.0107	0.006	0.0001
Cl										
F										
Total	95.79	96.73	96.11	96.18	96.43	96.79	96.82	90.76	96.77	97.04

Mineral	mag	mag	mag	mag	mag	mag	mag	mag	mag	mag
Analysis No.	Lo54MGM_cir11spot1	Lo39MGM_cir2spot1	Lo39_cir2spot6	Lo39_cir2spot9	Lo23PGM_cir6spot1	Lo23PGM_cir8spot1	Lo23MGM_cir1spot1	Lo23MGM_cir2Aspot1	Lo23MGM_cir3spot1	Lo23MGM_cir4spot1
Run ID	tm070909	tm070909	tm070909	tm070909	tm070909	tm070909	tm070909	tm070909	tm070909	tm070909
SiO2	0.0808	0.0995	0.1108	0.1117	0.0689	4.8165	0.1411	0.0765	0.1114	0.2209
TiO2	13.2417	9.3903	9.0709	9.188	9.4703	0.1135	9.3108	9.3701	9.2059	9.4507
Al2O3	2.54	3.0037	3.0328	3.0934	2.9677	5.1751	3.151	2.9588	2.9958	2.6773
Cr2O3										
FeO	76.7285	79.7299	79.1398	79.2595	80.3513	81.8506	80.1347	80.5349	80.5075	78.2788
MnO	0.9385	0.6998	0.7074	0.7538	0.7633	0.2148	0.7551	0.902	0.8434	0.8763
MgO	2.7781	2.5284	2.74	2.6186	2.7367	0.2169	2.7551	2.3649	2.3918	2.4495
ZnO	0.1042	0.101	0.1539	0.1755	0.1976	0.0804	0.1576	0.0908	0.2056	0.2778
CaO	0.0307	0.0455	0.0115	0.0115	0.0123	0.4715	0.0001	0.0001	0.0237	0.0676
Na2O	0.0213	0.0185	0.0079	0.0004	0.0223	0.7367	0.0294	0.0168	0.0008	0.0282
K2O	0.0001	0.0113	0.0001	0.0099	0.0203	0.0403	0.0001	0.0244	0.0138	0.0001
NiO	0.0531	0.0001	0.019	0.0173	0.0308	0.0309	0.0034	0.0001	0.0017	0.0428
P	0.0083	0.0062	0.0001	0.0231	0.0001	0.0001	0.0083	0.0001	0.0249	0.0415
S	0.0001	0.0001	0.0134	0.0098	0.0181	0.0073	0.0036	0.0001	0.0001	0.0036
Cl										
F										
Total	96.53	95.63	95.01	95.27	96.66	93.75	96.45	96.34	96.33	94.42

Mineral	mag	mag	mag	mag	mag	mag	mag	mag	mag
Analysis No.	Lo23MGM_cir5spot2	Lo23MGM_cir5line1_1	Lo23MGM_cir5line1_2	Lo23MGM_cir5line1_3	Lo23MGM_cir5line1_4	Lo23MGM_cir5line1_5	Lo23MGM_cir6spot2	Lo23MGM_cir8spot1	Lo23MGM_cir12spot1
Run ID	tm070909	tm070909	tm070909	tm070909	tm070909	tm070909	tm070909	tm070909	tm070909
SiO2	0.1051	0.1008	0.1127	0.1095	0.0875	0.1195	0.0522	0.112	0.1331
TiO2	9.9847	9.8942	9.7975	9.7783	9.873	9.6862	9.3748	9.3145	9.2252
Al2O3	2.6181	2.6409	2.5501	2.5805	2.7169	2.7236	2.871	3.0062	2.949
Cr2O3									
FeO	80.3064	80.2815	79.8353	80.0002	80.7859	79.9814	80.2461	79.6242	79.8694
MnO	0.9792	0.8955	0.9472	0.873	0.9635	0.843	0.8298	0.8004	0.8118
MgO	2.3876	2.3745	2.3519	2.3097	2.337	2.5182	2.2886	2.5945	2.4803
ZnO	0.0774	0.1389	0.024	0.1603	0.1095	0.1229	0.1469	0.0615	0.0588
CaO	0.014	0.0079	0.0097	0.0001	0.0035	0.072	0.0001	0.0001	0.0879
Na2O	0.0241	0.0005	0.0005	0.0019	0.0098	0.014	0.0222	0.0141	0.0031
K2O	0.0001	0.0001	0.0001	0.0001	0.0106	0.0366	0.0001	0.0106	0.0001
NiO	0.0001	0.0017	0.0001	0.0702	0.0001	0.0001	0.0445	0.0137	0.0017
P	0.0145	0.0001	0.0001	0.0001	0.0083	0.0001	0.0001	0.0042	0.0332
S	0.0012	0.0193	0.0001	0.0157	0.0157	0.0001	0.0096	0.0001	0.0001
Cl									
F									
Total	96.51	96.36	95.63	95.90	96.92	96.12	95.89	95.56	95.65

Mineral	mag	mag	mag	mag	mag	mag	mag	mag
Analysis No.	Lo23MGM_cir14spot1	Lo23MGM_cir14spot2	Lo23MGM_cir14line1_2	Lo23MGM_cir14line1_3	Lo23MGM_cir14line1_5	Lo23MGM_cir14line1_6	Lo39_cir12spot1	Lo39_cir13spot6
Run ID	tm070909	tm070909	tm070909	tm070909	tm070909	tm070909	tm070909	tm070909
SiO2	0.0901	0.1102	0.0465	0.0603	0.0968	0.1074	0.0819	0.1414
TiO2	9.3998	9.5028	9.274	9.5986	9.3475	9.3198	9.4375	9.4796
Al2O3	3.0285	3.0602	3.028	3.0178	3.0142	3.0371	2.9583	2.5915
Cr2O3								
FeO	80.995	79.9627	80.2615	79.9491	79.7721	80.1533	79.4848	79.6061
MnO	0.7278	0.8217	0.78	0.7727	0.7581	0.7522	0.7766	0.9095
MgO	2.657	2.5986	2.6393	2.7045	2.6466	2.7347	2.5765	2.543
ZnO	0.1471	0.1231	0.1952	0.0401	0.0455	0.0482	0.1759	0.2705
CaO	0.0501	0.0001	0.0001	0.0062	0.0343	0.059	0.0001	0.0382
Na2O	0.0235	0.0004	0.0113	0.0284	0.0004	0.0295	0.0004	0.0063
K2O	0.0041	0.0187	0.0001	0.009	0.0001	0.0001	0.0132	0.0016
NiO	0.0001	0.0069	0.0001	0.0001	0.0001	0.012	0.0902	0.0728
P	0.0021	0.0187	0.0187	0.0021	0.0001	0.0001	0.0001	0.0001
S	0.0048	0.0001	0.0338	0.006	0.0072	0.0012	0.0001	0.0098
Cl								
F								
Total	97.13	96.22	96.29	96.19	95.72	96.25	95.60	95.67

Mineral	opx	opx	opx	opx	opx	opx	opx	opx	opx	opx	opx
Analysis No.	LO18 c1 pt2	LO18 c1 pt3	LO52_C10point5	LO52_C3_line2_3	LO52_C3_line2_4	LO52_C3_line2_5	LO52_C3_line2_6	LO52_C3_line2_7	Lo39MGM_cir1spot2	Lo39MGM_cir2spot2	Lo39MGM_cir2spot3
Run ID	tm010509	tm010509	tm130709	tm130709	tm130709	tm130709	tm130709	tm130709	tm070909	tm070909	tm070909
SiO2	55.6873	55.28	54.1155	54.1329	54.2413	53.3146	53.4459	52.5684	52.9478	52.9109	52.9051
TiO2	0.2137	0.1732	0.2409	0.2327	0.205	0.2624	0.415	0.2491	0.2427	0.2942	0.2441
Al2O3	0.7329	0.5969	0.7611	1.0261	0.92	1.2722	1.2444	1.0291	0.668	1.1847	1.1763
Cr2O3	0.0002	0.0024									
FeO	17.9547	18.0435	17.5774	18.0822	18.0565	18.466	18.0319	17.6557	17.5797	19.9664	20.2039
MnO	1.2932	1.5595	1.2054	1.296	1.3504	1.1988	1.2744	1.1159	1.2173	0.9626	1.0266
MgO	25.2125	25.0645	25.3724	25.5535	25.4597	25.4357	25.3625	25.0198	25.1229	23.6473	23.5313
ZnO	0.0427	0.164							0.085	0.1286	0.0468
CaO	1.2607	1.2451	1.3343	1.33	1.2353	1.3899	1.3333	1.264	1.2489	1.5262	1.3652
Na2O	0.0126	0.0335	0.0295	0.0059	0.0357	0.0407	0.0412	0.0345	0.0393	0.0408	0.0292
K2O	0.0001	0.0235	0.0151	0.0091	0.0027	0.0091	0.0155	0.016	0.0092	0.0001	0.0074
NiO	0.00	0.00	0.031	0.0002	0.0328	0.0055	0.0036	0.0765	0.0002	0.0442	0.0276
P			0.0003	0.0097	0.0048	0.0434	0.0338	0.0003	0.0001	0.0001	0.0143
S									0.0001	0.0178	0.0001
Cl											
F											
Total	102.41	102.19	100.68	101.68	101.54	101.44	101.20	99.03	99.16	100.72	100.58

Mineral	opx	opx	opx	opx	opx	opx	opx	opx	opx
Analysis No.	Lo39MGM_cir4spot1	Lo39MGM_cir4spot2	Lo39MGM_cir4spot3	Lo39MGM_cir6spot2	Lo39MGM_cir6spot4	Lo39MGM_cir6spot6	Lo39MGM_cir6line1_1	Lo39MGM_cir6line1_2	Lo39MGM_cir6line1_3
Run ID	tm070909	tm070909	tm070909	tm070909	tm070909	tm070909	tm070909	tm070909	tm070909
SiO2	53.4358	52.716	52.3538	53.6209	52.9247	52.9425	53.4086	53.4833	53.0365
TiO2	0.1956	0.2558	0.2664	0.226	0.1578	0.1924	0.1837	0.1991	0.17
Al2O3	0.881	0.8101	0.9118	0.7013	0.8123	0.7149	0.8026	0.6448	0.6161
Cr2O3									
FeO	18.4079	18.8559	19.3381	18.3596	18.7058	18.4586	17.8726	18.179	18.2612
MnO	1.3258	1.0691	1.0178	1.2697	1.2061	1.3372	1.1479	1.2937	1.2169
MgO	24.9436	24.1563	24.1778	24.8526	24.2013	24.3306	24.8279	25.1034	25.0673
ZnO	0.041	0.1377	0.0556	0.0938	0.0002	0.0938	0.0645	0.0528	0.17
CaO	1.1948	1.2473	1.3523	1.2817	1.2588	1.2215	1.1422	1.3053	1.2539
Na2O	0.0157	0.0365	0.0206	0.0172	0.021	0.0644	0.0142	0.0082	0.0517
K2O	0.0055	0.0138	0.0147	0.0083	0.0175	0.0001	0.0083	0.0055	0.0001
NiO	0.0387	0.0002	0.0002	0.0498	0.0002	0.0002	0.0535	0.0002	0.0148
P	0.0001	0.0072	0.0096	0.0001	0.0048	0.0168	0.0336	0.0096	0.0168
S	0.0041	0.0028	0.0001	0.0001	0.0028	0.0165	0.0001	0.0001	0.0001
Cl									
F									
Total	100.49	99.31	99.52	100.48	99.31	99.39	99.56	100.29	99.88

Mineral	opx	opx	opx	opx	opx	opx	opx	opx	opx
Analysis No.	Lo39MGM_cir6line1_4	Lo39MGM_cir6line1_5	Lo39MGM_cir6line1_6	Lo39MGM_cir6line1_7	Lo39MGM_cir6line1_8	Lo39MGM_cir6line1_9	Lo39MGM_cir6line1_10	Lo39MGM_cir8spot1	Lo39MGM_cir8spot3
Run ID	tm070909	tm070909	tm070909	tm070909	tm070909	tm070909	tm070909	tm070909	tm070909
SiO2	53.0946	52.2526	52.5486	52.1413	53.2918	53.0357	52.9061	53.4739	53.1844
TiO2	0.255	0.3522	0.2657	0.2527	0.2246	0.1976	0.2075	0.2722	0.2955
Al2O3	0.929	1.6302	1.3999	1.3097	0.6663	0.566	0.7488	1.4466	1.384
Cr2O3									
FeO	17.8052	18.0548	18.3762	17.3577	18.4426	18.2013	17.8079	17.693	17.8005
MnO	1.2163	1.1858	0.9904	1.1758	1.3985	1.2782	1.1857	1.0003	0.8927
MgO	24.7985	23.9857	24.4224	24.2667	24.7968	24.759	25.1166	25.1542	25.3637
ZnO	0.0176	0.041	0.126	0.1262	0.0469	0.0234	0.0264	0.0264	0.0382
CaO	1.2528	2.0144	1.289	1.2617	1.3204	1.2912	1.1954	1.423	1.36
Na2O	0.0342	0.0241	0.0111	0.0367	0.0164	0.0157	0.018	0.0307	0.026
K2O	0.0185	0.0175	0.0001	0.0407	0.0001	0.0001	0.0001	0.0037	0.0315
NiO	0.0462	0.0002	0.1107	0.0166	0.0517	0.0406	0.0702	0.0129	0.0111
P	0.0001	0.0167	0.024	0.0001	0.0192	0.0144	0.0072	0.0001	0.0001
S	0.0001	0.0055	0.0001	0.0001	0.0028	0.0151	0.0138	0.0138	0.0001
Cl									
F									
Total	99.47	99.58	99.56	97.99	100.28	99.44	99.30	100.55	100.39

Mineral	opx	opx	opx	opx	opx	opx	opx	opx	opx
Analysis No.	Lo39MGM_cir9spot2	Lo39MGM_cir9spot4	Lo39MGM_cir13spot2	Lo39MGM_cir13spot3	Lo39PGM_cir5spot6MI	Lo54MGM_cir7spot3	Lo23MGM_cir1spot2	Lo23MGM_cir2Aspot2	Lo23MGM_cir3line1_2
Run ID	tm070909	tm070909	tm070909	tm070909	tm070909	tm070909	tm070909	tm070909	tm070909
SiO2	52.6385	52.7629	53.2298	53.4229	54.2791	54.5662	53.356	54.6529	54.9523
TiO2	0.2637	0.2342	0.2109	0.2181	0.2165	0.2982	0.3125	0.2657	0.2819
Al2O3	1.0231	0.8934	0.7286	0.7831	0.7206	1.4359	0.883	0.9501	0.7334
Cr2O3									
FeO	18.6258	18.4686	19.4615	19.37	17.7851	16.3	19.7945	18.3466	18.2504
MnO	1.1021	1.2026	1.2292	1.1919	1.2687	0.6914	1.0939	1.3602	1.2991
MgO	24.2905	24.0981	24.0838	24.4553	25.6582	27.9367	24.8623	25.8063	26.1008
ZnO	0.0645	0.0059	0.041	0.0909	0.1059	0.0767	0.0002	0.0002	0.0972
CaO	1.4872	1.2347	1.3492	1.5026	1.2678	1.3586	1.5673	1.2729	1.3421
Na2O	0.0227	0.0506	0.063	0.0485	0.0222	0.0196	0.044	0.0213	0.0331
K2O	0.012	0.0001	0.0001	0.0018	0.0001	0.04	0.0001	0.0148	0.0028
NiO	0.0002	0.0646	0.0002	0.0002	0.0002	0.0037	0.0019	0.0002	0.0002
P	0.0048	0.0001	0.0048	0.0001	0.012	0.029	0.012	0.0168	0.0265
S	0.0001	0.0001	0.011	0.0001	0.0001	0.0028	0.0001	0.0001	0.0042
Cl									
F									
Total	99.54	99.02	100.41	101.09	101.34	102.76	101.93	102.71	103.12

Mineral	opx	opx	opx	opx	opx	opx	opx	opx	opx
Analysis No.	Lo23MGM_cir3line1_3	Lo23MGM_cir3line1_4	Lo23MGM_cir4spot2	Lo23MGM_cir4spot3	Lo23MGM_cir4spot4	Lo23MGM_cir6spot1	Lo23MGM_cir6spot4	Lo23MGM_cir14spot3	Lo23MGM_cir14spot4
Run ID	tm070909	tm070909	tm070909	tm070909	tm070909	tm070909	tm070909	tm070909	tm070909
SiO2	55.0164	54.8442	54.5793	36.7614	30.6649	54.7482	54.1066	54.1483	46.4688
TiO2	0.2389	0.2414	0.2296	0.2099	4.5472	0.1973	0.2418	0.2848	0.2765
Al2O3	0.775	0.8126	0.8837	2.2265	1.4543	0.8202	0.7846	1.2821	0.9328
Cr2O3									
FeO	18.0451	18.0196	18.6087	16.1098	49.0189	18.6664	16.4266	17.8997	16.6739
MnO	1.318	1.2417	1.2538	0.9456	1.1075	1.3962	1.1974	0.8593	1.1525
MgO	25.899	26.1112	25.3725	25.2957	19.243	25.95	26.8418	26.6563	22.0453
ZnO	0.1473	0.0854	0.0002	0.0999	0.0002	0.0294	0.0266	0.0089	0.0471
CaO	1.2621	1.3193	1.1912	0.7492	0.6112	1.3155	1.3207	1.2991	1.1371
Na2O	0.0314	0.0227	0.024	0.0657	0.0026	0.0235	0.0352	0.036	0.0681
K2O	0.0251	0.0037	0.0083	0.0001	0.0001	0.0001	0.0047	0.0158	0.0056
NiO	0.0002	0.0593	0.0019	0.0002	0.0449	0.0111	0.0297	0.0002	0.0002
P	0.0001	0.0001	0.0001	0.012	0.0068	0.0048	0.0121	0.0001	0.0048
S	0.0001	0.0001	0.0001	0.0014	0.0001	0.0028	0.0001	0.0264	0.0028
Cl									
F									
Total	102.76	102.76	102.15	82.48	106.70	103.17	101.03	102.52	88.82

Mineral	opx	opx	opx	opx	opx	opx	opx	opx	opx
Analysis No.	Lo23MGM_cir14line1_4	Lo23MGM_cir14line1_7	Lo23MGM_cir14line1_8	Lo23MGM_cir14line1_9	Lo23MGM_cir14line1_10	Lo39_cir12line1_10	Lo39_cir12line1_11	Lo39_cir12line1_12	Lo39_cir13spot4
Run ID	tm070909	tm070909	tm070909	tm070909	tm070909	tm070909	tm070909	tm070909	tm070909
SiO2	55.1829	51.8888	53.7631	54.662	54.4214	54.3646	54.444	54.2333	54.361
TiO2	0.2275	0.3137	0.3707	0.3527	0.2867	0.2493	0.2212	0.195	0.1954
Al2O3	0.7001	1.4814	2.2497	1.3532	1.6401	0.8147	0.766	0.7982	0.7269
Cr2O3									
FeO	18.4198	15.7073	18.0464	17.7824	17.9861	17.9063	17.7323	17.6969	18.0529
MnO	1.1838	1.1212	0.9313	1.0655	1.0002	1.2097	1.1343	1.1985	1.3656
MgO	26.0842	25.2015	25.8267	26.2606	26.3481	25.7314	25.5656	25.5395	25.2459
ZnO	0.0002	0.1477	0.0002	0.0649	0.0472	0.0239	0.0926	0.0002	0.0567
CaO	1.3251	1.3144	1.5699	1.3707	1.465	1.3243	1.3415	1.3149	1.3229
Na2O	0.0464	0.0273	0.0436	0.046	0.038	0.0213	0.0373	0.0003	0.027
K2O	0.0065	0.0001	0.0102	0.0001	0.0001	0.0113	0.0263	0.0001	0.0038
NiO	0.0019	0.039	0.0002	0.0074	0.0002	0.0188	0.0319	0.0002	0.0002
P	0.0217	0.0121	0.0001	0.0048	0.0072	0.0001	0.0024	0.0001	0.0073
S	0.0001	0.0001	0.0055	0.0001	0.0166	0.0056	0.007	0.0001	0.0001
Cl									
F									
Total	103.20	97.25	102.82	102.97	103.26	101.68	101.40	100.98	101.37

Mineral	opx
Analysis No.	Lo39_cir13spot5
Run ID	tm070909
SiO2	54.0328
TiO2	0.2202
Al2O3	0.7386
Cr2O3	
FeO	18.1968
MnO	1.2993
MgO	25.4288
ZnO	0.0865
CaO	1.2385
Na2O	0.0447
K2O	0.0169
NiO	0.0338
P	0.0001
S	0.0001
Cl	
F	
Total	101.34

Mineral	cpx	cpx	cpx	cpx	cpx	cpx	cpx	cpx	cpx	cpx
Analysis No.	Lo39MGM_cir3spot2	Lo39MGM_cir3spot3	Lo39MGM_cir3line1_4	Lo39MGM_cir3line1_5	Lo39MGM_cir5spot2	Lo39MGM_cir7spot2	Lo39MGM_cir12spot2	Lo39MGM_cir14spot1	Lo39MGM_cir14spot2	Lo54MGM_cir9spot2
Run ID	tm070909	tm070909	tm070909	tm070909	tm070909	tm070909	tm070909	tm070909	tm070909	tm070909
SiO2	52.1975	52.1558	51.2661	51.0094	50.821	50.3099	50.8642	52.2925	51.51	51.6526
TiO2	0.3914	0.3728	0.4527	0.4829	0.4044	0.6716	0.3733	0.4227	0.4988	0.5108
Al2O3	1.3319	1.247	1.7123	1.5842	2.3253	3.2926	1.1865	1.5104	1.9782	2.5818
Cr2O3										
FeO	9.3571	8.7853	9.2543	9.035	8.5825	8.8909	10.2471	9.5941	9.9412	8.5775
MnO	0.7256	0.6956	0.644	0.5949	0.5718	0.579	0.5886	0.5149	0.4326	0.3758
MgO	15.2277	15.3565	15.042	14.6848	14.719	14.1443	14.4207	14.9808	14.7671	15.7978
ZnO	0.0586	0.0587	0.0002	0.0002	0.0822	0.0793	0.1701	0.0002	0.047	0.1149
CaO	20.7398	20.656	20.3958	20.6196	20.8277	21.1662	20.5773	20.9376	20.6996	21.4711
Na2O	0.3347	0.3817	0.3821	0.3882	0.4216	0.3967	0.3916	0.3288	0.4087	0.337
K2O	0.0197	0.0001	0.0001	0.044	0.0117	0.0036	0.017	0.0045	0.0117	0.0072
NiO	0.0002	0.0148	0.0002	0.0018	0.0002	0.0166	0.0002	0.0002	0.0314	0.0278
P	0.0115	0.0301	0.0001	0.0138	0.0001	0.0001	0.0001	0.0139	0.0046	0.0116
S	0.0053	0.0001	0.0001	0.0001	0.0001	0.0094	0.0001	0.0001	0.008	0.0013
Cl										
F										
Total	100.40	99.75	99.15	98.46	98.77	99.56	98.84	100.60	100.34	101.47

Mineral	cpx	cpx	cpx	cpx	cpx	cpx	cpx	cpx	cpx	cpx	cpx
Analysis No.	Lo54MGM_cir9spot4	Lo23MGM_cir7spot1	Lo23MGM_cir7spot2	Lo23MGM_cir7spot4	Lo39_cir2spot4	Lo39_cir2spot5	Lo39_cir2spot10	Lo39_cir2spot11	Lo39_cir2spot12	Lo39_cir2line1_2	Lo39_cir2line1_3
Run ID	tm070909	tm070909	tm070909	tm070909	tm070909	tm070909	tm070909	tm070909	tm070909	tm070909	tm070909
SiO2	49.3927	52.8656	54.7288	44.2488	51.3849	50.7733	52.7866	50.9984	50.7065	52.7299	52.5546
TiO2	1.1032	0.4772	0.4675	1.7661	0.5984	0.775	0.4309	0.6801	0.8002	0.4236	0.4789
Al2O3	5.4306	1.4809	2.2178	2.2899	2.6264	3.5775	1.8619	3.6831	3.8365	1.643	1.719
Cr2O3											
FeO	8.9227	8.6715	8.1391	19.7204	8.805	8.536	8.4406	8.5557	8.2746	8.4712	8.4545
MnO	0.2747	0.65	0.4306	0.4052	0.5707	0.4078	0.5826	0.2633	0.2746	0.5474	0.5826
MgO	14.0823	15.5874	17.1633	14.5771	14.9899	14.589	15.6483	14.707	14.9238	15.6902	15.6958
ZnO	0.05	0.0118	0.0002	0.0002	0.0328	0.0625	0.0418	0.0119	0.0894	0.0388	0.0298
CaO	21.7682	20.9717	20.6516	18.2031	21.4101	21.5767	20.7948	21.4867	21.5752	20.9013	21.0339
Na2O	0.3593	0.3708	0.3253	0.2506	0.3919	0.3434	0.3942	0.3614	0.4081	0.3532	0.3813
K2O	0.0333	0.0199	0.0073	0.016	0.0209	0.0309	0.0073	0.0219	0.0009	0.0301	0.0246
NiO	0.0002	0.0002	0.0002	0.0002	0.0002	0.03	0.0638	0.0002	0.0563	0.0002	0.0263
P	0.0023	0.0023	0.0187	0.0001	0.007	0.0047	0.0001	0.0001	0.0117	0.0117	0.0117
S	0.004	0.0067	0.0027	0.0001	0.0001	0.0109	0.0001	0.0014	0.0163	0.0001	0.0109
Cl											
F											
Total	101.42	101.12	104.15	101.48	100.84	100.72	101.05	100.77	100.97	100.84	101.00

Mineral	cpx	cpx	cpx	cpx	cpx	cpx	cpx	cpx	cpx	cpx	cpx
Analysis No.	Lo39_cir2line1_4	Lo39_cir2line1_5	Lo39_cir2line1_6	Lo39_cir2line1_8	Lo39_cir2line1_9	Lo39_cir2line1_10	Lo39_cir2line1_15	Lo39_cir2line1_17	Lo39_cir2line1_18	Lo39_cir2line1_19	Lo39_cir2line1_20
Run ID	tm070909	tm070909	tm070909	tm070909	tm070909	tm070909	tm070909	tm070909	tm070909	tm070909	tm070909
SiO2	52.6787	52.7136	52.7325	50.3096	50.7352	50.7464	50.5525	50.6923	50.3021	50.1282	50.3447
TiO2	0.5457	0.4719	0.4369	0.8107	0.7576	0.7324	0.8027	0.7295	0.7612	0.7805	0.8176
Al2O3	1.7029	1.7851	1.8425	4.0163	3.8289	3.9269	3.642	3.8104	3.8216	3.9004	4.0621
Cr2O3											
FeO	8.404	8.2069	8.619	8.5681	8.4411	8.5758	8.4386	8.4778	8.2547	8.322	8.2761
MnO	0.4674	0.5328	0.6641	0.2801	0.2634	0.2801	0.3487	0.3007	0.2486	0.2525	0.2859
MgO	15.4656	15.5502	15.4078	14.4815	14.7329	14.8906	14.5772	14.8778	14.7422	14.7933	14.7566
ZnO	0.0894	0.0002	0.0089	0.003	0.0596	0.0002	0.0507	0.0268	0.0298	0.003	0.0002
CaO	21.2576	21.3239	21.273	21.6137	21.5963	21.4978	21.6757	21.7944	21.6571	21.6781	21.4961
Na2O	0.411	0.3481	0.4056	0.377	0.4031	0.3466	0.4034	0.378	0.3564	0.3539	0.371
K2O	0.0055	0.01	0.0009	0.0373	0.0364	0.0009	0.0091	0.02	0.0001	0.0118	0.0274
NiO	0.0002	0.0002	0.0002	0.0002	0.0188	0.0056	0.0002	0.0451	0.0525	0.0002	0.0244
P	0.007	0.0094	0.007	0.0094	0.0001	0.0187	0.0281	0.0187	0.0001	0.0187	0.0094
S	0.0027	0.0136	0.0109	0.0109	0.0001	0.0122	0.0163	0.0027	0.0001	0.0001	0.0109
Cl											
F											
Total	101.04	100.97	101.41	100.52	100.87	101.03	100.55	101.17	100.23	100.24	100.48

Mineral	cpx	cpx
Analysis No.	Lo39_cir2line1_21	Lo39_cir2line1_22
Run ID	tm070909	tm070909
SiO2	50.4989	50.4174
TiO2	0.8545	0.7747
Al2O3	4.0086	3.8232
Cr2O3		
FeO	8.48	8.7759
MnO	0.3802	0.4007
MgO	14.6196	14.4468
ZnO	0.0298	0.003
CaO	21.6104	21.475
Na2O	0.3955	0.3878
K2O	0.0164	0.0001
NiO	0.0002	0.0038
P	0.0001	0.0094
S	0.0068	0.0001
Cl		
F		
Total	100.90	100.52

Mineral	Ol	Ol	Bt	Bt	Bt	Bt	APATITE	APATITE	APATITE
Analysis No.	Lo39_cir2spot7	Lo39_cir2spot8	Lo54PGM_cir7spot1	Lo54PGM_cir7spot2	Lo54PGM_cir7line1_1	Lo54PGM_cir7line1_2	LO52_C2line2_3	LO52_C2line2_5	Lo39MGM_cir1spot3
Run ID	tm070909	tm070909	tm070909	tm070909	tm070909	tm070909	tm130709	tm130709	tm070909
SiO2	38.0641	37.857	37.2434	37.4551	37.4325	37.6041	0.2539	0.24	5.2322
TiO2	0.007	0.0306	5.8028	5.9153	5.8495	5.814	0.0072	0.0036	0.5641
Al2O3	0.0419	0.0003	14.5335	14.4414	14.3933	14.424	0.0232	0.0021	1.4416
Cr2O3									
FeO	26.9605	26.6112	14.2828	14.1038	13.9268	13.5766	0.5251	0.4978	1.999
MnO	1.2425	1.1464	0.1601	0.1673	0.1548	0.1784	0.1913	0.1477	0.1825
MgO	36.1034	36.1116	15.8945	15.6241	15.8289	16.0169	0.214	0.2481	2.0723
ZnO	0.0883	0.0736	0.0002	0.0029	0.0495	0.0002			0.0764
CaO	0.0664	0.0966	0.0002	0.0445	0.0618	0.0111	53.6866	53.448	47.2989
Na2O	0.0141	0.0049	0.8989	0.901	0.8918	0.9185	0.0821	0.122	0.3227
K2O	0.0129	0.0148	8.206	8.0231	8.083	8.1098	0.0033	0.051	0.1586
NiO	0.0408	0.0576	0.0128	0.0972	0.0002	0.0018	0.0558	0.0306	0.0304
P	0.0096	0.0024	0.0278	0.0046	0.0139	0.0069	37.1513	37.6148	16.2131
S	0.0137	0.0001	0.0107	0.0401	0.0388	0.0147			0.033
Cl									
F									
Total	102.67	102.01	97.07	96.82	96.72	96.68	92.19	92.41	75.62

Mineral	MELT INC	MELT INC	MELT INCLUSION	MELT INCLUSION	MELT INCLUSION	MELT INCLUSION	MELT INC	MELT INC	MELT INC	MELT INC
Analysis No.	Lo39MGM_cir13spot5	Lo54PGM_cir5line1_2	Lo39MGM_cir5spot3MI	Lo39MGM_cir7spot4MI	Lo39MGM_cir9spot3MI	Lo39MGM_cir9spot5MI	Lo39_cir1spot7MI	Lo23MGM_cir14line1_1	Lo39_cir14line1_6	Lo39_cir14spot5
ID number	tm070909	tm070909	tm070909	tm070909	tm070909	tm070909	tm070909	tm070909	tm070909	tm070909
SiO2	66.7871	67.1002	67.7055	66.4485	66.2911	66.798	66.8821	65.4863	66.4345	65.5068
TiO2	0.5539	0.3728	0.4125	0.4467	0.51	0.4203	0.5213	0.5398	0.5045	0.4533
Al2O3	15.738	16.2431	16.2709	16.2529	15.8456	15.9867	15.8175	15.8019	16.3659	16.1817
Cr2O3										
FeO	2.8841	1.4437	2.8772	2.6522	2.9357	2.853	2.5422	3.2689	2.8106	2.9264
MnO	0.1349	0.1205	0.1532	0.0831	0.1606	0.144	0.1629	0.115	0.1202	0.1783
MgO	0.6408	0.3191	0.682	0.6925	0.6389	0.632	0.5896	0.606	0.7254	0.7381
ZnO	0.0002	0.0002	0.1369	0.0208	0.0774	0.0625	0.0002	0.0002	0.0151	0.0272
CaO	1.9084	1.8693	1.9491	2.0268	1.9746	1.8931	1.8	2.1761	1.8007	1.7283
Na2O	0.8181	0.8973	1.053	1.0854	0.9152	0.9234	1.1913	0.9801	1.2528	1.3119
K2O	4.3505	4.2715	4.3457	4.0823	4.2773	4.194	4.4303	4.4312	4.7217	4.917
NiO	0.0561	0.0075	0.0002	0.0002	0.0019	0.0243	0.0322	0.0002	0.0002	0.0266
P	0.0465	0.0491	0.0318	0.0611	0.0293	0.0513	0.0619	0.0392	0.0546	0.0347
S	0.0211	0.0028	0.0112	0.0407	0.0001	0.0323	0.0001	0.0113	0.0114	0.0142
Cl										
F										
Total	93.94	92.70	95.63	93.89	93.66	94.01	94.03	93.46	94.82	94.04

Mineral	MELT INC
Analysis No.	Lo54_cir5spot4
ID number	tm070909
SiO2	67.0284
TiO2	0.4073
Al2O3	17.6533
Cr2O3	
FeO	1.4048
MnO	0.1299
MgO	0.0432
ZnO	0.0637
CaO	1.9815
Na2O	0.7077
K2O	3.8319
NiO	0.0514
P	0.1348
S	0.0258
Cl	
F	
Total	93.46

Mineral	GLASS	GLASS	GLASS	GLASS	GLASS	GLASS	GLASS	GLASS	GLASS	GLASS	GLASS	GLASS
Analysis No.	LO18 c3 pt11	LO52_C5line1_7	LO52_C5line2_2	LO52_C5line2_10	LO52_C6line2_10	LO52_C6line3_10	LO52_C7line1_2	LO52_C7line1_20	LO52_C10line2_9	LO52_C11line2_9	LO52_C12line2_1	LO52_C3_line1_1
Run ID	tm010509	tm130709	tm130709	tm130709	tm130709	tm130709	tm130709	tm130709	tm130709	tm130709	tm130709	tm130709
SiO2	68.1817	62.4465	72.2011	68.8899	62.7951	66.8048	58.7978	72.065	69.7162	58.1949	67.6905	69.1604
TiO2	0.4286	1.191	0.4354	0.4294	0.3038	1.0626	0.521	0.4572	0.4833	0.7445	0.4364	0.4722
Al2O3	15.792	14.7351	16.4562	15.7044	19.4338	15.589	13.5466	16.3387	15.4575	13.3935	15.1983	15.6441
Cr2O3	0.0002											
FeO	2.8968	4.4505	2.8428	2.053	1.3582	6.5357	2.8866	2.6586	2.4784	4.5746	2.4903	2.5343
MnO	0.1637	0.2011	0.1377	0.1598	0.0002	0.162	0.1483	0.1706	0.1339	0.0967	0.0697	0.1118
MgO	0.5262	3.8458	0.6214	0.8785	0.4414	0.6856	1.9622	0.6195	0.6469	0.5134	0.6441	0.7302
ZnO	0.0401											
CaO	2.1064	4.2315	1.9134	1.7513	3.5394	1.7064	3.5069	2.0258	1.8558	1.8771	1.8809	1.8503
Na2O	3.4771	1.8376	3.6447	4.1682	3.6827	4.5377	2.2437	3.3987	2.9548	1.0359	2.5432	3.0817
K2O	4.4066	3.2781	4.4741	4.0603	2.1986	4.2865	3.5481	4.4585	4.4198	4.3155	4.1284	4.2139
NiO		0.0002	0.0002	0.0002	0.0002	0.0002	0.0002	0.0002	0.0977	0.0002	0.0092	0.0461
P		0.1415	0.2072	0.1037	0.0247	0.0684	0.0196	0.0888	0.0739	0.1221	0.1676	0.2019
S												
Cl												
F												
Total	98.02	96.36	102.93	98.20	93.78	101.44	87.18	102.28	98.32	84.87	95.26	98.05

Mineral	GLASS	GLASS	GLASS	GLASS	GLASS	GLASS	GLASS	GLASS	GLASS	GLASS
Analysis No.	LO52_C3_line1_8	LO52_C3_line2_2	LO52_C3_line4_8	Lo54MGM_cir11spot3	Lo23MGM_cir8line1_1	Lo39_cir5line1_19	Lo39_cir12line1_20	Lo39_cir14spot4	Lo54_cir2line1_15	Lo54_cir5_block1_glass_1_1
Run ID	tm130709	tm130709	tm130709	tm070909	tm070909	tm070909	tm070909	tm070909	tm070909	tm070909
SiO2	68.8802	68.9514	65.6596	69.6521	66.9876	61.6052	60.7552	68.3534	63.5338	58.469
TiO2	0.4628	0.2629	0.6192	0.4702	0.4285	0.3657	0.3575	0.4571	0.5778	0.5219
Al2O3	15.6263	14.6158	14.4725	17.0254	15.552	15.0662	13.9485	16.2813	14.6854	13.1788
Cr2O3										
FeO	2.6045	2.3605	2.3754	2.4981	3.0461	2.0672	1.9426	2.4047	1.9379	1.517
MnO	0.1631	0.2403	0.0916	0.1148	0.1521	0.1034	0.0922	0.1129	0.096	0.0753
MgO	0.6666	1.7852	0.7516	0.5451	0.7974	0.6561	0.5824	0.7276	0.5965	0.4912
ZnO				0.0002	0.0002	0.0002	0.0425	0.0121	0.0364	0.0182
CaO	1.883	1.4837	1.7146	1.4785	2.126	1.7439	1.1875	1.9334	1.7009	1.3305
Na2O	0.7217	0.5936	2.4726	0.8728	0.7064	0.8495	0.8622	0.72	0.6648	0.6159
K2O	4.365	4.0667	4.2545	4.8609	4.1087	3.7688	2.6244	4.1864	3.9896	3.7405
NiO	0.0369	0.0002	0.0002	0.0056	0.0002	0.0002	0.0002	0.0002	0.0002	0.0002
P	0.1084	0.0742	0.1377	0.0662	0.0565	0.0449	0.0376	0.0947	0.0174	0.0599
S				0.0028	0.0113	0.0001	0.0101	0.01	0.0014	0.01
Cl										
F										
Total	95.52	94.43	92.55	97.59	93.97	86.27	82.44	95.29	87.84	80.03

Mineral	GLASS	GLASS	GLASS	GLASS	GLASS	GLASS	GLASS
Analysis No.	Lo54_cir5_block1_glass_1_2	Lo54_cir5_block1_glass_1_6	Lo54_cir5_block1_glass_2_6	Lo54_cir5_block1_glass_3_5	Lo54_cir5_block1_glass_4_5	Lo54_cir5_block1_glass_4_6	Lo54_cir5_block1_glass_5_5
Run ID	tm070909	tm070909	tm070909	tm070909	tm070909	tm070909	tm070909
SiO2	67.7206	62.7585	68.3083	55.3106	58.6121	67.743	63.6084
TiO2	0.5979	0.5676	0.5535	0.0198	0.498	0.5736	0.563
Al2O3	16.129	15.2351	16.1467	27.8064	14.5127	16.2254	14.9185
Cr2O3							
FeO	2.776	2.442	2.7657	0.5005	2.0085	2.9753	1.5319
MnO	0.1465	0.1445	0.1314	0.0169	0.1296	0.122	0.143
MgO	0.7135	0.7114	0.6657	0.0629	0.7205	0.7065	0.675
ZnO	0.0002	0.0002	0.0002	0.0002	0.0002	0.0121	0.0455
CaO	2.1307	2.0591	2.3684	10.7219	1.6819	2.2909	1.7322
Na2O	0.6422	0.493	1.4262	5.3685	1.378	0.9252	0.7305
K2O	4.3731	4.0781	4.3733	0.3624	3.7445	4.5481	4.1451
NiO	0.0095	0.0513	0.0002	0.0002	0.0002	0.0228	0.0002
P	0.0621	0.0273	0.0695	0.0049	0.0695	0.0843	0.0648
S	0.0001	0.0142	0.0001	0.0001	0.057	0.0014	0.01
Cl							
F							
Total	95.30	88.58	96.81	100.18	83.41	96.23	88.17

Mineral	GLASS	GLASS	GLASS	GLASS	GLASS
Analysis No.	Lo54_cir5_block1_glass_6_4	Lo54_cir5_block1_glass_6_6	Lo54_cir5_block1_glass_6_7	Lo54_cir5_block1_glass_7_4	Lo54_cir5_block1_glass_7_7
Run ID	tm070909	tm070909	tm070909	tm070909	tm070909
SiO2	61.0419	61.3877	67.409	61.8708	67.9982
TiO2	0.5143	3.5688	0.5929	0.5355	0.5885
Al2O3	13.7116	14.8948	16.22	15.0383	16.1551
Cr2O3					
FeO	2.1089	1.6373	3.0079	1.9922	2.8691
MnO	0.1446	0.1033	0.1144	0.139	0.0957
MgO	0.6007	0.5292	0.7381	0.6292	0.7343
ZnO	0.0002	0.0665	0.0484	0.0968	0.0212
CaO	1.7224	1.7909	2.1214	1.902	2.2028
Na2O	0.408	0.5533	0.6687	0.4502	0.9466
K2O	4.0106	4.2108	4.4356	4.0583	4.6491
NiO	0.0002	0.0002	0.0076	0.0266	0.0002
P	0.0522	0.0814	0.0645	0.0671	0.0446
S	0.0001	0.0142	0.0001	0.0043	0.0185
Cl					
F					
Total	84.32	88.84	95.43	86.81	96.32